Light nuclei and antinuclei production in proton-proton interactions

A DISSERTATION SUBMITTED TO THE GRADUATE DIVISION
OF THE
UNIVERSITY OF HAWAIʻI AT MĀNOA IN PARTIAL
FULFILLMENT OF THE
REQUIREMENTS FOR THE DEGREE OF

DOCTOR OF PHILOSOPHY
IN
PHYSICS

MAY 2023

By
Anirvan Shukla

Dissertation Committee:

Philip von Doetinchem, Chairperson
Veronica Bindi
Jason Kumar
Sven Vahsen
Peter Berkelman

The sky is naught but dying stars.

- Nasus of Shurima

Acknowledgements

I wish to thank Philip von Doetinchem, my advisor, for showing me how to be a good physicist.

I wish to thank Amaresh Datta, Marek Gazdzicki, Diego Gomez, Maciej Lewicki, Piotr Podlaski, and Szymon Pulawski for helping me understand how protons collide in space and on Earth at CERN. I also thank Andrew Kuhlman, Chris Light, and Achim Stoessl for their valuable suggestions and input on the thesis draft.

I wish to thank the National Science Foundation for financial support, and the Open Science Grid consortium [1, 2], University of Hawai'i at Mānoa's Mana high performance computing cluster, and CERN IT Batch Service for letting me wield the magic of high-throughput computing.

I wish to thank Manimala Shukla, Colonel DS Shukla, and Caroline Tisdale, for showing me the joys of life.

Abstract

Identifying the nature of dark matter is a major unsolved problem in physics. The detection of low-energy cosmic-ray antinuclei could provide a "smoking gun" signature of dark matter annihilation or decay, as they are produced essentially free of the astrophysical background. Such a detection could also indicate new astrophysical phenomena like undiscovered antimatter sources in our Galaxy.

The main source of astrophysical antinuclei background are the interactions of cosmic-ray protons with hydrogen in the thin interstellar gas. However, their formation process is poorly understood. The impact of new-physics searches with cosmic-ray antinuclei can be increased by reducing uncertainties related to antinuclei formation modeling. For that purpose, this dissertation discusses how the coalescence mechanism for (anti)deuterons was extended to estimate the production of $^3\overline{\mathrm{He}}$ and $^4\overline{\mathrm{He}}$ in cosmic-ray interactions. The results were used to model how antinuclei are transported in our Galaxy, to predict the antinuclei flux received at Earth.

The production mechanisms of light antinuclei have been studied in accelerator-based experiments before. However, very few proton-proton measurements exist at energies which are relevant for cosmic-ray antinuclei production. Modeling of antinuclei formation also requires high-precision measurements of antiproton production. These factors motivate the analysis of new large p–p data sets from modern particle accelerator experiments.

NA61/SHINE is a fixed-target experiment at the CERN-SPS, which studies hadron-nucleus and nucleus-nucleus collisions for various physics goals. This dissertation presents new measurements of proton, antiproton, as well as $\pi^{\pm}$ and $K^{\pm}$ spectra, using the high-statistics p–p data from NA61/SHINE. The new results significantly extend the phase space coverage in rapidity and transverse momentum, as compared to previous results. They also dramatically reduce uncertainties in antiproton production. The first measurements of deuteron production at energies relevant for cosmic-ray studies are presented. The viability of measuring antideuteron production and two-particle angular correlations, with the recently-upgraded NA61/SHINE detector, is also shown.

Table of Contents

List of Tables

List of Figures

Chapter 1
Introduction

Dark matter is a hypothetical form of matter that does not appear to interact with electromagnetic radiation and is thus invisible to ordinary telescopes. However, it is inferred to exist from its gravitational effects on visible matter, such as the rotation curves of galaxies, the gravitational lensing of light, and measurements of the large-scale structure of the universe [3].

Cosmic rays are high-energy particles that originate from outer space and constantly bombard the Earth. They consist mainly of protons, helium and other atomic nuclei, but also include electrons, positrons, and neutrinos [4].

Chapter 2 provides a background of particle astrophysics and the current motivations for dark matter. After a brief overview of Galactic cosmic-rays, it reviews the current status and future prospects of cosmic-ray antinuclei searches, and explains how cosmic antinuclei can be an important tool to investigate the nature of dark matter as well as other unknown exotic astrophysical phenomena in our Galaxy.

Chapter 3 introduces the modeling of (anti)nuclei production in astrophysical processes via the two-particle coalescence model developed as part of this work. It then shows how the coalescence model was extended to estimate the astrophysical production of light antinuclei like $^{3}\overline{\mathrm{He}}$ and $^{4}\overline{\mathrm{He}}$ using very large-scale simulations. The calculated uncertainty in antinuclei formation and its effect on the expected antiparticle flux received on Earth is discussed. Comparisons with expected antiparticle flux from various dark matter models are also shown.

Towards the goal of reducing uncertainties related to antinuclei formation modeling as well as interactions of cosmic rays with the interstellar medium (ISM), Chapter 4 presents the measurements of proton and antiproton production spectra using the high-statistics p–p data sets from NA61/SHINE. The new results from this work significantly extend the phase space coverage in rapidity and transverse momentum, as compared to previous measurements in p–p interactions. Sec. 4.5 presents the first deuteron production measurements for proton–proton interactions in the low-energy

region near the deuteron production threshold. The details of this new NA61/SHINE measurement using a newly-developed analysis technique are presented.

In Chapter 5, ongoing and future measurements using the high-statistics p–p data in NA61/SHINE are presented. The chapter also discussed ongoing NA61/SHINE upgrades and the potential for future measurements with the upgraded detector. Furthermore, it outlines steps toward developing a quantum-mechanical description of antinuclei formation, highlighting the importance of advancing our understanding of this process.

Chapter 6 provides a summary of the work presented in this study, encapsulating the key findings and their implications for the field.

Chapter 2
Cosmic-ray Antinuclei As Messengers Of New Physics

What is our Universe made of? This is a key question which arises from our fundamental desire to know what all is out there in our Universe. The current understanding is that only about 5% of the Universe consists of ordinary matter, about 26% is made of the unknown dark matter, and the remaining 69% is dark energy [6]. The structure of ordinary matter is a crucial aspect of particle physics, and the Standard Model (SM) is the most advanced framework to describe it.

2.1 Standard Model Of Elementary Particles

The Standard Model of elementary particles is a theory that describes how the basic building blocks of ordinary matter interact through three of the four fundamental forces: electromagnetic, weak, and strong force [7]. It includes 12 types of fermions, which are elementary particles of ordinary matter with a quantum-mechanical spin of 1/2, and 5 types of bosons, which are spin-1 particles that mediate the fundamental forces (see Fig. 2.1).

Fermions can be further classified into quarks and leptons. All common observable matter around us is composed of up-quarks, down-quarks and electrons (which are a type of lepton). Quarks have been found only within bound states called hadrons, which are held together by the strong force mediated by massless bosons called gluons. Most of our knowledge about quarks comes from observing hadrons. Hadrons are of two types - baryons, which are made of odd number of quarks (usually three), or mesons, which consist of an equal number of quarks and antiquarks (usually one of each). Common baryons are protons and neutrons, while pions and kaons are examples of mesons. Each elementary particle has its corresponding antiparticle which has the same mass but an opposite electrical charge. Hence, quarks have corresponding antiquarks, which can bind to form particles like antiprotons and antineutrons.

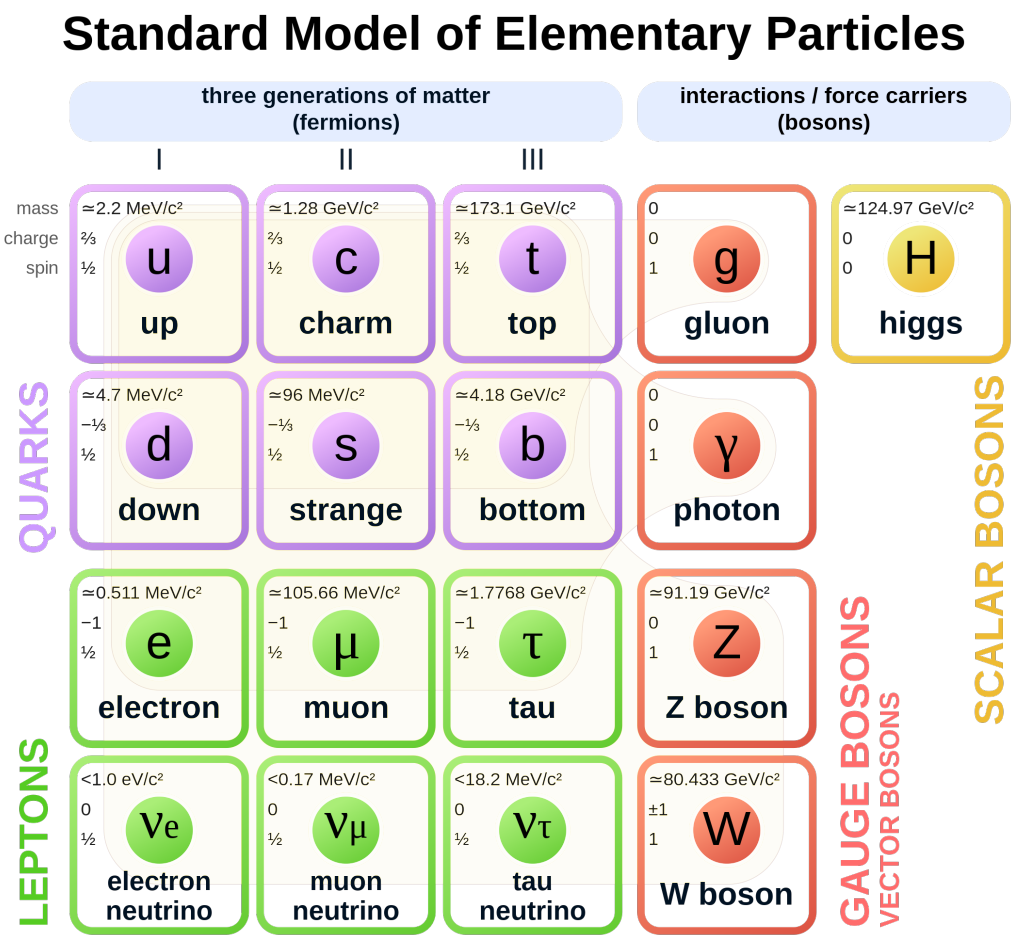

Figure 2.1: Standard model of elementary particles. Figure from [5].

The Standard Model is one of the most successful and tested theories in physics, but it has limitations and open questions that motivate further research. Among other phenomena, it does not explain gravity, matter–antimatter asymmetry [8], or the nature of dark matter.

2.2 Dark Matter

About 95% of the mass-energy of the Universe is postulated to be a combination of dark matter and dark energy. Dark energy is a form of energy that causes the universe to expand at an accelerating rate. Dark matter is a type of matter that does not appear to interact via the electromagnetic force, as the interaction is constrained by data to be very small and therefore does not emit or reflect light. It interacts with gravity and holds galaxies and clusters of galaxies together. Despite being invisible

and undetectable by ordinary means, dark matter is estimated to make up about 26% of the mass-energy present in the Universe [6]. However, its nature remains unknown. Various theories and experiments [9–11] have sought to explain and detect dark matter, but none have been conclusive so far. The motivations for dark matter stems from observations and measurements that challenge our current understanding of gravity, with the leading explanation being the presence of matter that does not appear to interact electromagnetically. This suggests the existence of unseen mass in the Universe which influences the behavior of ordinary, visible matter through gravity.

The first evidence supporting the existence of dark matter came from observations of the rotation velocities of galaxies [12, 13]. Previous signs had been detected in the 1930s by Jan Oort, who studied stellar velocities in the Milky Way galaxy [14], and Fritz Zwicky, who examined galaxy velocities in the Coma Cluster. However, these early measurements suffered from numerous issues [15, 16]. Modern measurements of the Galaxy rotation curves show that stars at the edges of galaxies rotate faster than expected from the visible mass of the galaxies. This discrepancy can be explained by assuming the presence of additional unseen mass, i.e., dark matter, that increases the total gravitational force acting on the stars. Another evidence comes from a phenomenon known as gravitational lensing. According to Einstein's theory of general relativity, objects with mass can bend light around them. Observations of this lensing effect around very massive objects such as galaxy clusters indicates the presence of more mass than what visible matter alone can account for [17].

Another hint comes from the Cosmic microwave background (CMB), which is the afterglow of the Big Bang. Measurements of temperature fluctuations in the CMB provide information about the density and distribution of matter in the early Universe. The observed fluctuations are consistent with the presence of dark matter. Dark matter also plays a crucial role in the formation of large structures in the universe, such as galaxy clusters and superclusters. Simulations that include dark matter can reproduce the observed distribution of these large-scale structures, while simulations without dark matter may fail to do so [18]. Finally, observations of colliding galaxy clusters such as the Bullet Cluster have provided additional indications. By analyzing the distribution of mass after the collision, it was observed that the visible matter (which emits X-rays) and the majority of the total mass (inferred from gravitational lensing) were separated. This separation suggests the presence of an unseen, non-interacting component, which is consistent with dark matter [19].

These experimental observations provide compelling support for the existence of dark matter, despite the uncertainty surrounding its exact properties. The quest for direct evidence of dark matter continues. Unraveling its nature and origins is among the most significant challenges in deepening our understanding of the cosmos and its evolution.

Prospects for Dark Matter Searches Current experiments focus on searching for new novel particles beyond the Standard Model that can explain dark matter. One of the most theoretically well-motivated candidates for such a particle is the weakly interacting massive particle, or WIMP. The search for new dark matter particles is based on three main strategies: make it, shake it or break it. There are many current and planned experiments for each of the three types of searches. "Making" dark matter involves collider searches which probe the products of high-energy particle collisions for signs of new particles that could be dark matter candidates. "Shaking" involves searching for the tiny nuclear recoils and scattering cross sections that dark matter particles could cause when they interact with atomic nuclei in highly-sensitive underground detectors.

"Breaking" involves using space and ground-based detectors to pickup indirect signals of dark matter particles as they annihilate or decay in space. In various viable dark matter models [20–43], these processes could leave observable signatures in the neutrino, gamma-ray, and cosmic-ray spectra, such as spectral features, anisotropy or correlations with other astrophysical signals. Several experiments have been designed to search for these signatures using different techniques and detectors, such as balloon-borne instruments, ground-based telescopes and space-based observatories.

2.3 Galactic Cosmic Rays

Cosmic rays (CR) are high-energy charged particles that travel through interstellar space and reach Earth. They were first discovered by Victor Hess in 1912, who was studying the ionization of air during balloon flights [44]. The modern study of cosmic rays is an interdisciplinary field encompassing astrophysics, particle physics, solar physics, and geophysics. It has been instrumental in advancing our understanding of fundamental physics, and continues to reveal new phenomena in astrophysics.

The main source of Galactic cosmic rays is thought to be diffusive shock acceleration of interstellar gas by supernova remnants, with possibly small contributions from other sources like pulsars and pulsar wind nebulae [43]. Cosmic rays from such sources are called primary, and mostly consist of protons and α-particles. Secondary cosmic rays are formed either by the interaction of primary cosmic rays with the hydrogen (H) and helium (He) atoms within the interstellar medium (ISM) or by the decay of unstable nuclei. Fig. 2.2 is an illustration of these different processes.

The energy spectrum of cosmic rays decreases steeply with energy, and can be approximated by a power-law function with some minor structures. Most cosmic-ray particles have kinetic energy of less than ~1–10 GeV per nucleon, and hence, are influenced by the magnetic field of the Sun and Earth. Fig. 2.3 shows how the primary cosmic-ray flux declines rapidly with increasing energy [45].

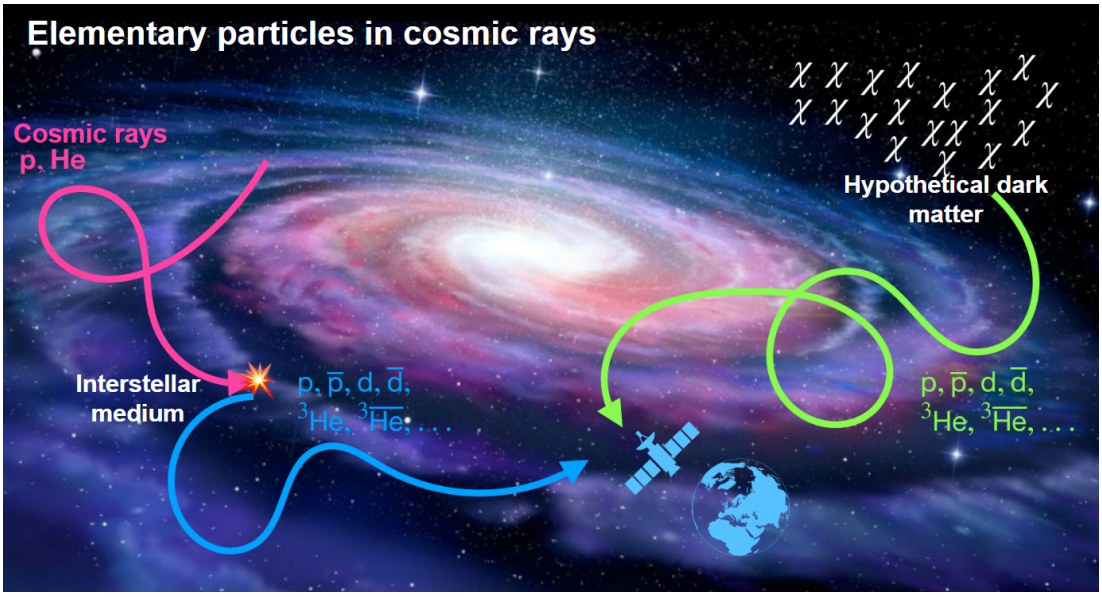

Figure 2.2: A cartoon showing various CR interactions in the Galaxy. CRs can be primary CRs like protons or α-particles produced by astrophysical processes like supernovae. They can be secondary CRs as well, which are produced when primary CRs collide with the interstellar medium, or could also be produced by the annihilation or decay of hypothetical dark matter. Figure adapted from [46].

Prospects for Dark Matter Signatures in Galactic Cosmic Rays Dark matter, which may have been in thermal equilibrium during the early universe, is thought to have "frozen out" as the universe expanded and cooled. This suggests that dark matter particles could interact with one another and generate particles from the Standard Model. Indirect searches for dark matter focus on identifying potential differences between cosmic rays produced by dark matter and those from standard astrophysical processes. Cosmic-ray antiparticles can be ideal candidates for such searches because the standard astrophysical background, which is mostly generated by the interactions of primary cosmic rays with the interstellar medium, is very low. It is also predicted to have a different spectral shape, as it is forward-boosted due to the higher velocities of the incident primary cosmic-ray particles. These differences, especially at kinetic energies below few GeV/nucleon, are the main motivation for cosmic-ray searches of antiparticles. Rare antiparticles can act as messengers for new and exotic processes in the Galaxy, such as dark-matter annihilation or decay [20–43].

2.4 Antiparticles in Cosmic Rays

Modern space-based and balloon-borne experiments like BESS, PAMELA, and AMS-02 have enabled the growing interest in searches for cosmic-ray antiparticles [43, 47–53]. The only cosmic-ray antiparticles that have been detected so far are positrons [54–

56] and antiprotons [47–50, 53]. The study of their spectra faces challenges due to significant or uncertain levels of the astrophysical background. Recent findings from PAMELA [54], Fermi [57], and AMS-02 [55, 56, 58] reveal a structure in the positron data at high energies that cannot be explained by cosmic-ray propagation models, like GALPROP [59]. The possible explanations for this phenomenon range from various acceleration mechanisms to production of positrons in pulsars and dark-matter annihilation [60], as well as evidence for dark matter with TeV-scale mass.

AMS-02 has measured the cosmic antiproton flux with percent-level precision in a large energy range [62]. However, the antiproton spectra do not display a similar feature like positrons [49, 63]. They have instead been useful in placing constraints on various dark matter models [28, 64, 65]. It is worth noting that the statistical accuracy of these constraints is limited at lower energies, and deviations in the observed antiproton fluxes from the expected non-exotic cosmic-ray flux have been observed with varying degrees of significance [66–72]. Some antiproton studies suggest that these deviations, along with the γ-ray excess observed in the Galactic Center [67, 70], could be hints of dark-matter. However, these deviations are not very large, and several uncertainties exist in the measurement. These uncertainties include factors such as antiproton production in primary cosmic-ray interactions with the ISM, the transport of cosmic-ray particles in the ISM and in the Sun's magnetic field, and lastly, instrumental resolution effects. Consequently, interpreting these antiproton measurements continues to be a challenge.

Cosmic-ray Antinuclei Cosmic-ray antinuclei like antideuterons and antihelium are extremely rare particles that originate from high-energy interactions of primary CRs with the ISM. They are also predicted to be produced from a wide range of exotic sources like dark matter annihilation or decays [20, 41, 73], or even primordial black hole evaporation [43]. The discovery of cosmic antinuclei like antideuterons and antihelium has the potential to transform both astrophysics and particle physics. It can offer insights into the origin, propagation, and composition of cosmic rays, as well as reveal potential evidence for new physics beyond the Standard Model. The detection of low-energy cosmic antideuterons and antihelium could provide a "smoking gun" signature of new physics, as they are virtually free from astrophysical backgrounds (see Fig. 2.4), making them crucial for the ongoing search for novel phenomena. It will allow the probing of a variety of dark matter models that evade or complement collider, direct, or other cosmic-ray searches [20–23, 26–28, 30–32, 35–39, 74]. However, detecting cosmic antinuclei is very challenging as they are extremely suppressed by the dominant foreground of cosmic nuclei. It requires sophisticated techniques to identify them and reject the false positives.

In the search for cosmic messengers with a higher signal from exotic processes with respect to the astrophysical background (see Fig. 2.4), cosmic-ray antideuterons were proposed about 20 years ago [20] (for recent reviews see [41, 73]). Antideuterons are

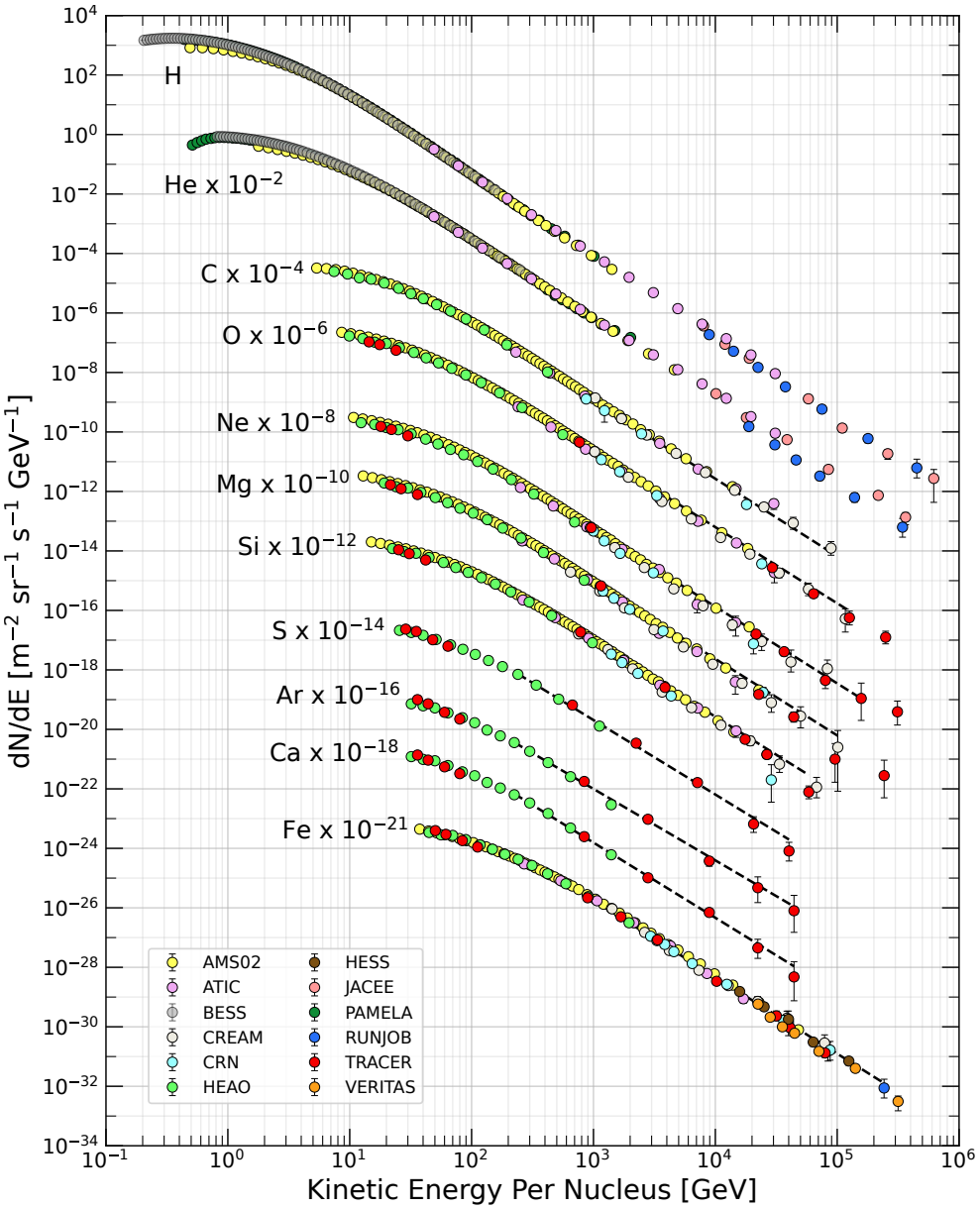

Figure 2.3: Fluxes of primary cosmic-ray nuclei are plotted vs. kinetic energy per nucleons. The inset shows the H/He ratio at constant rigidity. Figure adapted from [61].

made of one antiproton and one antineutron. It is known from studies of proton–proton collisions in particle colliders on Earth that the production of light antinuclei gets suppressed by a factor of about 1000, for every additional antinucleon in the antinucleus final state [78]. As a result, the cosmic-ray antideuteron flux is predicted to be much lower than the antiproton flux. In a broad range of models, including those involving dark-matter annihilation, it is possible to generate a cosmic antideuteron flux that is larger than the predicted astrophysical background by several orders of

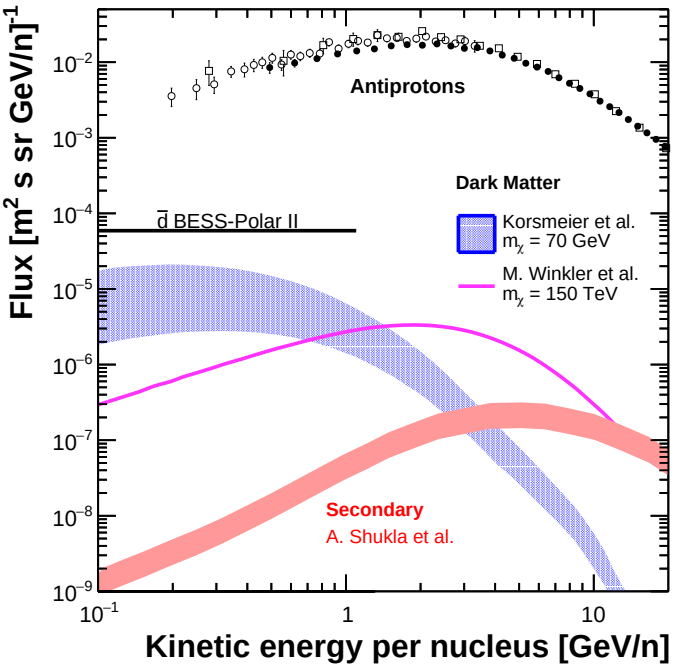

Figure 2.4: Antiproton flux [48, 49, 62, 63] and antideuteron exclusion limits in comparison with the predicted antideuteron flux corresponding to the potential AMS-02 antiproton excess, interpreted as dark matter annihilation (blue) [35, 75]) and secondary astrophysical background (red) [43]. The magenta line shows a new model, motivated by the AMS-02 antihelium nucleus candidates [76]. The width of the bands indicates the uncertainty in antideuteron formation. In addition, the BESS-Polar II sensitivity results [77] are shown.

magnitude. This difference in flux also exhibits a distinct spectral shape, which is a result of the underlying kinematics. Despite the larger flux, it still remains several orders of magnitude lower than that of the antiproton flux. Because of these features, the detection of even a few cosmic-ray antideuterons would represent a potential breakthrough in finding signatures of exotic processes.

The BESS experiment [47] has reported the best antideuteron exclusion limits so far, while the analysis of the AMS-02 data is ongoing. The upcoming GAPS [79–81] balloon-borne experiment, which is designed specifically for low-energy cosmic antinuclei searches, is expected to have its first flight soon.

While attempting a first-time discovery of light antinuclei like antideuterons, antihelium, and anticarbon, the AMS-02 experiment unexpectedly detected several antihelium candidates in its higher-velocity region [82–87]. This exciting development leads to the assumption that antideuterons should also be observable in large quantities. However, no antideuteron candidates have been announced yet. This has generated significant theoretical interest, but there is no preferred explanation for these antihelium candidates as of now. Confirmation of cosmic antihelium detection

would have a direct impact on the predictions of the antideuteron flux. Any model which explains the cosmic-ray antihelium signal must not overpredict the measured antiproton flux, as well as comply with current antideuteron detection limits.

Antihelium originating from antimatter-dominated regions in the Universe is currently considered highly unlikely, as existing observations have not provided substantial evidence for such regions [88, 89]. Various proposed models include modified antihelium formation models [36, 90], dark matter annihilation [31, 32, 35, 37, 39], or even emission from the nuclear processes of a nearby antistar [91]. Although these models offer potential explanations for the presence of antihelium, further experimental evidence and theoretical developments are needed to confirm or refute these possibilities.

The impact of dark matter searches with CR antinuclei, especially in light of the AMS antihelium candidates, can be increased by improving our understanding of how astrophysical antinuclei are produced in our Galaxy. Precise determination of the interaction cross sections of CRs with the ISM, along with reducing the uncertainties associated with antinuclei formation in these interactions, are the primary challenges that need to be overcome to improve the interpretation of cosmic-ray data [41, 92, 93]. The focus of this work is to address these uncertainties. These are discussed in Chapter 3.

Chapter 3
Astrophysical Antinuclei Production and Propagation in the Galaxy

Over the past fifty years, the fields of cosmic-ray, antimatter, and dark matter physics have evolved together [34]. Antideuterons, which consist of one antiproton and one antineutron, were first identified in the early 1960s in experiments using proton beams from the CERN Proton Synchrotron [94] and Brookhaven Alternating Gradient Synchrotron [95]. By that time, deuterons, nuclei which are made of one proton and one neutron, had already been identified in nuclear emulsions exposed to cosmic rays [96].

The production of deuterons and antideuterons in collider experiments enabled the testing of models to describe their formation. This led to the development of a two-stage formation process, which involves the creation of a nuclear cascade in which multiple nucleons interact to form a nucleus [97–100]. However, uncertainties in the antinuclei formation mechanism remain one of the dominant source of uncertainties in the antinuclei flux predictions [34, 41]. This chapter provides an overview of the different formation models, their advantages and drawbacks, and how they can be extended to model the production of antinuclei heavier than antideuterons.

3.1 Uncertainties in Cosmic Antinuclei Formation

In our matter-dominated Universe, astrophysical production of antinuclei can occur only as pair production from the collision of CRs with the ISM, with protons being the largest component of both CRs and the ISM (in the form of hydrogen gas). Cosmic antinuclei can be formed in these nucleus–nucleus (A–A) interactions when the collision energy is above their respective production thresholds. The production threshold increases sharply with antinucleon number because every additional antinucleon in the final state requires the production of a corresponding nucleon as well. The threshold energies for $\overline{d}$, $^3\overline{\mathrm{He}}$, and $^4\overline{\mathrm{He}}$ production in p–p

interactions are about 17, 31, and 49 GeV, respectively, in the target frame, or about 5.7, 7.5, and 9.7 GeV, respectively, in the center-of-mass frame of the collision.

Nucleus–nucleus interactions in accelerator-based experiments have been used to investigate the production mechanisms of light cosmic antinuclei in a variety of collision systems and energies [101–119]. These studies aim to develop a comprehensive model of cosmic antinuclei production across various astrophysical phenomena. [41]. However, most of this data comes from heavy-ion collisions. Such measurements offer limited relevance for reducing uncertainties related to cosmic rays, as heavy-ion interactions are not the predominant type in the Galaxy. It is important to emphasize that measuring antinuclei production in proton-proton interactions in accelerator-based experiments is challenging. This is due to the extremely low antinuclei production rate, especially at collision energies near the production thresholds. For example, the antideuteron production rate can be less than one per million collisions for p–p interactions at ~100 GeV. There is also a substantial background of charged hadrons which are produced in these interactions, which can complicate the identification of antinuclei in particle detectors. Because of these factors, previous studies have not been sufficient in accurately modeling the production mechanism of cosmic antinuclei.

Due to the critical lack of precise measurements of proton-proton collisions in modern experiments, relatively large uncertainties of about a factor of 10 persist in the low-energy region near the antinuclei production thresholds, at collision energies below a few hundred GeVs in the rest frame of the ISM [92]. This region is the most important for cosmic-ray studies, as it is the dominant source of the astrophysical antinuclei flux. This can be seen in Fig. 3.1, which shows the product of the cosmic-ray proton flux with the estimated production probability of light antinuclei in proton-proton interactions as a function of collision kinetic energy. The product peaks between 50–500 GeV, highlighting the collision energy range which contributes the most to the astrophysical antinuclei flux (see Sec. 3.6 for details of the source term calculations).

Several efforts are currently underway to reduce these uncertainties using new data from experiments like ALICE [120] at CERN's Large Hadron Collider (LHC), and NA61/SHINE [121], a fixed-target experiment at CERN's Super Proton Synchrotron (SPS). In addition to production cross section measurements, the loss of antinuclei due to their interactions with the ISM during their transport to Earth can also be studied in these experiments, as demonstrated in [43, 122]. It is important to note that although ALICE p–p measurements offer valuable information for setting asymptotic limits to (anti)nuclei production models, NA61/SHINE has the advantage of conducting measurements in the low-energy range close to the production thresholds. This range is highly relevant for cosmic antinuclei searches, and may yield results that potentially differ from the high-energy limit. However,

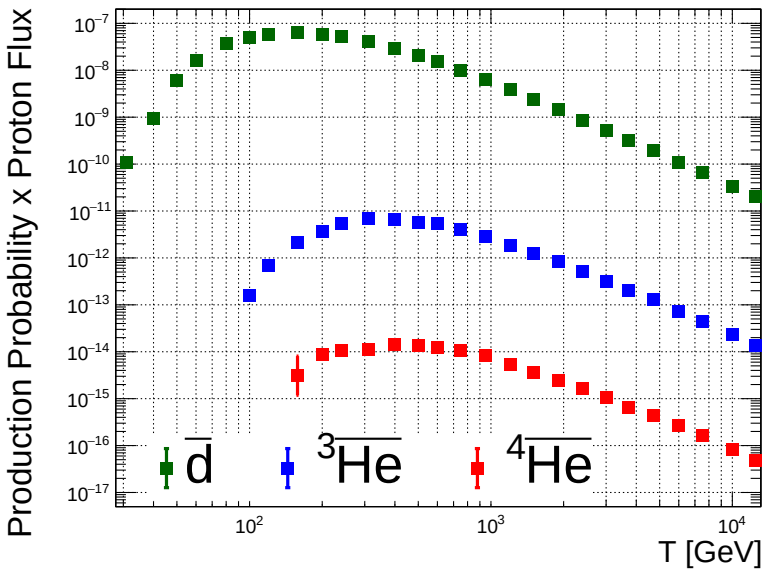

Figure 3.1: Cosmic-ray proton flux multiplied with the antideuteron, $^3\overline{\text{He}}$, and $^4\overline{\text{He}}$ production probability estimated from about 100 trillion p–p simulations with `EPOS-LHC` [93], as function of the collision kinetic energy T. Most error bars in this simulation are too small to be visible. See Sec. 3.1 and 3.3 for details.

NA61/SHINE also encounters the challenge of low antinuclei production rates. The NA61/SHINE measurements will be discussed in detail in Chapter 4.

The ongoing measurements are critical for constraining the production and transport of cosmic-ray antinuclei in our Galaxy [26, 123]. Comprehensive modeling of the antinuclei production in A–A collisions is necessary for the interpretation of cosmic antinuclei fluxes, especially for p–p interactions at lower energies (50–500 GeV/c). For instance, the Report of the Topical Group on Particle Dark Matter for Snowmass 2021 [124] concluded that "This is an area where considerable improvement is possible in the near future. Measurements from fixed-target accelerator experiments, covering a range of energies, with the capacity to detect antiproton, antideuteron and antihelium nuclei, will be of great benefit to achieve reduced cross-sectional uncertainties."

3.2 Antinuclei Formation Modeling

The formation of light antinuclei in hadronic interactions can be described by different models; however, the precise production mechanisms remain elusive due to the limited availability of experimental measurements, as discussed above. Fig. 3.2 shows the (anti)protons and (anti)neutrons constituents of heavier (anti)nuclei.

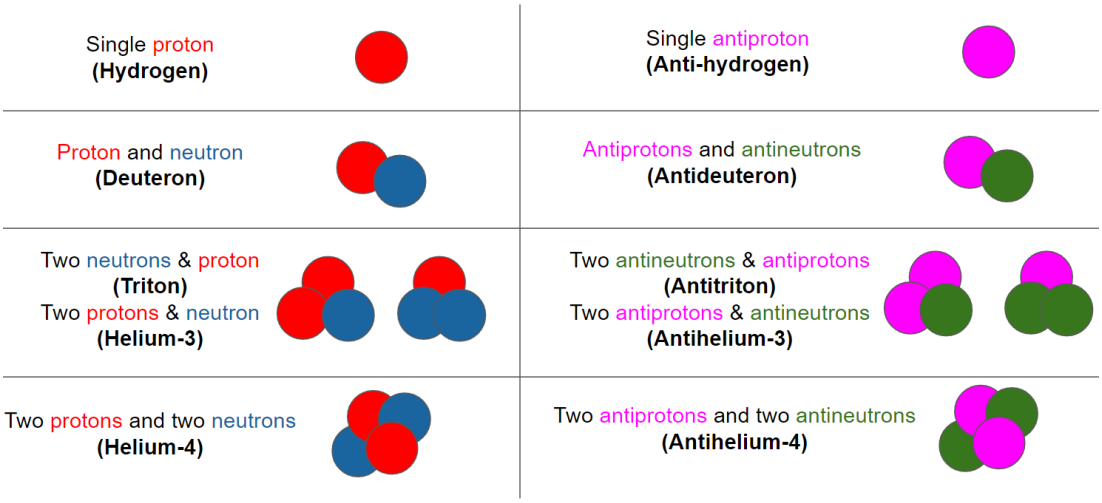

Figure 3.2: Building up light (anti)nuclei by successively adding (anti)protons and (anti)neutrons.

The two most popular models to describe antinuclei production are the coalescence model and the thermal model, but they are based on different underlying physics. The simple coalescence model (see Sec. 3.2.2) is a phenomenological model based on the assumption that any pair of (anti)proton and (anti)neutron within a sphere of radius p_0 in momentum space will coalesce to produce an (anti)nucleus. Antinuclei production can also be described by the thermal or statistical model (see Sec. 3.2.1). There have also been initiatives to develop a quantum mechanical description of the formation process [90, 125–127].

3.2.1 Thermal Model

The production of light nuclei in p–A or A–A collisions (where A is a nucleus) can be described by the statistical hadronization or thermal model approach, where the hadronization happens in so-called fireballs [128–130]. In this model, all products of the fireball continue interacting with each other until the mean free path for elastic collisions is larger than the system size (called the freeze-out condition) [131]. The resulting particle spectra can be used to examine the conditions at freeze-out, and to discriminate between predictions of coalescence and thermal models. The particle yields depend exponentially on the chemical freeze-out temperature T_{chem} and the mass m:

$$\frac{\mathrm{d}N}{\mathrm{d}y} \propto \exp\left(-\frac{m}{T_{\mathrm{chem}}}\right), \tag{3.1}$$

where $\mathrm{d}N/\mathrm{d}y$ is the particle rapidity density. Rapidity is a dimensionless quantity with convenient transformation properties under Lorentz boosts along the beam axis [132]. Due to their large masses, the abundance of nuclei is very sensitive to

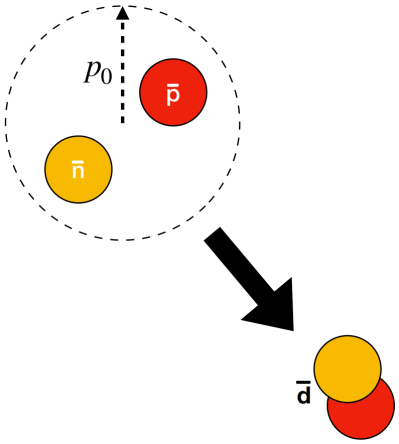

Figure 3.3: Any antiproton-antineutron pair within a sphere of radius p_0 in momentum space is assumed to coalesce to produce an antideuteron. Figure adapted from [46].

T_{chem}. The value of T_{chem} obtained from data is about $\sim$150 MeV/c^2 and shows a weak energy dependence. As the binding energy of (anti)deuterons is very low (2.2 MeV), the chance to breakup in the aftermath of the fireball creation should be high. Nevertheless, the measured (anti)nuclei yields are reproduced in a wide range of collisions by the existing models [41, 131, 133].

However, such models do not provide the detailed information on momentum distribution of the produced (anti)deuterons. Additionally, they are not suited to extract a general formalism for the production of (anti)nuclei in hadron–hadron collisions in the very broad energy range required to characterise the production of secondary antideuterons by CR interactions with the ISM. Coalescence models, on the other hand, can provide detailed predictions for light antinuclei production yields and momentum spectra. They can also be applied to the full energy range of CR interactions [43]. Measurements of particle mean multiplicities, along with the deuteron-to-proton and deuteron-to-antiproton ratios as a function of mean multiplicity, can be an important tool to differentiate between the predictions of the coalescence and thermal models. The thermal model overpredicts the deuteron-to-proton ratio in p—p interactions [134, 135].

3.2.2 Coalescence Model

The coalescence model has been applied to describe the light antinuclei formation process in results from ALICE and other experiments [45, 92, 93]. In this model, the fusion of an antiproton and an antineutron into an antideuteron is based on the assumption that any antiproton-antineutron pair within a sphere of radius p_0 in momentum space will coalesce to produce an antinucleus (see Fig. 3.3). The coalescence momentum p_0 is a phenomenological quantity and has to be determined

through fits to experimental data [100]. Its value lies in the range of about 100 MeV/c. This is smaller than the typical scale at which the perturbative theory of quantum chromodynamics breaks down. This means that coalescence is sensitive to non-perturbative effects, and hence is harder to predict theoretically. The simple coalescence model links the (anti)proton N_p and (anti)neutron N_n yields to the (anti)nucleus yield N_A with mass number A:

$$E_A \frac{\mathrm{d}^3 N_A}{\mathrm{d}p_A^3} = B_A \left(E_p \frac{\mathrm{d}^3 N_p}{\mathrm{d}p_p^3} \right)^Z \left(E_n \frac{\mathrm{d}^3 N_n}{\mathrm{d}p_n^3} \right)^N \text{ with } B_A = A \left(\frac{4\pi}{3} \frac{p_0^3}{m_p} \right)^{A-1}, \tag{3.2}$$

with E_X and p_X being the corresponding energies and momenta, Z the number of (anti)protons, N the number of (anti)neutrons, and m_p the proton mass. This is also known as the analytical coalescence model.

However, this is overly simplistic since it does not take into account effects like energy conservation, spin alignment etc., which have an important effect on deuteron and antideuteron formation. It also assumes that the production of antiprotons and antineutrons is uncorrelated [136] and expresses the momentum distribution of the coalesced particle as the product of two independent isotropic distributions. This is another simplification since correlations have an important effect on the coalescence process [137–139]. Furthermore, it does not consider the higher energy threshold for antinuclei production as compared to that of nuclei.

To take into account the hadronic physics (energy and momentum, angular correlations, event topography, antiproton-antineutron production asymmetry, etc.), MC hadronic event generators are used. Typical hadronic generators [140–146] do not produce light (anti)nuclei. Therefore, modern techniques create an event-by-event coalescence model afterburner coupled to the hadronic generators. The afterburner applies the coalescence condition to $\overline{pn}$ or pn pairs on a per-event basis. (e.g., Refs. [27, 92, 147]). For each event, the momentum difference of each antinucleon pair is calculated in their corresponding center-of-mass frame. If the momentum difference is smaller than p_0, a new particle is produced with a momentum equal to the sum of the constituent particle's momenta. The coalescence condition can be expressed as:

$$|\vec{k}_{\bar{p}} - \vec{k}_{\bar{n}}| < 2p_0. \tag{3.3}$$

The coalesced particle's binding energy is taken into account by calculating its total energy from its calculated momentum and the Particle Data Group [148] value of its rest mass. The constituent antiprotons and antineutrons are removed from the event, and the process is repeated for all remaining antinucleons, until all possible pairs are exhausted. The coalescence momentum p_0 is varied as a free parameter, and best-fit values are obtained by comparisons with the experimental data.

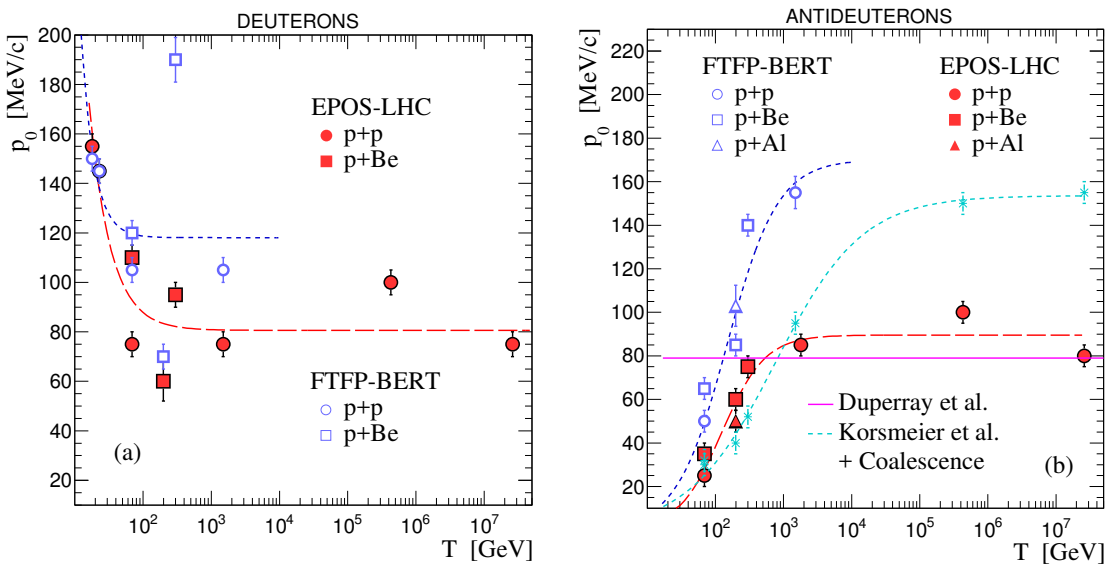

Figure 3.4: Fitted parametrizations of coalescence momentum p_0 for deuterons (left) and antideuterons (right, Eq. 3.4) as function of the collision kinetic energy T, from two hadronic generators, EPOS-LHC (long-dashed red line) and FTFP-BERT (dashed blue line). Additionally, the parametrization of Korsmeier *et al.* [149] are included (dashed cyan line). The constant value of $p_0 = 79\,\mathrm{MeV}/c$ estimated by Duperray *et al.* [150] is also shown (solid magenta line). Figure adapted from [92].

To simulate the production of antideuterons and larger antinuclei, an accurate description of the production of constituent particles (antiprotons and antineutrons) is of paramount importance. In Ref. [92], the formation of deuterons and antideuterons was studied using multiple MC event generators in the framework of Cosmic Ray Monte Carlo package (`CRMC`) [151]. This study demonstrated that the parametrization of p_0 was dependent on the choice of the MC event generator. Moreover, the `EPOS-LHC` MC event generator [140], despite many discrepancies with measurements, was shown to be the most consistent with $\overline{p}$ production data in a broad range of energies. Therefore, it was chosen as the hadronic event generator for this work as well. The kinetic energy dependence of p_0 for the antideuteron production using `EPOS-LHC` was described by the following parametrization:

$$p_0\,(T) = \frac{A}{1 + \exp\,(B - \ln(T/C))} \tag{3.4}$$

where T is the collision kinetic energy in GeV. The parameters A, B, and C were determined to be $89.6 \pm 3.0\,\mathrm{MeV}/c$, 6.6 ± 0.88, and 0.73 ± 0.10, respectively [92]. Fig. 3.4 shows the p_0 parametrizations and their steep change in the region that is most relevant for cosmic rays (up to a few 100 GeV). Historically, a constant p_0 value of about $80\,\mathrm{MeV}/c$ was assumed above the production threshold [22]. With

the spread in p_0 values, and the antiproton mismatch between generators and data, the total antideuteron yield was found to have an uncertainty of more than a factor of 10 [92]. Fig. 3.4 also shows a general discrepancy between the two commonly used hadronic event generators, with `Geant4`'s FTFP-BERT model [143] being about 50% higher than `EPOS-LHC`. The underlying uncertainties could potentially be even larger. As existing antideuteron production data are very limited, and the fitted coalescence momenta from p–p, p–Al, and p–Be collisions are relatively close, Gomez *et al.* [92] obtained a parametrization which was independent of the collision system size. However, the p–Al and p–Be results disagree by about 2σ, and only one p–p point exists in this interesting range. Therefore, for an improved understanding of antinuclei formation, more p–p measurements in the 50–400 GeV/c range are crucial.

The event-by-event coalescence afterburner approach presents several limitations as well. It employs a simplified system-size-independent single parameter to describe the nucleus formation process. It neglects the initial and final nuclear spin states. Spatial separation of nucleons is only considered by excluding (anti)nucleons produced by weak decays. Measuring (anti)neutron spectra is challenging, which may results in different hadronic generators being untuned for accurate production. Given the small p_0 value, it is sensitive to two-particle angular correlations of the produced nucleons. Therefore, it is important to recognize that the coalescence model is not a nuclear-physics model for the formation of light antinuclei derived from first principles. Instead, it should be seen as an empirical approach, capable of reproducing experimental data. Precise measurements of (anti)nuclei production and their angular correlations in proton-proton interactions can help achieve the ultimate goal of developing a quantum-mechanical description of the formation process.

Sec. 3.3 discusses how the coalescence model developed by Gomez *et al.* was extended to simulate the production of heavier antinuclei like antitriton, $^3\overline{\mathrm{He}}$, and for the first time, $^4\overline{\mathrm{He}}$.

3.3 New Multiparticle Coalescence Model

As discussed earlier in Sec. 2.4, AMS-02 has recently reported several cosmic antihelium candidate events [82, 83], but thus far, no antideuteron candidates have been reported. These unexpected antihelium observations have spurred an interest in studying the secondary production and propagation of antihelium in our Galaxy. Most of these semianalytical studies have relied on simplified numerical scaling of antiproton production cross sections to predict the production cross sections of heavier antinuclei in typical CR-ISM interactions [35, 91, 150].

This section discusses a different approach, by extending the two-particle coalescence model discussed in the previous section to develop a multiparticle coalescence mechanism. This approach benefits from the continuous improvement of Monte

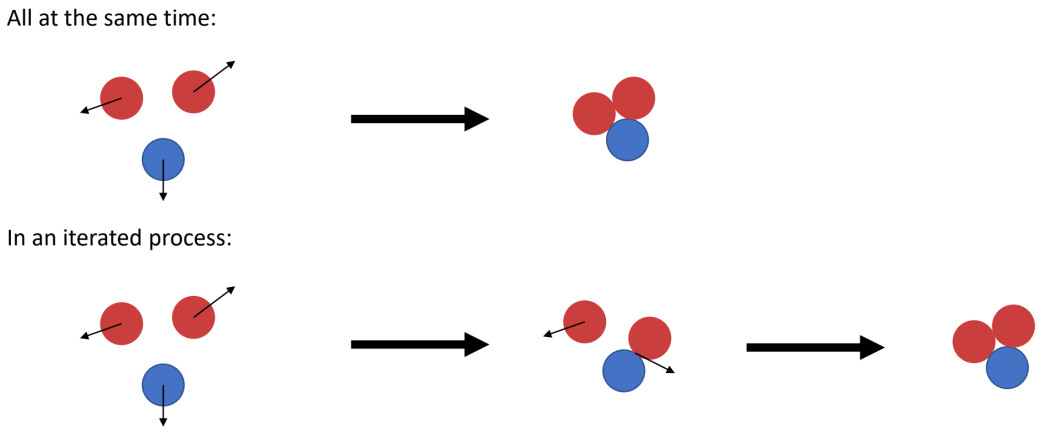

Figure 3.5: Simultaneous (top) and Iterated (bottom) coalescence scenarios for the production of a three-particle nucleus, in the center-of-mass frame of the produced nucleons. Figure adapted from [152].

Carlo (MC) particle interaction simulators, and the availability of high-throughput computational facilities. Utilizing massive computation power of about 10,000 years of single-CPU time, about 100 trillion proton-proton collisions were simulated at different collision energies. The total number of p–A collisions simulated in this study is at least a couple of orders of magnitude more than what was feasible just a few years ago. The new model extends the event-by-event coalescence mechanism of formation of two-particle nuclei (deuterons and antideuterons) to estimate the production of larger antinuclei ($^3\overline{\text{He}}$ and $^4\overline{\text{He}}$). Two simple scenarios were considered:
i) Simultaneous coalescence.—An N-particle antinucleus can be formed by simultaneously coalescing N antiproton and antineutrons, where each antiproton and antineutron pair fulfills the aforementioned coalescence condition (Eq. 3.3). For example, to produce $^4\overline{\text{He}}$, two antiprotons and two antineutrons are selected, and the coalescence condition is evaluated for all six possible combinations of particle pairs.
ii) Iterated coalescence.—Antiprotons or antineutrons are iteratively added to a multiantinucleon state if they fulfill the two-particle coalescence condition. For example, an antideuteron produced by the *simultaneous coalescence* scenario is further evaluated for $^3\overline{\text{He}}$ production, by pairing and evaluating it with all remaining antiprotons in that event. Similarly, $^3\overline{\text{He}}$ is paired with all remaining antineutrons to evaluate for $^4\overline{\text{He}}$ production.

Fig. 3.5 shows these two different scenarios for coalescence of three nucleons. Both these methods were used in this work. The *simultaneous coalescence* method was first used to generate the initial antiparticles, and then the *iterated coalescence* method was used to produce additional antiparticles. The Gomez *et al.* [92] p_0 parametrizations were used in this study to test the hypothesis that a single parameter can accurately describe the formation of heavier antinuclei. This is supported by previous work on the analytical coalescence model, where it was shown that the two-particle coalescence

parameter calculated from $\overline{d}$ production could be scaled to correctly predict the $^{3}\overline{\mathrm{He}}$ production as well [35, 90, 91, 135].

For a systematic study of the dependence of antinuclei production on p_0, seven different values of p_0 for each collision energy were used in this work. These seven values include an initial value of p_0 specific to that kinetic energy, from the $\overline{d}$ parametrization developed by Gomez *et al.* This parametrization is shown in Eq. 3.4. For the rest of this work, this initial value is referred to as $p_{0,G}$. The remaining six values are 70%, 80%, 90%, 110%, 120%, and 130% of $p_{0,G}$.

Proton-proton interactions were simulated at 27 collision energy values, in logarithmic bins between 31 GeV and 12.5 TeV in the laboratory frame. For each collision, a projectile proton moving with the selected energy was collided head on with a stationary proton target. These simulated collisions mimic the interaction of cosmic rays with the interstellar matter. The afterburner was used to implement the coalescence conditions to generate light antinuclei. The number of collisions simulated in each bin was motivated by that bin's relative contribution to the overall source term of the produced antiparticles (see the discussion in Sec. 3.6.1). It was estimated that the contribution to the $\overline{d}$, $^{3}\overline{\mathrm{He}}$, and $^{4}\overline{\mathrm{He}}$ source terms are the largest from the bins at 158, 310, and 400 GeV, respectively. Hence, the bins from 158-500 GeV have the most number of simulated events to get the best estimates of the production cross sections. Further, since p–p collisions contribute 60%-70% of the total antinuclei source terms [35, 45], only those were simulated for this study. The remaining contributions (p–He, He–p, and He–He) were estimated by scaling the parametrization developed in Refs. [68, 91, 153]. The total number of p–p collisions simulated for each energy bin and the number of antiparticles produced per p–p collision by the coalescence mechanism are given in Table 3.1.

3.4 Antinuclei Production Cross Sections

Fig. 3.6 (left) shows the $\overline{p}$ production cross sections calculated in this study in proton-proton collisions as function of collision kinetic energy. These cross sections are also compared to experimental data from Refs. [154, 155] and parametrizations from Winkler [156] and di Mauro [68, 157]. It is visible that the production of antiprotons increases with collision energy and eventually saturates at high energy (approximately 1 TeV). A large gap in the few-hundred GeV range exists in the available $\overline{p}$ production data. Fig. 3.6 (right) shows the production cross section of light antinuclei as a function of collision kinetic energy. As expected, a clear trend is observed that antinuclei production becomes rarer as the number of antinucleons in the final state increases. Fig. 3.7 shows the predicted production yields of $\overline{d}$ and $^{3}\overline{\mathrm{He}}$ as a function of transverse momentum p_{T}, for selected collision energies in the laboratory frame.

Table 3.1: Energy bins, number of generated events per bin, and antiparticles produced per event using the coalescence model at 120% of $p_{0,G}$.

Energy Bins (GeV)	Number of events (billion)	$\overline{d}$	$^3\overline{\mathrm{He}}$	$^4\overline{\mathrm{He}}$
		Particles produced per event		
31	778	8.86×10^{-11}	0	0
40	1284	1.55×10^{-9}	0	0
50	431	1.92×10^{-8}	0	0
60	673	8.54×10^{-8}	0	0
80	583	4.40×10^{-7}	0	0
100	4777	1.13×10^{-6}	3.56×10^{-12}	0
120	3308	2.18×10^{-6}	2.57×10^{-11}	0
158	4032	5.01×10^{-6}	1.73×10^{-10}	2.48×10^{-13}
200	11998	8.98×10^{-6}	5.79×10^{-10}	1.33×10^{-12}
240	6114	1.39×10^{-5}	1.43×10^{-9}	2.78×10^{-12}
310	9061	2.16×10^{-5}	3.55×10^{-9}	5.96×10^{-12}
400	14462	3.09×10^{-5}	7.02×10^{-9}	1.49×10^{-11}
500	7087	3.96×10^{-5}	1.12×10^{-8}	2.61×10^{-11}
600	4024	4.95×10^{-5}	1.72×10^{-8}	3.93×10^{-11}
750	4921	5.94×10^{-5}	2.37×10^{-8}	6.34×10^{-11}
950	2273	7.00×10^{-5}	3.13×10^{-8}	9.32×10^{-11}
1200	1993	8.04×10^{-5}	3.92×10^{-8}	1.13×10^{-10}
1500	1951	9.02×10^{-5}	4.66×10^{-8}	1.39×10^{-10}
1900	1151	1.05×10^{-4}	6.02×10^{-8}	1.77×10^{-10}
2400	2872	1.15×10^{-4}	6.84×10^{-8}	2.25×10^{-10}
3000	2106	1.25×10^{-4}	7.63×10^{-8}	2.51×10^{-10}
3700	2400	1.35×10^{-4}	8.35×10^{-8}	2.67×10^{-10}
4700	790	1.52×10^{-4}	1.01×10^{-7}	3.44×10^{-10}
6000	526	1.64×10^{-4}	1.10×10^{-7}	4.08×10^{-10}
7500	2360	1.75×10^{-4}	1.18×10^{-7}	4.33×10^{-10}
10000	596	1.91×10^{-4}	1.30×10^{-7}	4.83×10^{-10}
12500	911	2.04×10^{-4}	1.39×10^{-7}	4.98×10^{-10}

3.5 Validating the New Multiparticle Coalescence Model

3.5.1 Comparison with $\overline{p}$ production data

The predicted antinuclei fluxes from cosmic-ray propagation models are highly correlated with antiproton production in proton-proton interactions. Hence, it

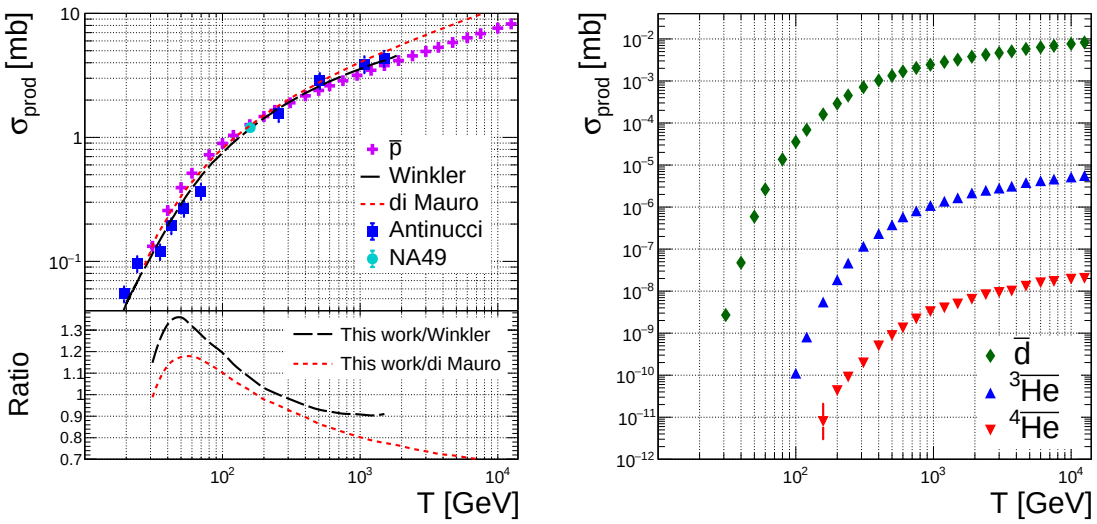

Figure 3.6: Production cross sections calculated in this study for (left) $\overline{p}$ and (right) heavier antinuclei in p–p collisions as function of collision kinetic energy T in the laboratory frame, using the coalescence mechanism at 120% of $p_{0,G}$. The $\overline{p}$ production cross sections are also compared to experimental data from Refs. [154, 155] and parametrizations from Winkler [156] and di Mauro [68, 157]. Details about the choice of the coalescence parametrization are given in Sec. 3.5.2.

is important to base these calculations on correct antiproton production cross sections. The $\overline{p}$ total production cross section as predicted from this simulation was compared with data at different collision energies [154, 155] in Fig. 3.6 (left). This EPOS-LHC-based simulation was found to be compatible with the total cross section measurements within the uncertainties. Next, the $\overline{p}$ differential production cross section as function of kinetic energy was compared to the latest parametrization at different collision energies. Fig. 3.8 shows the comparison for collisions at 20 and 450 GeV/c. The agreement with parametrization from di Mauro *et al.* is poor for 20 GeV/c interactions but gets much better at 450 GeV/c. The agreement at very low kinetic energies is especially poor. The parametrization from Korsmeier *et al.* [149] shows only the primary $\overline{p}$ cross section and does not include the contribution from $\overline{n}$ decay; therefore it is lower than the di Mauro *et al.* parametrization [157] used by Poulin *et al.* [91] by a factor of 2. Taking this factor into account, the cross section predicted by EPOS-LHC in this work is in good agreement with Ref. [149].

3.5.2 Validation with $\overline{d}$, $\overline{t}$ and $^3\overline{\mathrm{He}}$ production data

Because of a lack of light-antinuclei production data for p–p collisions at low energies near the production thresholds, a direct comparison with the predictions of the multiparticle coalescence model is not possible at this time. However, comparison

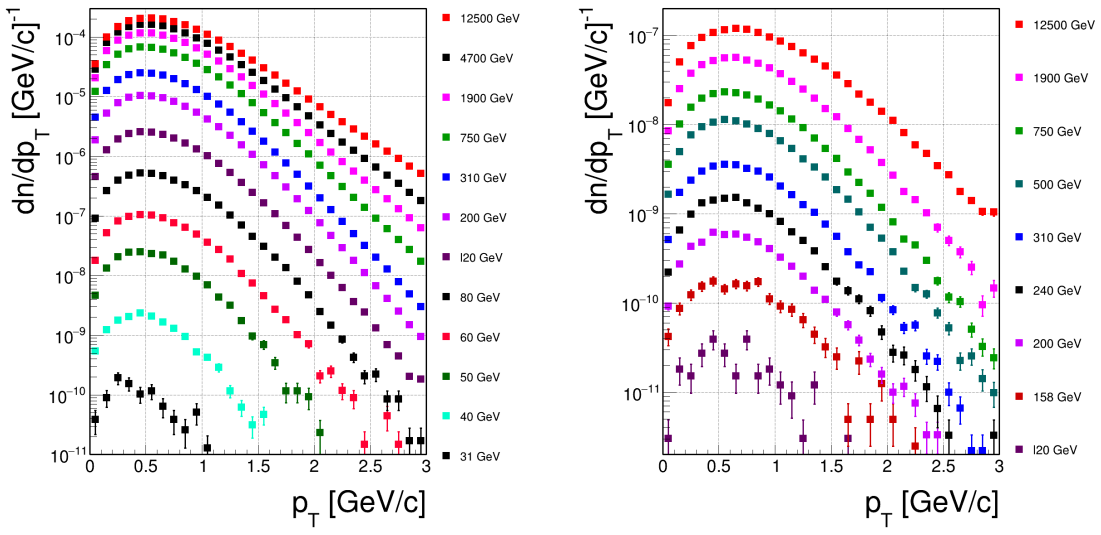

Figure 3.7: Antinuclei spectra produced in p–p interactions via the coalescence mechanism as a function of its transverse momentum p_{T} are shown for selected CR energies (laboratory frame), using the coalescence mechanism at 120% of $p_{0,G}$: (left) $\overline{d}$ spectra and (right) $^3\overline{\mathrm{He}}$ spectra. Details about the choice of the coalescence parametrization are given in Sec. 3.5.2.

with p–A collisions (where A is a nucleus) can produce a target-independent parametrization for the production of light antinuclei. $\overline{t}/\overline{p}$ and $^3\overline{\mathrm{He}}/\overline{p}$ ratios have been measured in p–Al and p–Be collisions at beam momentum of 200 GeV/c in the WA33 experiment at CERN-SPS [158–160]. The predictions of this model are compared to data in Fig. 3.9. The model was employed in its existing form, without conducting any additional fits to new data. The uncertainty bands were estimated by varying the coalescence parameter from $p_{0,G}$ (59 MeV/c) to 130% of $p_{0,G}$ (77 MeV/c). In both magnitude and shape, it nearly overlaps with the uncertainty band from the analytical model (Eq. 3.2) used in [160], and is also in good agreement with the data.

Proton-proton collisions were also simulated at $\sqrt{s} = 7$ TeV, with the aim of comparing the updated coalescence scheme with the latest $^3\overline{\mathrm{He}}$ production data from ALICE [161]. The coalescence parameter p_0 was again varied from $p_{0,G}$ (90 MeV/c) to 130% of $p_{0,G}$ (116 MeV/c) to simulate an uncertainty band. The results are shown in Fig. 3.10. The $^3\overline{\mathrm{He}}$ and $\overline{t}$ production yields are within 10%–30% of the yield predicted by using $p_{0,G}$. Moreover, as found by ALICE and in Ref. [162], the simulation also shows no measurable asymmetry in antitriton and antihelium production at very high energies.

Since the development of the $\overline{d}$ parametrization in Ref. [92], new data for $\overline{d}$ production at $\sqrt{s} = 13$ TeV have been published by ALICE [163]. Comparison of the data with the predictions from the coalescence model is shown in Fig. 3.11 (left). Once again, the uncertainty band was estimated by varying the coalescence parameter from $p_{0,G}$

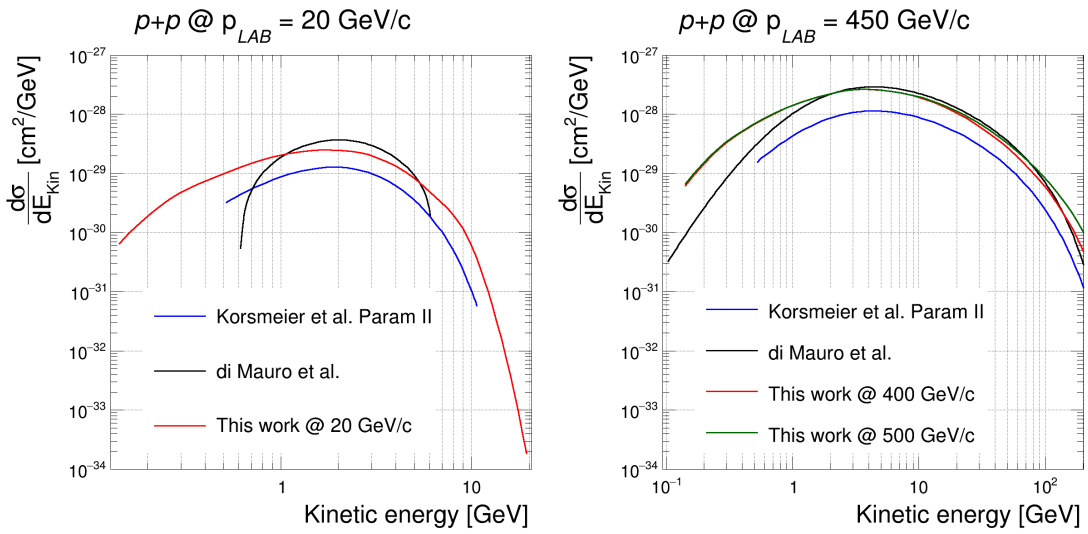

Figure 3.8: The antiproton differential production cross section as function of kinetic energy E_{Kin} for (left) p–p at $p_{\mathrm{lab}} = 20\,\mathrm{GeV}/c$ and (right) p–p at $p_{\mathrm{lab}} = 450\,\mathrm{GeV}/c$. The results are compared to parametrization from di Mauro *et al.* [157] and Korsmeier *et al.* [149]. The parametrization from Korsmeier *et al.* does not include the contribution from decay of antineutrons.

($90\,\mathrm{MeV}/c$) to 130% of $p_{0,G}$ ($116\,\mathrm{MeV}/c$). The $\overline{d}$ production yield from ALICE is found to be within 10%–20% of the yield predicted by using $p_{0,G}$ as the coalescence momentum, demonstrating the predictive power of the updated model for cosmic-ray studies.

As discussed in Sec. 3.3, the production cross sections for $\overline{d}$, $^3\overline{\mathrm{He}}$, and $^4\overline{\mathrm{He}}$ at each collision energy were estimated at seven different values of the coalescence parameter p_0. The parametrization in Eq. 3.4 was used to get the initial value of p_0 (i.e., $p_{0,G}$), and the other p_0 values were used to estimate the uncertainty bands. However, as shown above, using $p_{0,G}$ as the coalescence parameter underpredicted the $^3\overline{\mathrm{He}}$ production cross sections by 10%–20% for both high and low interactions. To take this into consideration, the subsequent $^3\overline{\mathrm{He}}$ and $^4\overline{\mathrm{He}}$ production cross sections and the CR flux discussions are shown with an uncertainty band with the lower edge corresponding to $p_{0,G}$ and the upper edge corresponding to 130% of $p_{0,G}$. The uncertainties in the $\overline{d}$ parametrization from Ref. [92] are also similar in magnitude, especially in the low-energy region (collision kinetic energy of approximately ~100 GeV) relevant for $\overline{d}$ production in cosmic-ray interactions. Along with the comparison to data at $\sqrt{s} = 13\,\mathrm{TeV}$ as discussed above, and to be consistent with the other antinuclei, a similar uncertainty band (from $p_{0,G}$ to 130% of $p_{0,G}$) was chosen for $\overline{d}$ as well. This effectively shifts the value of parameter A in Eq. 3.4 by 15%, from 90 to $103\,\mathrm{MeV}/c$.

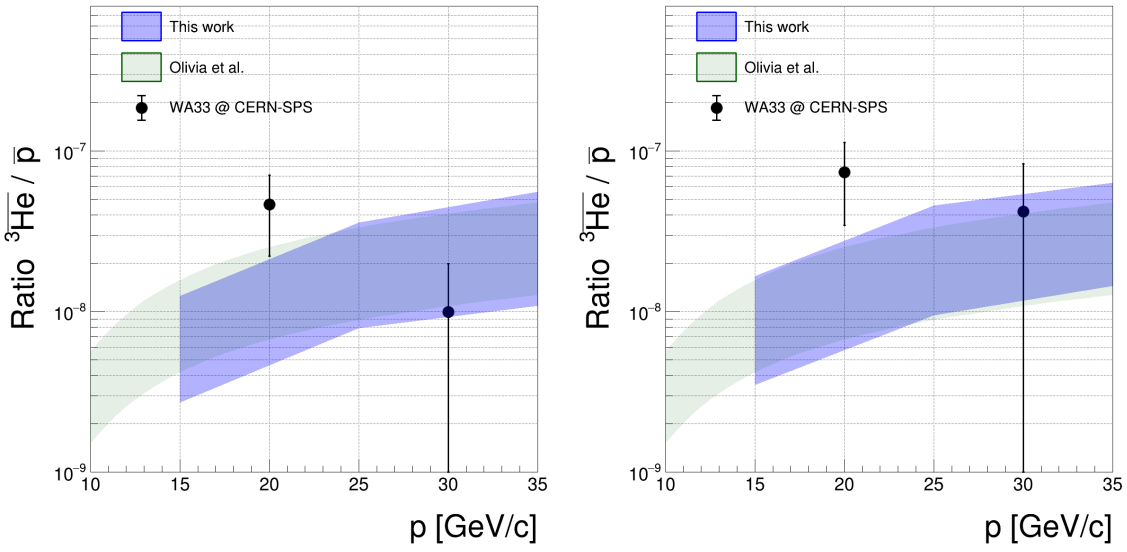

Figure 3.9: The invariant production cross section ratio $^3\overline{\mathrm{He}}/\overline{p}$ as function of momentum p [GeV/c] in the laboratory frame for (left) p–Be at $p_{\mathrm{lab}} = 200\,\mathrm{GeV}/c$ and (right) p–Al at $p_{\mathrm{lab}} = 200\,\mathrm{GeV}/c$ [158–160]. The uncertainty bands for this work were estimated by varying the coalescence parameter from $p_{0,G}$ (59 MeV/c) to 130% of $p_{0,G}$ (77 MeV/c).

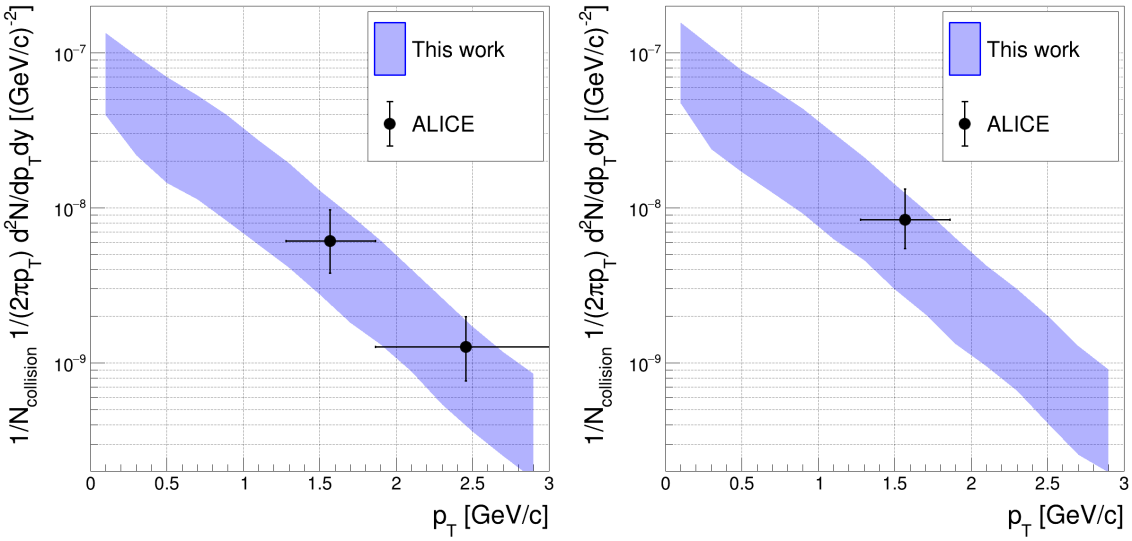

Figure 3.10: Number density of (left) $^3\overline{\mathrm{He}}$ and (right) $\overline{t}$ production from coalescence mechanism for p–p interactions at $\sqrt{s} = 7\,\mathrm{TeV}$, along with ALICE results from Ref. [161]. The uncertainty bands were estimated by varying the coalescence parameter from $p_{0,G}$ (90 MeV/c) to 130% of $p_{0,G}$ (116 MeV/c).

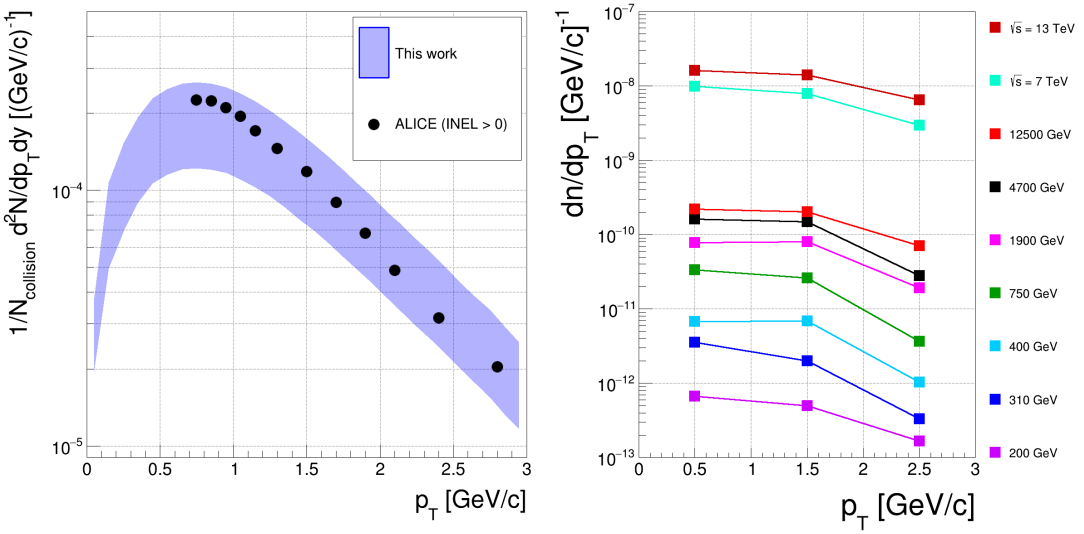

Figure 3.11: Left: number density of $\overline{d}$ production from coalescence mechanism for p–p interactions at $\sqrt{s} = 13\,\text{TeV}$, along with ALICE results from Ref. [163]. The uncertainty band was estimated by varying the coalescence parameter from $p_{0,G}$ ($90\,\text{MeV}/c$) to 130% of $p_{0,G}$ ($116\,\text{MeV}/c$). Right: the predicted differential yield of $^4\overline{\text{He}}$ as a function of p_T in p–p interactions at different collision energies, using the coalescence mechanism at 120% of $p_{0,G}$. Details about the choice of the coalescence parametrization are given in Sec. 3.5.2.

Finally, this study marks the first instance of successfully simulating a sufficient number of p–p collisions to generate $^4\overline{\text{He}}$ spectra using the coalescence mechanism. As a result, this model holds potential for characterizing the formation of diverse light antinuclei across small collision systems in a broad energy range, using a single energy-dependent coalescence parameter. The model offers important predictions that can be compared to data from future collider experiments when they become available. Fig. 3.11 (right) shows the $^4\overline{\text{He}}$ production yield as a function of p_T predicted by this study at different collision energies, including at $\sqrt{s} = 7$ and 13 TeV. ALICE has published results of $^4\overline{\text{He}}$ production in Pb–Pb collisions at $\sqrt{s} = 2.76\,\text{TeV}$ [164] and $^4\overline{\text{He}}$ production upper limit in p–Pb collisions at $\sqrt{s} = 5.02\,\text{TeV}$ [165]. However, p–Pb and Pb–Pb collisions differ significantly from p–p collisions, especially at LHC energies. Pb–Pb collisions comprise a larger number of nucleons, resulting in higher energy densities and the potential formation of a quark-gluon plasma. The larger system size in Pb–Pb collisions also leads to collective effects, such as flow patterns and anisotropic expansion, which are absent in p–p collisions. Additionally, the increased complexity of initial geometries and a higher probability of final-state interactions in Pb-Pb collisions give rise to phenomena like jet quenching [166–168]. In addition to the large disparities in system size and collision energy, they have different (anti)nuclei production threshold energies and potentially different production mechanisms. Therefore, these ALICE results should not be used

to validate the predictions of the p–p MC simulations in this work. Instead, these predictions can be compared to future p–p measurements to further validate or refine the model.

Measuring the antideuteron and antihelium production at LHC energies is very useful to validate various formation models, but cosmic rays at LHC energies are extremely rare, with most cosmic-ray protons having an energy of only a few GeVs. Using systems with collision energies closer to the production threshold of light antinuclei is necessary to understand their production in the Galaxy [41].

3.6 Propagation of Antinuclei in the Galaxy

Galactic CRs mainly propagate via two processes: diffusion due to scattering on interstellar turbulence, and convection by Galactic winds. CR particles lose energy by hadronic interactions such as pion production and ionization, and also due to inelastic collisions and radioactive decay. The Fokker-Planck equation describes CR propagation as:

$$\frac{\partial \psi}{\partial t} = Q(\boldsymbol{r}, p) + \mathbf{div}(D_{\mathrm{xx}}\mathbf{grad}\psi - \boldsymbol{V}\psi) + \frac{\partial}{\partial p}p^2 D_{\mathrm{pp}}\frac{\partial}{\partial p}\frac{\psi}{p^2} - \frac{\partial}{\partial p}\left[\psi\frac{\mathrm{d}p}{\mathrm{d}t} - \frac{p}{3}(\mathbf{div}\cdot\boldsymbol{V})\psi\right] - \frac{\psi}{\tau}, \qquad (3.5)$$

where $\psi = \psi(\boldsymbol{r}, p, t)$ is the time-dependent CR density per unit of the total particle momentum at position $\boldsymbol{r}$, $Q(\boldsymbol{r}, p)$ is the source term of the cosmic rays which can include primary CRs injected by supernova remnants, secondary CRs coming from spallation and cosmic-ray collisions with the ISM, as well as more exotic sources such as dark-matter annihilation. The propagation parameters D_{xx}, $\mathbf{V}$, and D_{pp} are the spatial diffusion coefficient, the convection velocity, and the diffusive re-acceleration coefficient, respectively. ψ/τ accounts for CR particles lost via decay, fragmentation and inelastic interactions with the ISM [43]. The modulation effects due to the magnetic fields of the Sun and Earth become significant for CRs which have kinetic energy per nucleon of about 1 GeV/nucleon [169]. They have to be treated separately using the Force Field approximation [170] or with special codes such as HelMod [171, 172].

The standard technique to estimate the source term $\mathrm{Q_{sec}}$ for antinuclei production in the interactions of CRs with ISM is by scaling the parametrization of $\overline{p}$ production cross section data from experiments. In this work, the production cross sections of all the antinuclei were generated using the results from the large-scale event-by-event simulations described above. The calculated $\overline{d}$, $^3\overline{\mathrm{He}}$, and $^4\overline{\mathrm{He}}$ differential production cross sections are presented in Fig. 3.12. It was assumed that all antitritons decay completely into $^3\overline{\mathrm{He}}$ over the timescale of Galactic transport, with no change in their kinetic energy distribution. Since p–p collisions contribute 60%-70% of the total antinuclei source terms [35, 45], only those were simulated. Contributions from the p–He, He–p, and He–He channels were estimated by scaling the antinuclei spectra

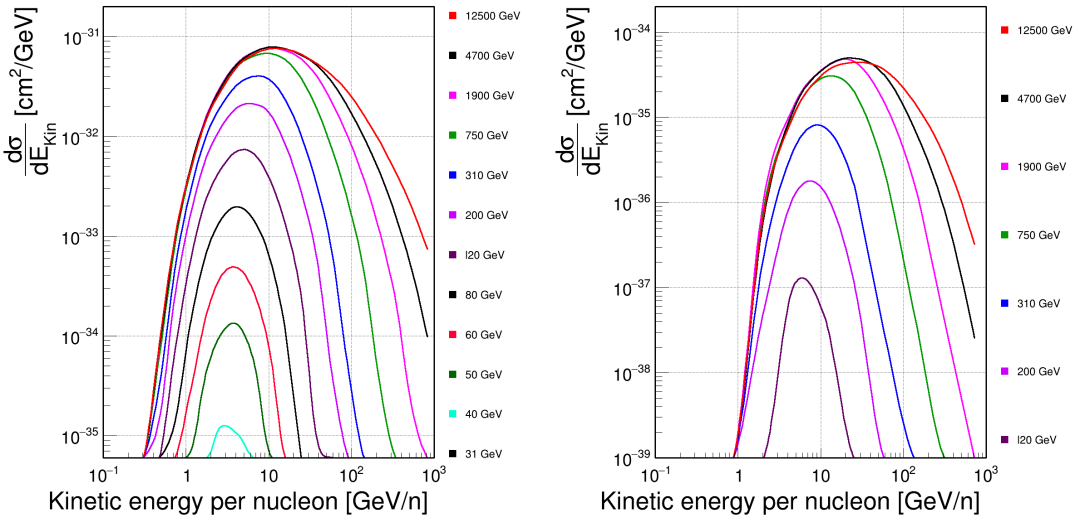

Figure 3.12: Differential production cross section ($\mathrm{cm}^2/\mathrm{GeV}$) for (left) $\overline{d}$ and (right) $^3\overline{\mathrm{He}}$ as function of kinetic energy per nucleon E_{Kin} (GeV/n) for selected p–p collision energies, using the coalescence mechanism at 120% of $p_{0,G}$. Details about the choice of the coalescence parametrization are given in Sec. 3.5.2.

obtained from the large-scale p–p simulations, using the scaling relations developed in Refs. [68, 91, 153]. For example, the $p+p \to \bar{d}+X$ cross sections were multiplied by $(A_T A_P)^{2.2/3}$, where A_P and A_T are the nucleon numbers of the projectile and target nuclei. The local source term $\mathrm{Q}_{\mathrm{sec}}$ was then calculated using [91, 173, 174]:

$$\mathrm{Q}_{\mathrm{sec}}(E_{\mathrm{A}}) = 4\pi n_{\mathrm{H}} \int_{E_{th}}^{\infty} \mathrm{d}E \phi_p(E) \frac{\mathrm{d}\sigma_{\mathrm{A}}}{\mathrm{d}E_{\mathrm{A}}}(E, E_{\mathrm{A}}), \tag{3.6}$$

where E_{th} is the production threshold energy, and n_H is the number density of hydrogen nuclei in the ISM which was set to 0.9 atoms/cm^3. The flux of CR protons $\phi_p(E)$ at the selected energies were obtained from the high-precision measurements by the AMS-02 collaboration [62]. The differential production cross section of an antinucleon A as a function of its kinetic energy per nucleon E_{A} was obtained from the large-scale MC simulations.

The calculated secondary antiparticle source terms for different antiparticles as a function of kinetic energy per nucleon are presented in Fig. 3.13 (left). Both $\overline{d}$ and $^3\overline{\mathrm{He}}$ source terms are lower than the source terms predicted by Poulin *et al.* [91] by an order of magnitude in the low kinetic energy region (less than 10 GeV). Because of low statistics (see Table 3.1), the $^4\overline{\mathrm{He}}$ source term is shown only from 4–20 GeV, where it is in agreement with Poulin *et al.* As $^4\overline{\mathrm{He}}$ production is extremely rare in p–p collisions, being able to predict the $^4\overline{\mathrm{He}}$ source term using MC simulations was only possible with a massive amount of computing power.

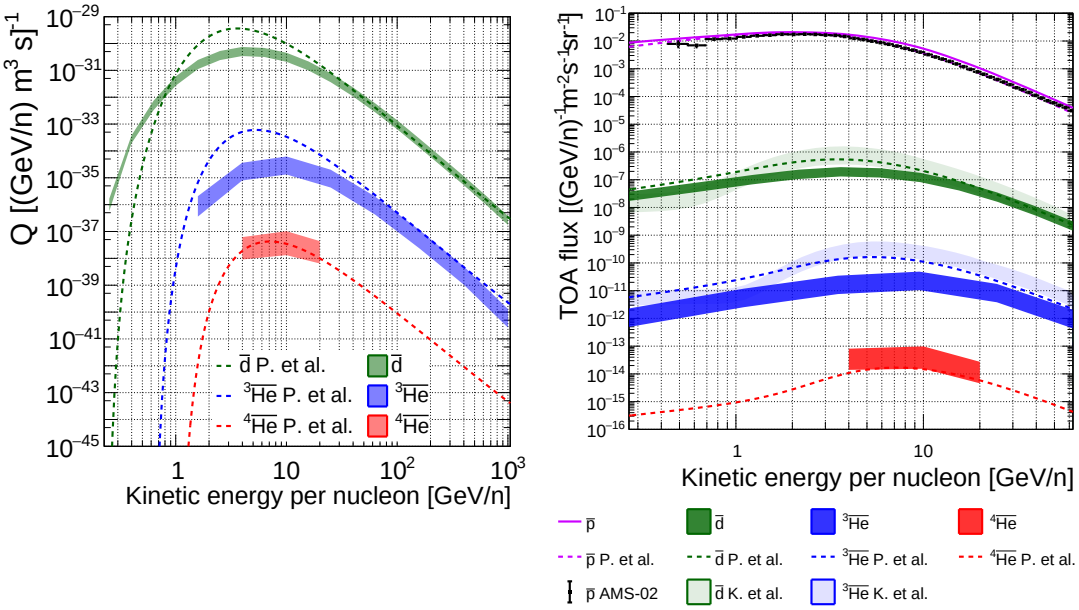

Figure 3.13: Left: local source terms for the secondary production of $\overline{d}$, $^3\overline{\mathrm{He}}$, $^4\overline{\mathrm{He}}$. The width of the bands represent uncertainty in the coalescence parameter, which was varied from $p_{0,G}$ to 130% of $p_{0,G}$. These predictions are compared to predictions by Poulin *et al.* [91] and Korsmeier *et al.* [35]. Right: the predicted secondary top-of-atmosphere flux for different antiparticles, propagated using the MED propagation model [175]. The width of the bands from this work represents uncertainty in the coalescence parameter. These predictions are compared to predictions by Poulin *et al.* [91] and Korsmeier *et al.* [35]. The $\overline{p}$ flux is compared to data from AMS-02 [62].

This was followed by the propagation of the source terms in the Galaxy. To propagate the antinuclei produced in interstellar medium, an updated semianalytical code developed in Refs. [91, 176, 177] was used. The only difference is the modification of $\overline{p}$, $\overline{d}$, and $\overline{\mathrm{He}}$ production cross section tables for p–p interactions, with tables generated using the coalescence model from this work. The diffusion parameters used for Galactic propagation in this study were not tuned to fit the $\overline{p}$ flux from this analysis with CR data. Instead, the parameters from Poulin *et al.* [91] were used with the MED propagation model [175] to predict the secondary antinuclei fluxes. Solar modulation was applied to produce the final top-of-the-atmosphere (ToA) fluxes.

3.6.1 Predicted Secondary Cosmic-ray Fluxes

The predicted antinuclei fluxes are shown in Fig. 3.13 (right). The uncertainty bands shown for the fluxes from this work are due to the uncertainty in the coalescence parameter, which was varied from $p_{0,G}$ to 130% of $p_{0,G}$. For comparison, the predicted

fluxes from Poulin *et al.* [91] and Korsmeier *et al.* [35] and $\overline{p}$ data from AMS-02 [62] are also shown.

The $\overline{p}$ flux predicted by this study exceeds the AMS-02 data by 20%–30% in the low kinetic energy region (1–5 GeV). This can be understood by looking at the comparison between the $\overline{p}$ production cross sections used in this work (from `EPOS-LHC`) and the di Mauro parametrization used by Poulin *et al.* (Fig. 3.6). The differences in the low-energy region (below a few hundred GeVs in the laboratory frame) are especially important. Fig. 3.6 (bottom left) shows that the $\overline{p}$ production cross section ratios of `EPOS-LHC` to the di Mauro parametrization reaches up to 1.2 for these low-energy collisions. Since low-energy collisions are the dominant source of antinuclei production in cosmic-ray interactions, the overproduction in `EPOS-LHC` in this region is the major reason behind the excess $\overline{p}$ flux predicted by this study. In future, this can be fixed by further tuning of the `EPOS` model using new $\overline{p}$ production data from p–p collisions at lower energies. These measurements are discussed in Chapter4.

It is important to note that the p_0 parametrization of Gomez *et al.* [92] for $\overline{d}$ production, which has been extended and improved in this work for $\overline{\text{He}}$ production, already absorbs any differences between the $\overline{p}$ production in `EPOS-LHC` and experimental data. This is because the p_0 is extracted by directly fitting to $\overline{d}$ and $\overline{\text{He}}$ data. Hence, even if the excess $\overline{p}$ production in `EPOS-LHC` is corrected so that the calculated $\overline{p}$ flux discussed above matches AMS-02 data, the calculated fluxes of the other heavier antinuclei shown in Fig. 3.13 (right) will not be affected by this correction.

The predicted secondary $\overline{d}$ flux is very close to the predicted flux from [91]. The predicted secondary $^3\overline{\text{He}}$ flux is consistently lower than the corresponding fluxes from both [91] and [35] by almost an order of magnitude, especially in the low kinetic energy region between 1 and 10 GeV. As discussed in Sec. 3.6, the predicted $^4\overline{\text{He}}$ flux is shown only from 4–20 GeV, and it agrees with [91] within the uncertainties.

The differences in the antinuclei fluxes between this study and Ref. [91] can be traced to the differences in the source terms in Fig. 3.13 (left). The $\overline{d}$ and $^3\overline{\text{He}}$ source terms are both smaller than the source terms in Ref. [91]. This reduction observed at lower energies is a consequence of the energy-dependent p_0. The $^4\overline{\text{He}}$ source term is about the same within the uncertainties. However, due to the lack of experimental data for $^4\overline{\text{He}}$ production, the validity of the multiparticle coalescence model could not be evaluated for this regime.

3.6.2 Comparison With Other Coalescence Models

The $\overline{d}$ production cross sections from the new model (Fig. 3.12 Left) were used in a study [43] to calculate the most up-to-date $\overline{d}$ flux predictions by including an estimate for the loss of $\overline{d}$ during galactic propagation. The uncertainties from the multiparticle

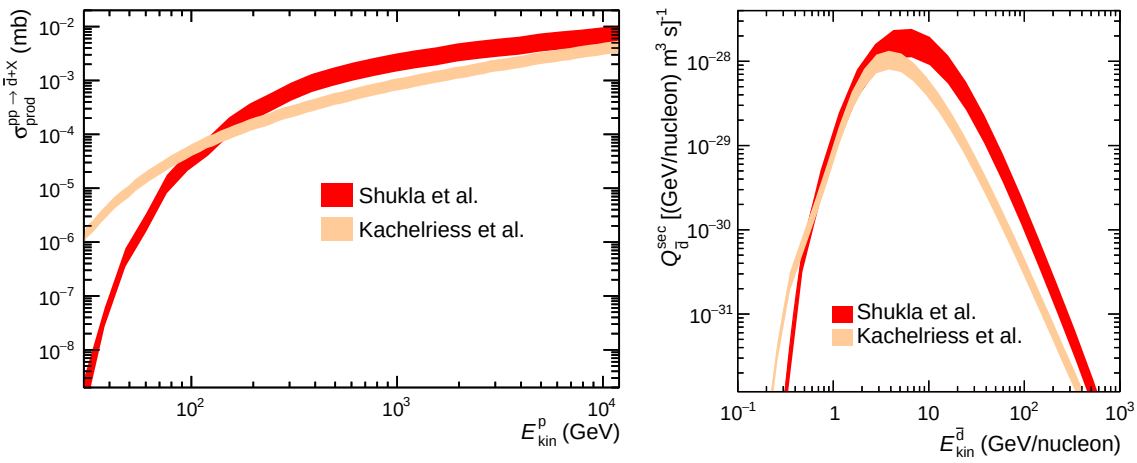

Figure 3.14: Left: Antideuteron total production cross section, in p–p collisions, as a function of the projectile kinetic energy E^{p}_{kin} (GeV) in the laboratory frame for two models [92, 93] and [178]. The band width corresponds to the uncertainty of the coalescence parameter. Right: Antideuteron source term, integrated over proton, helium and antiproton fluxes, as a function of its kinetic energy per nucleon for the two models. Figures adapted from [43].

coalescence model were important to bracket the uncertainty in the expected ToA fluxes. This study also compared the multiparticle coalescence model developed in this study with the coalescence model developed by Kachelrieß et al. [179]. This new coalescence model is based on the Wigner function representations of the produced nuclei states in a semi-classical picture. This includes the momentum correlations of coalescing antinucleons, as well as the process-dependent size of the antinuclei formation region.

The comparisons of the $\overline{d}$ production cross sections in p—p collisions, and the $\overline{d}$ local source term is shown in Fig. 3.14. The differences between the two approaches is likely due to the use of different event generators, as Kachelrieß et al. used the QGSJET-II model to simulate $\overline{d}$ production in p–H, p–He, He–p, and also $\bar{p}$–p and $\bar{p}$–He collisions. The smaller cross sections obtained by Kachelrieß et al. around 1000 GeV may be related to the underproduction of antinucleons in `QGSJET-II` at those energies. The two approaches also used slightly different data sets to parametrize the $\overline{d}$ production cross sections. Therefore, the discrepancies between the two source terms, where the two secondary source term predictions often do not overlap within their uncertainty bands, are a direct consequence of the mismatch in the production cross sections. The upper limit from the multiparticle coalescence model is up to 7 times larger than the lower limit from Kachelrieß et al. This results in the differences seen in the predicted secondary $\overline{d}$ flux by the two models, shown in Fig. 3.15.

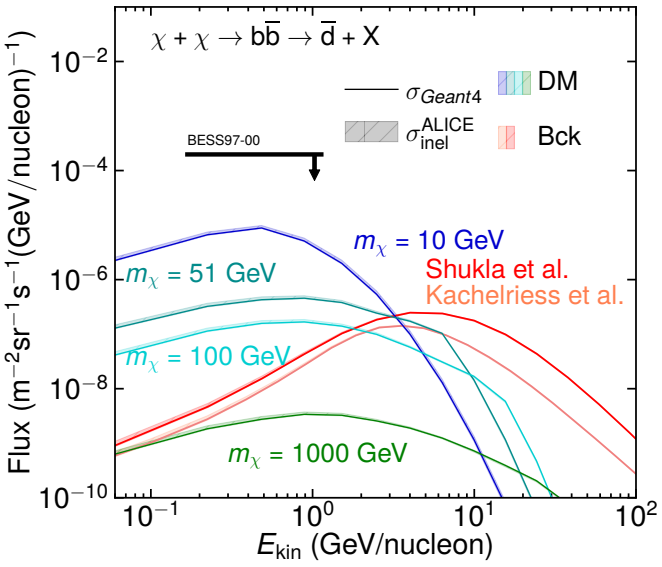

Figure 3.15: Antideuteron fluxes expected at Earth predicted from CR interactions with the ISM, from this dissertation and from Kachelrieß et al. [179]. A selected production scenario show antideuterons from dark-matter annihilation into $b\bar{b}$, for several hypothetical dark matter particle masses, using antideuteron spectra determined by [26]. Only uncertainties accounting for the inelastic cross section $\sigma^{\bar{d}}_{inel}$are shown. Figure adapted from [43].

However, despite these differences, the figure emphasizes the significance of a low-energy antideuteron search, particularly for decay signatures from dark matter candidates with a mass around 100 GeV. Finally, the comparison between these two coalescence models indicates that the uncertainty in the modeling of $\overline{d}$ formation mechanism is even more important than the uncertainty in the determination of coalescence parameters within any given coalescence model. This underscores the requirement of more measurements of $\overline{p}$ and $\overline{d}$ production cross sections in p–p and p–He collisions, to tune hadronic event generators and improve antinuclei formation modeling.

Chapter 4
Measurement of Charged Hadron Production in NA61/SHINE

4.1 Motivation for New Measurements

Ultra-high energy measurements from CERN's Large Hadron Collider (LHC) experiments, such as ALICE, operating at the TeV scale, have greatly enhanced our knowledge of antinuclei formation and their interactions. However, these measurements alone cannot provide a comprehensive picture of the entire energy landscape. As emphasized in previous chapters, a better understanding of antinuclei formation in p–p interactions between 50–400 GeV/c is crucial to boost the interpretation of cosmic-ray antinuclei measurements.

These lower-energy measurements are essential to build and validate hadron formation models in high-energy physics across a wide range of energies. The formation of (anti)deuterons is tightly coupled to the production of (anti)protons. Hence, it is essential to first validate the output of hadronic generators with (anti)proton measurements. As was shown in [92], available hadronic generators do not describe the measured antiproton production cross sections particularly well, for both overall yield and spectral shape. `EPOS-LHC` [140] exhibits the best agreement with the available data sets, but still shows an average deviation of about two standard deviations. Fig. 3.6 (left) shows a large gap in the available $\overline{p}$ production cross section data in the few-hundred GeV range, which is the dominant region for antinuclei production in CR interactions.

As described in Sec. 3.2, the two most common models to describe antinuclei production are the coalescence and thermal models, but they are based on different underlying physics. Most data that were used for the development of the modified coalescence model described in the previous chapters dates back several decades. Even worse than for $\overline{p}$, there are very few data points for deuteron and particularly antideuteron production cross sections in p-p interactions at low collision energies. One $\overline{d}$ data point at $p_{\text{lab}} = 70\,\text{GeV}/c$ [180] is followed by the next available data

only at $p_{\text{lab}} = 1500\,\text{GeV}/c$. The antinuclei production in CR interactions steeply increases between collisions at 50 to $400\,\text{GeV}/c$. The lack of collider measurements in this regime leads to discrepancies in the predicted yields between commonly-used hadronic generator models like `FTFP-BERT` [143] and `EPOS-LHC`. This leads to order-of-magnitude uncertainties in the predicted astrophysical antinuclei flux received at Earth. New data with larger statistics from modern experiments are necessary for the reduction of these large statistical and systematic uncertainties.

Complementing LHC experiments with measurements at lower energies, such as those conducted at CERN's Super Proton Synchrotron (SPS), can offer several other benefits as well. The lower-energy experiments can contribute to the understanding of the QCD (Quantum Chromodynamics) phase diagram, as they can probe the regions of the diagram that are not accessible at LHC energies. This can help in studying the transition from non-perturbative to perturbative QCD regimes, as well as phase transitions between hadronic matter and the Quark-Gluon Plasma (QGP), including its formation and evolution. Such studies are important for understanding the nature of strongly interacting matter. Combining measurements from ultra-high energy experiments like ALICE with experiments at lower energies provides a more comprehensive understanding of the fundamental interactions and properties of matter across a wide range of energies [181, 182]. Therefore, for a variety of reasons, more measurements of the (anti)proton and (anti)deuteron production cross sections in the low-energy region near the antinuclei production thresholds are crucial.

The fixed-target experiment NA61/SPS Heavy Ion and Neutrino Experiment (NA61/SHINE) at the SPS at CERN [121] is ideally suited to address these needs, because it studies the collision of nuclei with different targets over a range of incident beam momentum of 9–$400\,\text{GeV}/c$. So far, NA61/SHINE has published proton and antiproton production yields in p–p interactions only from the low-statistics data sets at $p_{\text{beam}} = 20$, 31, 40, 80 and $158\,\text{GeV}/c$ [121, 181]. These results have already been used in a number of cosmic-ray related studies [69, 71, 92, 149, 183], clearly highlighting the importance of ground-based measurements for CR data interpretation. The latest p–p data sets at incident proton beam momenta of 158 and $400\,\text{GeV}/c$ ($\sqrt{s} = 17.3$ and 27.4 GeV, respectively) are more than a factor of ten larger than the earlier 2009 data sets [181], and can help in reducing the statistical uncertainties in the previous analysis by more than a factor of 3.

This chapter presents the preliminary measurements of proton and antiproton spectra using the high-statistics proton-proton data sets at p_{beam} of $158\,\text{GeV}/c$ from NA61/SHINE. The first deuteron production measurements at this collision energy are also presented. The high-statistics data allows to significantly extend the phase space coverage in rapidity and transverse momentum, as compared to previous results from NA61/SHINE. Moreover, $\pi^{\pm}$ and $K^{\pm}$ spectra were also obtained as byproducts of this analysis, which are important for studies of strongly interacting matter.

Sec. 4.2 provides an an overview of NA61/SHINE, describing the experimental setup and detector subsystems. Data preparation for calibration and reconstruction, and detector simulation are described in Sec. 4.3. Sec. 4.4 shows how clean, well-reconstructed collision events and particle tracks are selected for analysis by applying a series of quality cuts, and how charged-particle identification (PID) is performed. It also shows how the detected particle counts are corrected for detector effects like background contributions, geometrical acceptance, and detector efficiencies. Finally, the estimation of statistical and systematic uncertainties is shown. Sec. 4.4.6 presents the new results, as well as comparisons to previous results and the `EPOS-LHC` model.

4.2 Introduction to NA61/SHINE

NA61/SHINE (SPS Heavy Ion and Neutrino Experiment) is a fixed-target large-acceptance hadron spectrometer. It is a multi-purpose facility designed to measure particle production in nucleus+nucleus, hadron+nucleus and p–p interactions over a wide incident beam momentum range (9 to 400 GeV/c) for various physics goals The detector is situated at the CERN-SPS in the H2 beamline of the North experimental area. [181, 182, 184].

Fig. 4.1 shows a schematic diagram of the NA61/SHINE detector setup. The four large volume Time Projection Chambers (TPC) are the main components of the charged-particle detection system. Two of them are called Vertex TPCs (VTPC), and are located downstream of the target inside superconducting magnets. The magnets have a maximum combined bending power of 9 Tm. The magnetic field can be scaled in proportion to the beam momentum in order to maximize the phase space acceptance at all momenta. The main TPCs (MTPC) and two walls of pixelated Time-of-Flight (ToF-L/R) detectors are placed symmetrically to the beamline, downstream of the magnets. The fifth small TPC (GAP-TPC) is placed between VTPC1 and VTPC2 directly on the beam line. The TPCs are filled with Ar:CO_2 gas mixtures in proportions 90:10 for the VTPCs and the GAP-TPC, and 95:5 for the MTPCs.

The Projectile Spectator Detector (PSD), which measures mainly the energy in the forward region of projectile spectators, is positioned downstream of the target. A set of scintillation and Cherenkov counters, as well as three beam position detectors (BPDs) placed upstream of the target provide timing reference, identification and position information of the incoming beam particles. After the beam particle interacts within the target, the produced charged particles can be tracked and identified with the measurement of specific energy loss ($\mathrm{d}E/\mathrm{d}x$) in different TPCs, and can be augmented by time-of-flight (tof) measurements using the ToF detectors.

Two types of analyses were conducted. The first analysis used the $\mathrm{d}E/\mathrm{d}x$ measurements in the TPCs to extract particle yields. The second tof–$\mathrm{d}E/\mathrm{d}x$ analysis

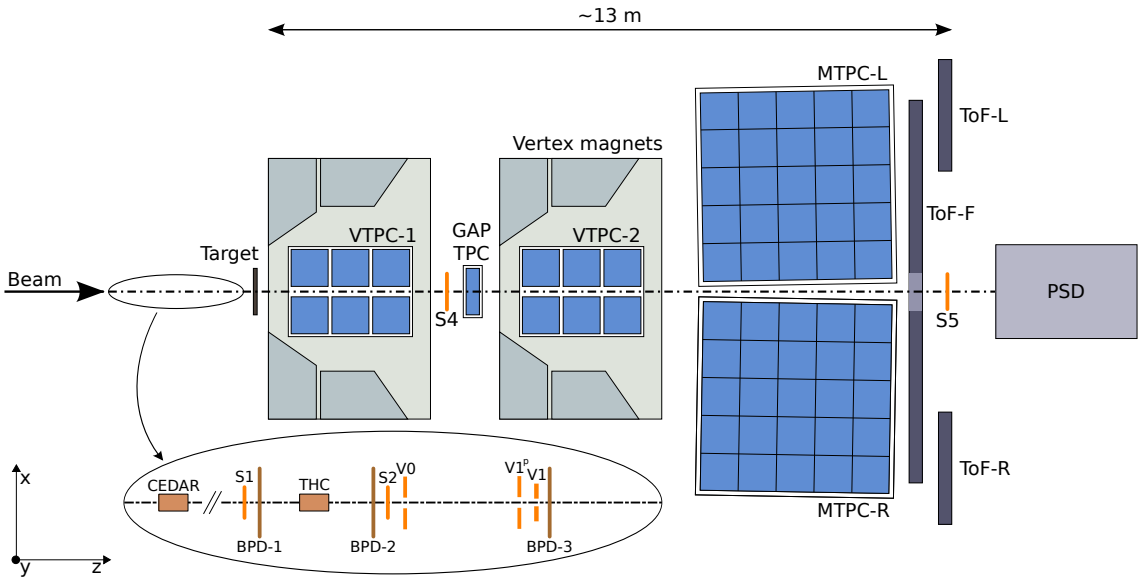

Figure 4.1: Schematic layout of the NA61/SHINE facility at the CERN-SPS [184] (horizontal cut, not to scale). The beam instrumentation is sketched in the inset. Alignment of the NA61/SHINE coordinate system is shown in the figure, with the origin in the middle of VTPC-2, on the beam axis. The nominal beam direction is along the z-axis. The magnetic field bends charged particle trajectories in the x–z (horizontal) plane. The electron drift direction in the TPCs is along the y (vertical) axis.

combined the dE/dx information from the TPCs with the time-of-flight information from the ToF detectors. The added information from ToF removes the ambiguity in the identification of low momentum tracks (4-10 GeV).

4.2.1 Beam counters and trigger system

This section briefly describes the beam counters, trigger system, and detector subsystems in NA61/SHINE [184]. The description focuses on those detectors which were used for the charged-particle identification in the analysis of the p–p data sets. To monitor the incident particle beam, upstream beam counters are used to provide information about the beam properties and position. To minimize beam interactions with these counters, their properties like size and material type are carefully selected. An example set of plastic (BC-408) scintillator beam counters that were used during the p–p data taking in 2009 is shown in Fig. 4.2.

The first detector is called S1, which is located upstream to the target. It is equipped with four photomultiplier tubes (PMTs) which are coupled directly to the scintillator. The second beam counter S2 has only one PMT. Two veto scintillator detectors V0 (round-shaped with a central hole) and V1 (square-shaped also with a central hole)

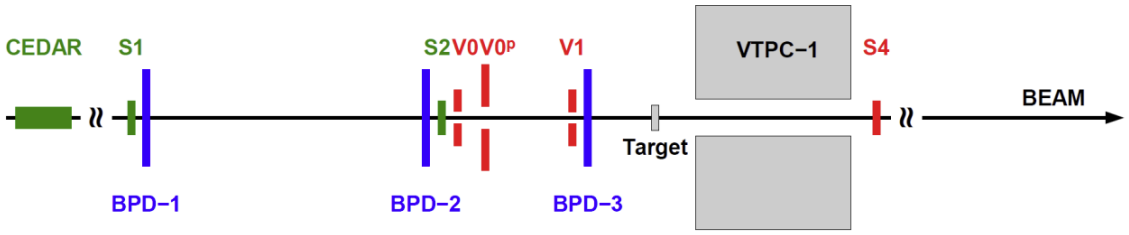

Figure 4.2: Schematic layout (horizontal cut in the beam plane, not to scale) of the beam detectors used in 2009 during the p–p data taking period. Counters pictured in green contribute to trigger logic in coincidence mode and the components marked in red in anti-coincidence.

are positioned downstream of the S2 detector. One additional veto detector $V0^P$ is installed to remove interaction of the beam halo.

The S4 counter is located downstream of the target on the beamline, after VTPC-1. The absence of the beam particle signal in S4 is used to select interactions of beam particles in the target. This veto mainly selects inelastic events and removes elastic scattering events, but it can also result in some losses of inelastic events. The physical dimensions and positions of the beam counters are summarized in Table 4.1. These beam counters are centered at the maximum of the beam profile in the x–y plane (i.e., normal to the beam direction).

The position of the incident particle beam in the x–y plane plane is measured by three Beam Position Detectors (BPDs) which are installed upstream of the target along the beamline. The BPDs used in NA61/SHINE are proportional chambers filled with Ar:CO_2 85:15 gas mixture with an active area of 48×48 mm^2. Two orthogonal sense wire planes, made of 15 μm tungsten wires with a 2 mm pitch are sandwiched between three cathode planes consisting of 25 μm aluminized Mylar. The outer cathode planes feature 2 mm pitch strips connected to the readout electronics. Each BPD measures the position of the trigger-selected beam particle independently in two orthogonal directions using two planes of orthogonal strips.

The beam induces a charge distribution on each strip plane, with an average width of about 5 strips. A BPD cluster is defined as a set of adjacent strips with signal amplitudes above a threshold value. This is done to remove signals from pedestal fluctuations (i.e., fluctuations from the baseline of the signal). The BPD cluster positions are used during the offline reconstruction of the recorded collision events (see Sec. 4.3). The path of the proton beam is used to calculate the position of the beam proton's interaction with the hydrogen in the target material.

Table 4.1: Beam detector parameters: dimensions and positions along the beamline (z coordinates).

Detector	Dimensions [mm]	Hole [mm]	Position [m]
S1	$60 \times 60 \times 5$		-36.42
S2	$\phi = 28 \times 2$		-14.42
S4	$\phi = 20 \times 5$		-2.11
V0	$\phi = 80 \times 10$	$\phi = 10$	-14.16
$V0^p$	$300 \times 300 \times 10$	$\phi = 20$	$\sim$ -14
V1	$100 \times 100 \times 10$	$\phi = 8$	-7.20
BPD-1	$48 \times 48 \times 32.6$		-36.20
BPD-2	$48 \times 48 \times 32.6$		-14.90
BPD-3	$48 \times 48 \times 32.6$		-6.93
Typical target position			-5.81

4.2.2 Time Projection Chamber

Time Projection Chambers (TPC) are the main tracking devices in NA61/SHINE. TPCs are particle detectors that use a combination of electric and magnetic fields together with gas in the detector's active volume to track the three-dimensional motion of a particle. Charged particles passing through the detector interact with the electrons in the gas along their path length. The gas gets ionized, and the incoming particles lose a small fraction of their kinetic energy as they travel through the detector. The energy loss per path length ($\mathrm{d}E/\mathrm{d}x$) of charged particle is approximately described by the Bethe-Bloch formula:

$$-\frac{\mathrm{d}E}{\mathrm{d}x} = 4\pi N_A r_e^2 m_e c^2 \frac{Z}{A}\frac{z^2}{\beta^2}\left[\ln\left(\frac{2mc^2\gamma^2\beta^2}{I}\right) - \frac{\delta}{2}\right], \tag{4.1}$$

where z and m are the charge and mass of the particle, Z and A are the atomic and mass numbers of the active gas material, m_e is the electron mass, r_e is the classical electron radius, N_A is Avogadro constant, I is mean excitation energy which is a characteristic of the active material (ionization potential), δ is the density correction describing how much the extended transverse electric field of incident relativistic particles is screened by the charge density of the gas atom's electrons, and β is the ratio of the particle's speed to the speed of light (c).

Particles identification can be done in TPCs based on the dependence of the particle's $\mathrm{d}E/\mathrm{d}x$ on the charge, mass and velocity (β) of the incident particle. Fig. 4.3 shows the measured energy loss of positrons, pions, kaons, and protons in units of MIPs as a function of momentum, measured for p–p interactions at $p_{\mathrm{beam}} = 80\,\mathrm{GeV}/c$. The parametrized Bethe-Bloch curves for these particles from Eq. 4.1 are also superimposed over the measurements. MIPs are minimum ionizing particles

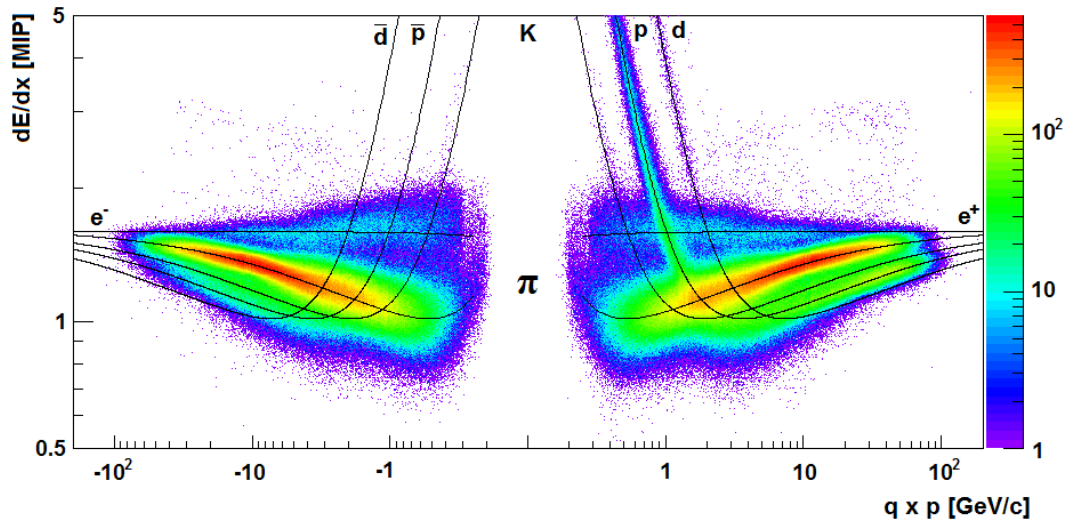

Figure 4.3: Specific energy loss in the TPCs for positive (right) and negative (left) charged particles as a function of particle momentum measured for p–p interactions at $p_{\text{beam}} = 80\,\text{GeV}/c$. Solid curves show the tabulated Bethe-Bloch parametrizations from Eq. 4.1 of the mean $\mathrm{d}E/\mathrm{d}x$ calculated for different particle species. This procedure is discussed in Sec. 4.4.2. Figure from [184].

whose primary energy loss mechanism is via ionization of the material they travel through (e.g. pions and kaons over a large momentum range moving through thin materials). A MIP's $\mathrm{d}E/\mathrm{d}x$ is near the minimum of the Bethe-Bloch curve. Details of the particle identification procedure are discussed later in Sec. 4.4.2.

NA61/SHINE utilizes four large-volume TPCs filled with gas for tracking particles. Two of these (Vertex TPCs: VTPC-1 and VTPC-2) are situated within the magnetic field, while the other two (Main TPCs: MTPC-L and MTPC-R) are positioned symmetrically downstream of the magnets relative to the beamline. Additionally, a smaller TPC (GAP-TPC) is placed between the two VTPCs to measure particles with the smallest production angles.

The ionization electrons created by the charged particles drift toward the chamber's end plates because of the electric field, which is typically parallel to the magnetic field. The uniform vertical electric field is maintained by a surrounding field cage made of aluminized Mylar strips, which are held at the appropriate electric potential by a voltage divider chain. Under the influence of this field, the electrons drift with constant velocity towards the top plates. These plates consist of Multi-Wire Proportional Chambers (MWPCs). The signal amplification of the ionization electrons occurs at the anode wires, and their position, arrival time, and total number are measured using the MWPCs.

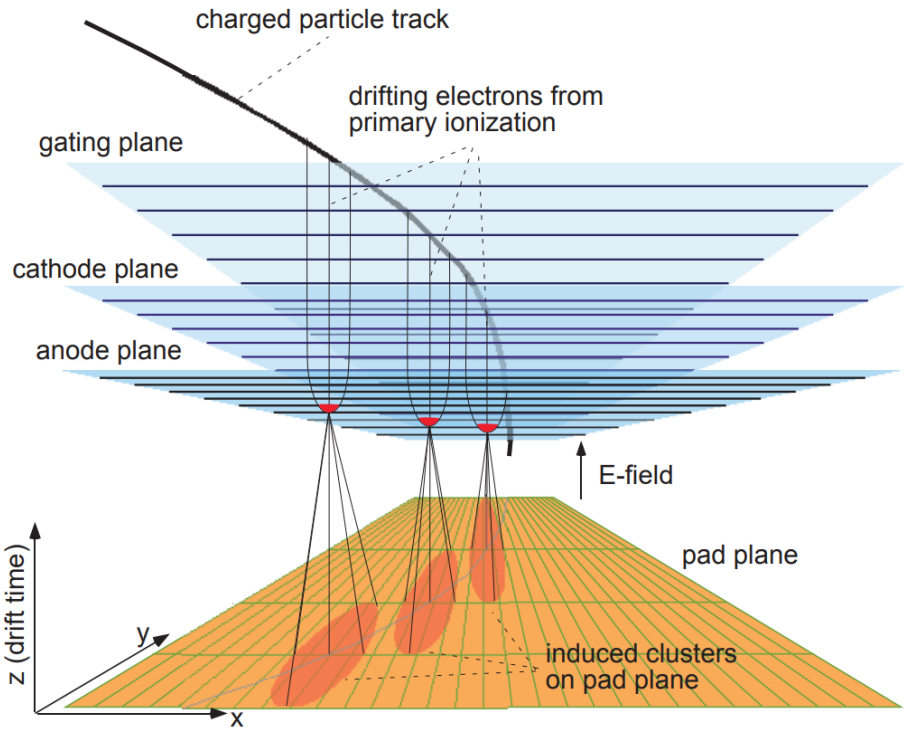

Figure 4.4: TPC Multi-Wire Proportional Chambers (MWPC) readout. Figure adapted from [182, 185].

The readout for TPCs generally consists of gating, cathode, anode, and pad planes, as illustrated in Fig. 4.4. The gating plane prevents positive ions from drifting back into the drift volume and stops electrons from entering the amplification region. During a triggered event, the gate opens, allowing electrons to drift to the cathode plane. The charge signal is amplified between the cathode and anode plane, and is finally collected.

To achieve high spatial resolution, the chamber top plates are subdivided into approximately one square centimeter pad-structured segments, totaling around 180,000 for all TPCs. Such a construction allows the TPCs to perform both energy loss and position measurements. A sequence of three-dimensional coordinates of a particle's interaction point within the TPC gas can be calculated by recording the arrival times of the track signals and the known position of the pads in the pad plane. This information can then be used to reconstruct the particle trajectory. The momentum of the charged particle can be calculated by measured the curvature of the particle trajectory because of the external magnetic field, which were set for a total bending power of 9 Tm for the 158 GeV/c proton beam. The NA61/SHINE TPCs enable the reconstruction of more than 1000 tracks produced in a single interaction event. With up to ~250 clusters and samples of energy loss per particle trajectory,

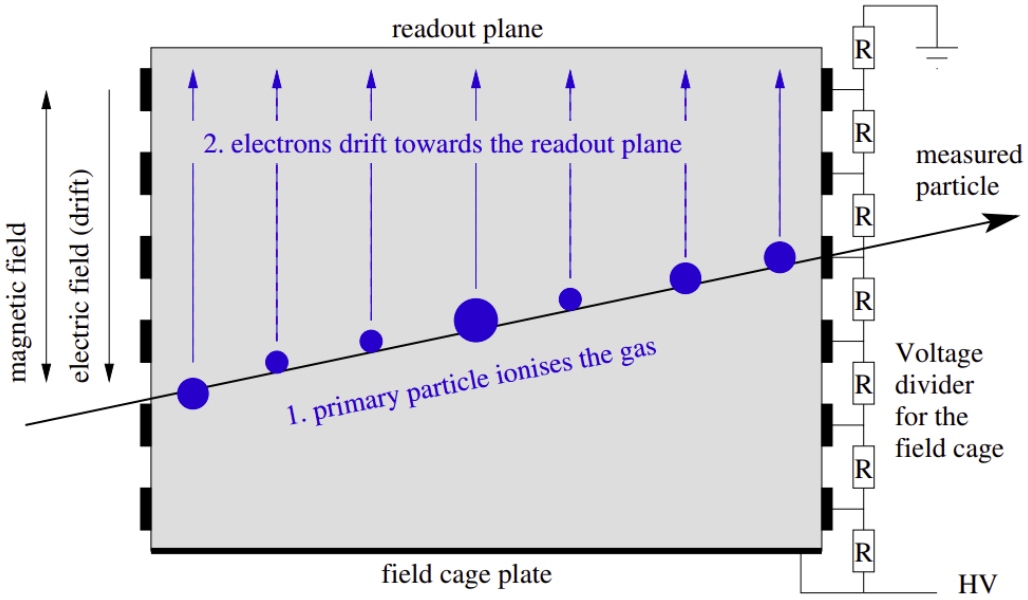

Figure 4.5: Schematic view of the TPC principle. Figure adapted from [182, 186].

they offer high statistics for accurate particlee tracking. A schematic representation of the principle of operation of TPCs is presented in Fig. 4.5.

Both MTPCs have a readout surface of 3.9×3.9,m^2, and a field cage of about 1.1 m in length. They are filled with Ar:CO_2 gas mixture in the proportion 95:5. The track signals are read out by 25 MWPCs, which provide up to 90 measured $\mathrm{d}E/\mathrm{d}x$ clusters or points along the particle's track. The accuracy of the measured mean $\mathrm{d}E/\mathrm{d}x$ is about 4%. The VTPCs boxes have a top surface area of 2.0×2.5 m^2 and a depth of 0.67 m. They are filled with the Ar:CO_2 in 90:10 proportion. Signal readout is done by 6 MWPCs, which can measure up to 72 $\mathrm{d}E/\mathrm{d}x$ clusters along the track length. [184]

The aptly-named GAP-TPC is installed directly on the beamline between VTPC-1 and VTPC-2 to cover the gap between the VTPCs and MTPCs. The additional $\mathrm{d}E/\mathrm{d}x$ clusters from the GAP-TPC are important to extrapolate nearly-straight high-momentum particle tracks to the primary interaction vertex. The material of the GAP-TPC is 0.05% of the proton interaction length, since the beam passes through it. The gas box's drift volume is made of a single layer of 125 mm of Mylar. Its pads have dimensions of $28 \times 4\,\mathrm{mm}^2$, and the readout plane consists of 7 padrows with 96 pads each. Like the VTPCs, it is filled with Ar:CO_2 gas mixture in the proportion 90:10. The parameters of all NA61/SHINE TPCs are summarized in Table 4.2 [184].

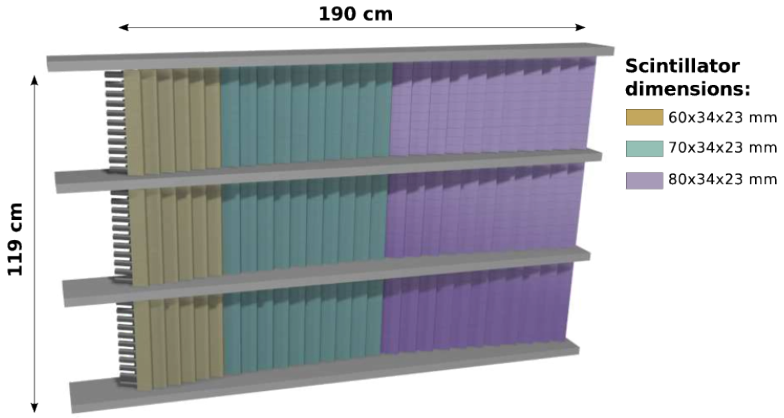

Figure 4.6: Schematic layout of scintillators in the ToF-R detector.

4.2.3 Time of Flight Detector

Additional particle identification power is available if the time-of-flight and the total path length traveled in that time is measured. NA61/SHINE has two ToF walls placed behind the MTPCs. These are called the ToF-L (Left) and ToF-R (Right). Each ToF wall has 891 rectangular-shaped scintillation detectors, totalling 1782 pixels and a total area of 4.4 m^2. A PMT is connected to the shortest side of each scintillator. The scintillators and the photocathode have a thickness of 23 mm, a height of 34 mm, and were produced in three different widths of 60, 70 and 80 mm. The smallest scintillator is placed closest to the beamline, and the largest are placed furthest away (Fig. 4.6). This allows the highest resolution in the detector region with the largest track density.

For the time-of-flight measurement, the start signal for the Time-to-Digital Converters (TDCs) is provided by the S1 beam counter. The analog PMT signals are split, with one part going to a charge-sensitive Analog-to-Digital converter (ADC), and the other goes to a TDC. The TDCs measure time between the start signal and the received

Table 4.2: Parameters of the VTPCs, MTPCs and GTPC in NA61/SHINE.

	VTPC-1	VTPC-2	MTPC-L/R	GTPC
Size ($L \times W \times H$) [cm]	$250 \times 200 \times 98$	$250 \times 200 \times 98$	$390 \times 390 \times 180$	$30 \times 81.5 \times 70$
No. of pads	26886	27648	63360	672
Pad size [mm]	$3.5 \times 28(16)$	3.5×28	$3.6 \times 40, 5.5 \times 40$	4.0×28
Drift length [cm]	66.60	66.60	111.74	58.97
Drift velocity [cm/ms]	1.4	1.4	2.5	1.3
Drift field [V/cm]	195	195	170	173
Drift voltage [kV]	13	13	19	10.2
Gas mixture	Ar:CO_2 (90/10)	Ar:CO_2 (90/10)	Ar:CO_2 (95/5)	Ar:CO_2 (90/10)
No. of sectors	2×3	2×3	5×5	1
No. of padrows	72	72	90	7
No. of pads per padrow	192	192	192, 128	96

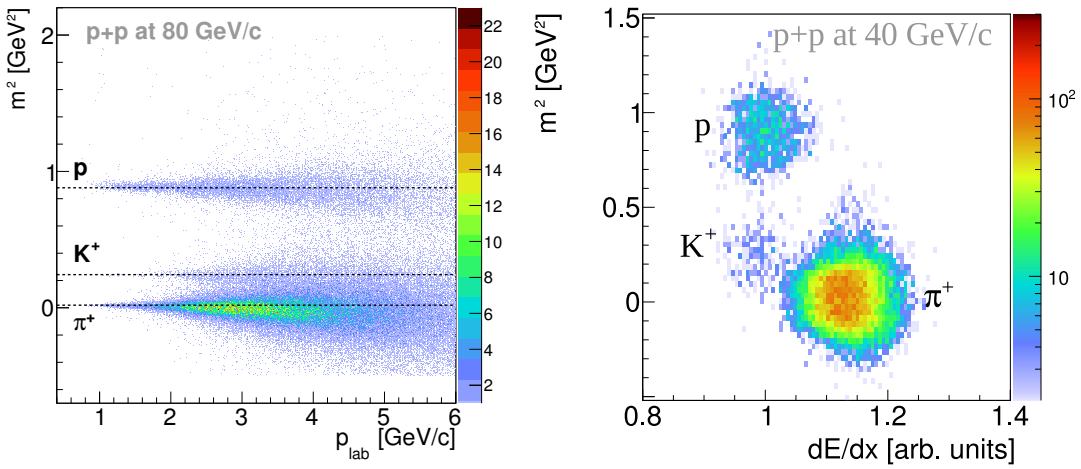

Figure 4.7: Left: Distribution of the calculated m^2 versus reconstructed momentum for p–p interactions at 80 GeV/c in NA61/SHINE. Right: Distribution of the calculated m^2 versus dE/dx for p–p interactions at 40 GeV/c in NA61/SHINE. Different particles like proton, kaons and pions can be identified and are labelled. Figures adapted from [181].

digital signal. If the digital signal is above a threshold, a stop signal is provided. From the measured time-of-flight (Δt), and using the reconstructed particle trajectory to estimate the distance L travelled by the particle as well as its momentum p, the square of the particle's mass (in GeV) can be calculated using:

$$m^2 = (cp)^2 \left(\frac{c^2\,\Delta t^2}{L^2} - 1 \right) \ . \tag{4.2}$$

The time resolution of the ToF-L/R system in NA61/SHINE was estimated by the distribution of the time-of-flight difference between particles identified as pions and prediction from the measured momentum and trajectory after assuming pion mass. This distribution was found to be Gaussian-shaped, with a width or resolution of about 100 ps for ToF-L, and 80 ps for ToF-R. This resolution included contributions from the intrinsic ToF detector resolution, the start detector resolution, and the uncertainties in particle tracking and extrapolation. The resolutions of the two ToF walls are not the same because they were built separately with non-identical components like PMTs and readout electronics.

An example distribution of the calculated m^2 versus reconstructed momentum for p–p interactions at 80 GeV/c in NA61/SHINE is shown in Fig. 4.7 (left). Fig. 4.7 (right) shows an example distribution of m^2 versus dE/dx for p–p interactions at 40 GeV/c in NA61/SHINE [181]. Expected hadrons regions are labeled. Negative values in the distribution are due to the finite measurement resolution. This method is used to supplement the TPC measurements and can provide particle identification in the crossover region of the Bethe Bloch curves. It is also crucial for deuteron identification,

because of the significant difference in deuteron mass from other hadrons with unit charge, like protons, pions, kaons (see Sec. 4.5).

4.2.4 Beams and Target

The incident proton beam at momenta of 158 GeV/c are secondary beams produced from the 400 GeV/c protons extracted from CERN-SPS. The beam momentum and intensity is adjusted using the magnets and collimators of the H2 beamline (see Fig. 4.8). The beam magnet currents can be set with a precision of approximately 0.5%. The beam momentum of the proton beam at 31 GeV/c was validated by directly measuring it using the dE/dx identification method. This was done by bending the beam into the TPCs with the maximum magnetic field setting [187], and measuring the energy loss of the beam protons in the TPCs.

Beam protons were identified by using two Cherenkov counters, a gas ring imaging CEDAR [188] and a threshold counter (THC). The CEDAR is based on a coincidence of six out of the eight PMTs which are placed radially along the Cerenkov ring. The THC is used in anti-coincidence within the trigger logic. Individual beam particles were identified and precisely measured by a set of scintillation and Cherenkov counters, as well as the three BPDs placed upstream of the target. A selection procedure based on the Cherenkov counters enabled to identify beam protons with a purity of about 99% [189].

For recording p–p interactions, a Liquid Hydrogen Target (LHT) of length 20.29 cm (corresponding to 2.8% interaction length of the beam proton) and diameter of 3 cm was used. The LHT was placed 88.4 cm upstream of VTPC-1. It was filled with para-hydrogen obtained in a closed-loop liquefaction system from the LHT facility, and it was operated at 75 mbar overpressure with respect to the atmosphere (965 mbar). At atmospheric pressure, the density ρ_{LH} of liquid hydrogen is equal to 0.0707 g/cm^3. Data were taken with liquid hydrogen inside the target (target-inserted), and ~10% data were also taken with an empty target (target-removed) to estimate background interactions.

4.3 Calibration and Reconstruction

Before the recorded collision events can be studied for analysis, they need to be calibrated and reconstructed. A data-based calibration procedure was used to optimize detector parameters and their time dependence. Adjustments were made in consecutive steps for each of the following effects: detector geometry, TPC drift velocities, inhomogeneities in the magnetic field in the VTPC corners, magnetic field settings, specific energy loss (dE/dx) measurements, and finally the time-of-flight measurements [190]. For each step, a small data sample was reconstructed to optimize

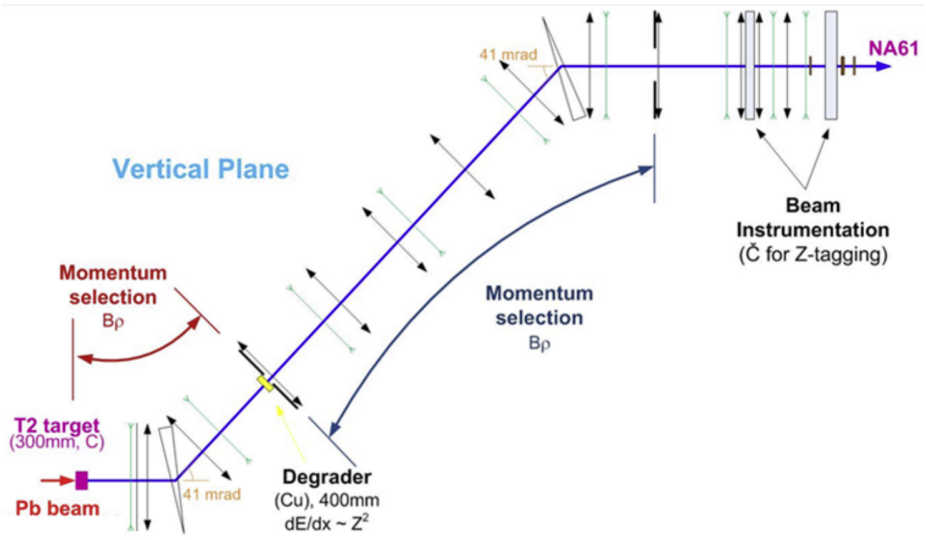

Figure 4.8: Schematic of the H2 beam line for fragmented ion beam. The dimensions are not to scale, as the beamline is more than 600 m long.

the calibration constants and their time-dependent corrections. This was followed by verification procedures and reconstruction of the full data set.

NA61/SHINE data is reconstructed in the following steps. First, the reconstruction algorithm uses the TPC raw cluster information to calculate total charge, and to find track segments in each TPC separately. The tracks segments are then matched and combined to form global tracks. Next, the global tracks are fitted while taking into account the magnetic field, and track parameters are determined at the first TPC cluster.

The algorithm searches for a cluster in each BPD plane. Then, an average of the strip positions weighted with the signal amplitudes on the BPD strips is calculated (using the centroid method) to estimate the position of the beam particle. In each BPD, a three-dimensional position is calculated by using the two transverse coordinates measured by the two strip planes and from the position of the BPD along the beamline. In order to reconstruct a beam particle track, an independent least-squares fits of the straight lines is performed on the positions measured by the three BPDs in the x–z and y–z planes.

The global tracks and the beam trajectory from the BPDs are together used to find the main p–p interaction vertex. The global tracks are refitted after including this interaction vertex, to finalize the particle trajectory and estimate its momentum at the interaction vertex. In the last step, the TPC tracks are matched with the T0F pixel hits [189]. An example reconstructed p–p collision event at $p_{\text{beam}} = 158\,\text{GeV}/c$ measured in NA61/SHINE is shown in Fig. 4.9.

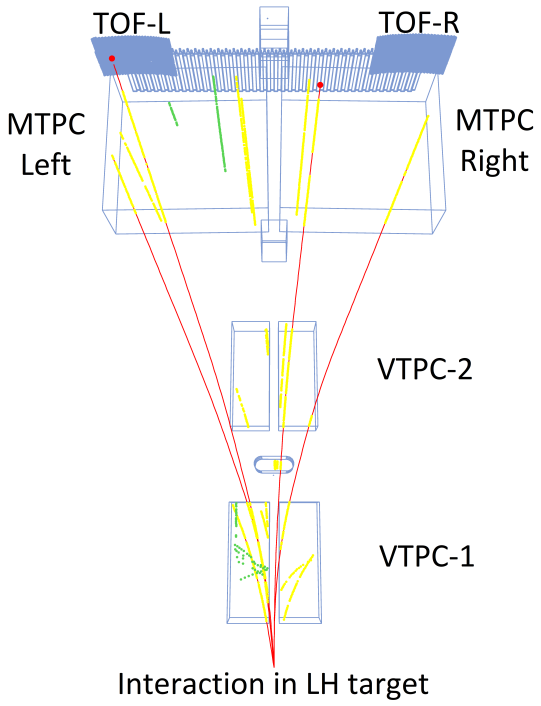

Figure 4.9: An example reconstructed p–p collision event at $p_{\text{beam}} = 158\,\text{GeV}/c$. The main vertex is where the beam proton interacted within the liquid hydrogen target (LHT). Red curves are reconstructed tracks corresponding to particles produced in the main p–p interaction point within the LHT. Yellow points show measured clusters in TPCs matched to primary tracks, and green points are measured clusters without any matching.

4.3.1 Monte-Carlo Simulations

Particle detectors are not perfect, and particles can go undetected for various reasons. One reason is limited geometrical acceptance, which means that detectable particles originating in certain kinematic regions do not pass through the detector. Another reason is suboptimal detector response, relating to the detector's capability to accurately identify and measure particles as they move through it. To account for these biases in the analysis of reconstructed data and correct the detected particle counts, it is vital to simulate an accurate detector response. These corrections play a crucial role in determining the true number of particles produced in the recorded p–p collision events. NA61/SHINE selected the `EPOS-1.99` [191] model for Monte-Carlo (MC) simulations for having the best available agreement with data for particle production from weak decays (feed-down corrections). Only inelastic interactions of the beam protons within the liquid-hydrogen target were simulated and reconstructed. Therefore, contribution of elastic scattering events is removed by the event selection cuts described in Sec. 4.4.1. The procedure for the corrections of all other biases is described in Sec. 4.4.4.

Table 4.3: Summary of the recorded high-statistics p–p interactions at $p_{\text{beam}} = 158\,\text{GeV}/c$ in NA61/SHINE.

Year	p–p interactions recorded	Total selected events
2009	3.8 million	1.6 million
2010	43.1 million	25.6 million
2011	13.7 million	8.1 million
Total	60.6 million	35.3 million

The detector response was simulated in the following steps. First, inelastic hadronic interaction events were generated. The produced particles were then propagated through the detector material using the `Geant` 3.21 software package [192], while taking into account the magnetic field as well as physics processes like particle decays. The detector response was simulated using dedicated NA61/SHINE packages which add distortions and inefficiencies consistent with various detector effects. The simulated and experimental data were stored in exactly the same format. The simulated events were then reconstructed using the same data reconstruction chain described earlier. The reconstructed tracks from the simulation were matched with the original simulated tracks by matching their cluster positions.

4.4 The dE/dx Analysis

In 2009, 2010, and 2011, NA61/SHINE recorded a total of more than 62 million p–p collisions at $158\,\text{GeV}/c$, containing more than 750 million produced particle tracks. This combined set is collectively called the p–p high-statistics data. After the application of event and track quality cuts described in Sec. 4.4.1, about 31 million collision events containing about 60 million particle tracks were selected for further analysis. The recorded event statistics are summarized in Table 4.3.

To ensure that the recorded events have a main interaction vertex within the LH target, a minimum bias trigger is used. This is done by requiring the detection of an incident beam proton upstream of the LH target (measured via signal from the S1 counter), and its disappearance downstream of the target (when there is no signal from the S4 counter). The high-statistics data were recorded with the so-called T1 beam trigger and the T2 interaction trigger, which consisted of the following:

T1: $S1 \times S2 \times \overline{V0} \times \overline{V1} \times \overline{CEDAR}$ (proton beam trigger),
T2: $S1 \times S2 \times \overline{V0} \times \overline{V1} \times \overline{CEDAR} \times \overline{S4}$ (proton interaction trigger),

where for example, $S1$ means the requirement of a signal from the S1 counter, and $\overline{S4}$ means the absence of any signal from the S4 counter. See Sec. 4.2.1 for details of the trigger setup. The overall analysis procedure consists of the following steps:

1. Event and track selection.
2. Calculation of raw (i.e., uncorrected for biases) particle count distributions of identified charged hadrons.
3. Applying data-derived and simulation-based corrections to the raw counts.
4. Calculation of the corrected particle spectra.
5. Estimation of statistical and systematic uncertainties.

The raw particle count distributions were corrected for the following effects:

(a) Contribution of particles produced from interaction outside the LHT (off-target interactions).
(b) Geometrical acceptance of the detector and detector efficiencies.
(c) Contribution of particles which are produced in weak decays (feed-down effect).

In this analysis, the final particle counts were measured in two-dimensional bins of rapidity (y) and transverse momentum (p_T). The particle rapidity was calculated in the collision center-of-mass frame. The bin size was chosen taking into account the statistical uncertainties and the resolution of the momentum reconstruction, to reduce the effect of bin-to-bin migration to less than 1% [189]. Corrections (Sec. 4.4.4), and statistical and systematic uncertainties (Sec. 4.4.5) were estimated for each bin. The final product of this analysis were charged hadrons spectra produced by strong interaction processes and in electromagnetic decays of produced hadrons in inelastic p–p interactions at $p_{\text{beam}} = 158\,\text{GeV}/c$.

4.4.1 Event and Track Selection

The following criteria were applied to select inelastic p–p interaction events from the reconstructed data:

Off-time beam particles The first step in the offline data analysis was to reject any events which had another off-time beam particle within the acquisition window of the trigger particle. During data collection, the S1 counter PMT was connected to a Wave Form Analyzer (WFA), which registered signals which were close in time. The proton beam was found to have a small probability of having a second beam particle within a $\pm 2\,\mu$s window about the beam particle. Events with such off-time beam particles were rejected. Fig. 4.10 shows the time distribution measured between the two beam particles in such events, before the WFA cut.

Trajectory of beam proton Next, the incident beam proton trajectory was verified. It was required to have a measured signal in both planes of BPD3 (which is the closest BPD to the target), and at least in three out of the total four planes of the other two BPDs (BPD-1 and BPD-2).

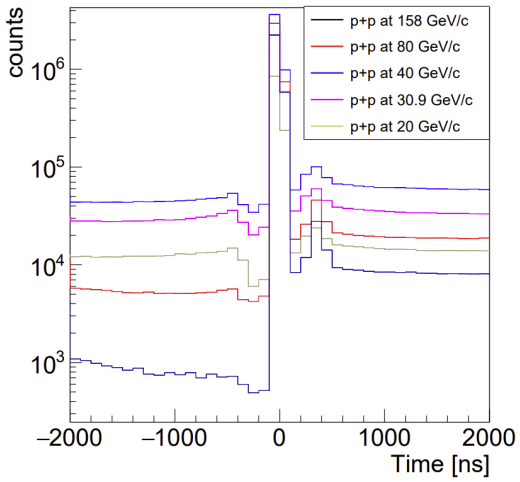

Figure 4.10: Time between the trigger particle and the other beam particles measured by Wave Form Analyzer (WFA) before the cut. Figure adapted from [182].

Reconstructed main interaction The event must contain at least one track reconstructed in the TPCs and originating from the main p–p interaction vertex.

Main vertex position The position of the fitted main interaction vertex was checked. Only events which had the z-coordinate of the main vertex within a range of $\pm 20\,\text{cm}$ from the center of the LHT were allowed. The distribution of the z-coordinate of the main vertices is shown in Fig. 4.11, and discussed further in Fig. 4.15.

Elastic interactions Finally, events which contained only a single reconstructed positive-charged track with momentum close to the beam proton's momentum were assumed to be proton elastic scattering interactions, and were rejected.

For selecting simulated events which were reconstructed in the MC analysis, all cuts listed above were applied. The WFA and BPD cuts are not applied as they were not simulated in the MC. The T2 interaction trigger was also not simulated, but this cut was applied in the MC using an effective T2 trigger cut, which was implemented by ensuring that there was no energy deposition in the simulated S4 counter in the MC.

To select only primary charged hadrons, and to reduce the contamination from off-time interactions, weak decays and secondary interactions, the following criteria were used to select the reconstructed particle tracks:

1. Tracks must have originated from the main interaction vertex.
2. The momentum fit of the track at the main interaction vertex should have converged.

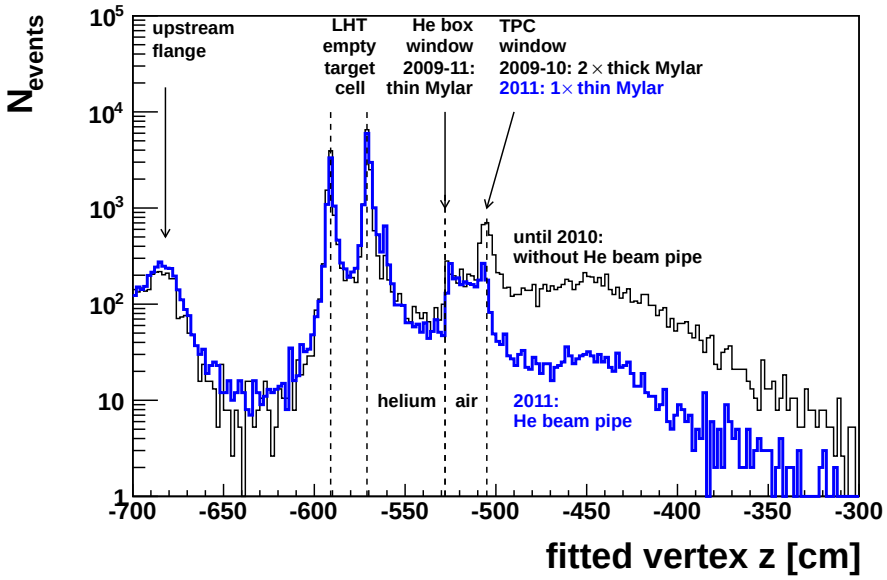

Figure 4.11: Main interaction vertex distribution along the beam axis for p–p interactions at 158 GeV/c, before the He beam pipe installation (2009 and 2010 data) and after the He beam pipes were installed and filled with helium gas (2011 data). Different detector components can be identified and have been labelled, including the fiducial volume of the LHT holders, centered close to -580 cm. Figure adapted from [184].

3. The fitted x-component of the rigidity ($p_{Lab,x}/q$) must be positive. This ensured that the angle between the initial track trajectory and the TPC pad direction was small. This reduced uncertainties in the reconstructed cluster positions, energy depositions, and the fitted track parameters. Tracks which pass this cut are called Right Side Tracks (RSTs), and which don't are called Wrong Side Tracks (WSTs) [193].
4. To ensure better measurements of particle trajectories, tracks must have at least 30 reconstructed clusters. Also, at least 15 points must be reconstructed in either VTPC-1 and VTPC-2, or the GAP-TPC should have at least 4 reconstructed points. Similar criteria is set for dE/dx clusters.
5. Finally, the impact parameter i.e., the distance between the main interaction vertex and the fitted track's extrapolation to the x–y plane at the main interaction vertex's z-coordinate, must be smaller than 4 cm in the horizontal (bending) plane and 2 cm in the vertical (drift) plane.

The dE/dx-only analysis does not use the ToF information. The final selected event and track statistics after successive application of these quality cuts is shown in Fig. 4.12.

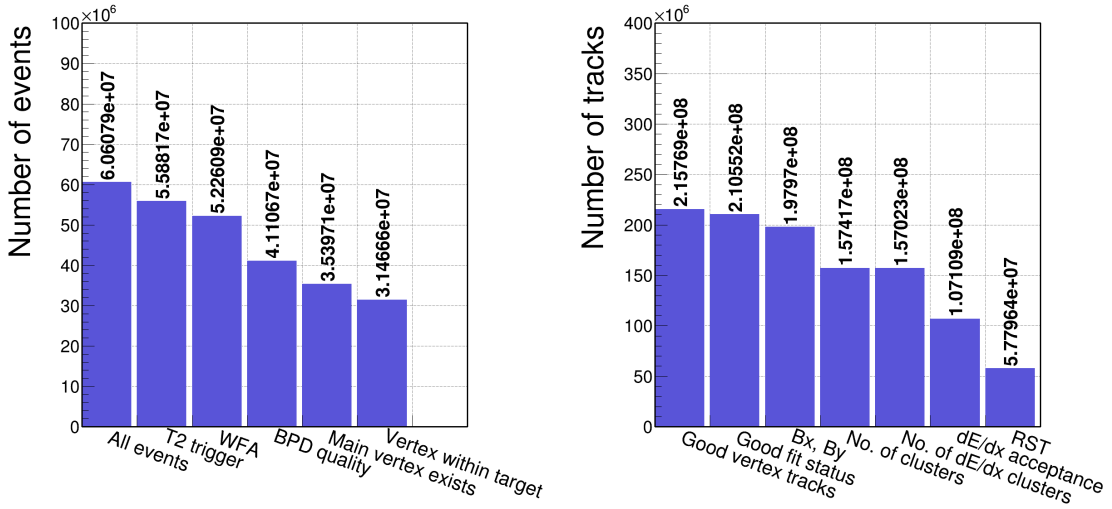

Figure 4.12: Left: Selection statistics of event selection cuts. Right: Selection statistics of track selection cuts.

4.4.2 Particle Identification Based on Specific Energy Loss Measurement ($\mathrm{d}E/\mathrm{d}x$)

As discussed before in Sec. 4.2.2, the main charged-particle identification technique in NA61/SHINE is based on the measurement of $\mathrm{d}E/\mathrm{d}x$ along particle trajectories in the TPCs as a function of momentum. This method is particularly important in the region of the relativistic rise of the ionization, where particle momenta is larger than $\approx 4\,\mathrm{GeV}/c$. At lower momenta, the $\mathrm{d}E/\mathrm{d}x$ measurements for different particle species overlap, and particle identification is not possible. The phase space acceptance map for this analysis is shown in Fig. 4.13.

Simultaneous measurements of $\mathrm{d}E/\mathrm{d}x$ and p_{lab} can be used to separate particles by their mass. This procedure was developed for the analysis of the low-statistics p–p data in Ref. [181]. The truncated mean $\mathrm{d}E/\mathrm{d}x$ for each TPC track was calculated as the average of the smallest 50% of the energy loss measurements along the track. This was done to remove the Landau distribution tails from the $\mathrm{d}E/\mathrm{d}x$ distributions. Fig. 4.3 shows the distribution of positive and negative charged tracks in the $\mathrm{d}E/\mathrm{d}x$–momentum plane. The expected dependence of this distribution for different particles, based on the Bethe-Bloch function (Eq. 4.1) is also shown.

The yields of positive-charged particles (π^+, p, K^+, and e^+) and negative-charged particles (π^-, $\bar{p}$, K^-, and e^-) are calculated separately by fitting the $\mathrm{d}E/\mathrm{d}x$ distributions in two-dimensional bins of p_{lab} (particle momentum in the laboratory frame) and p_T (transverse momentum). To cover the full detector acceptance while ensuring similar particle statistics in each bin, the phase space was

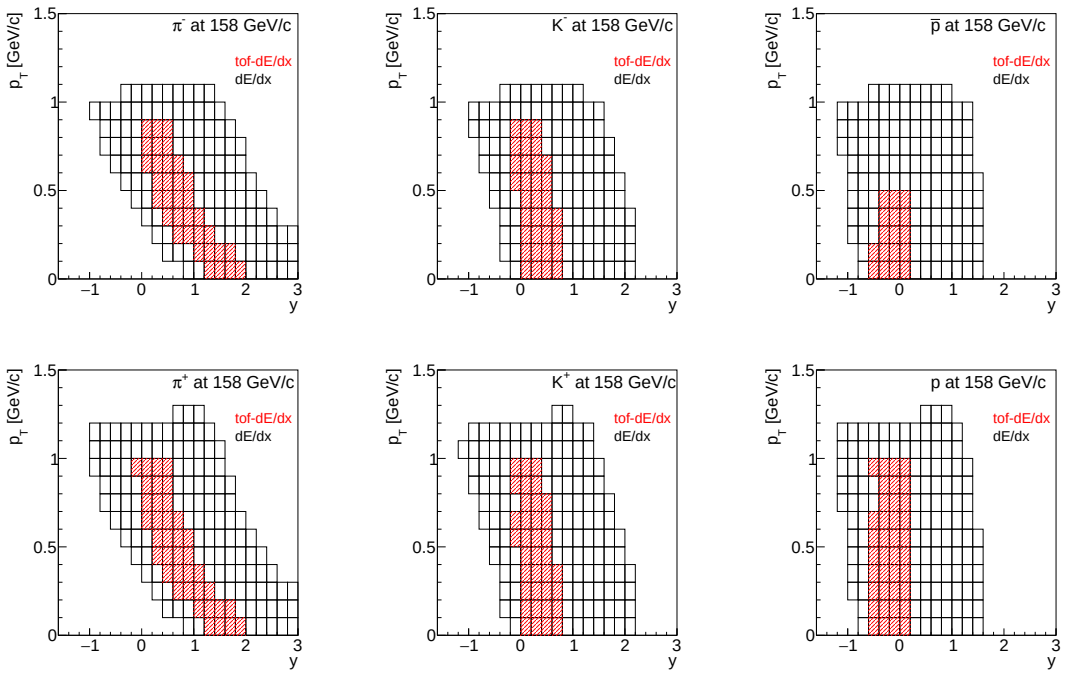

Figure 4.13: Acceptance of the tof–dE/dx (see Sec. 4.5.2) and dE/dx-only analysis (Sec. 4.4.2) for identification of pions, kaons and protons in p–p interactions at $p_{\text{beam}} = 158\,\text{GeV}/c$ in the low-statistics data from 2009. Figures adapted from [181].

divided into 400 two-dimensional bins, with 20 logarithmic-spaced bins in p_{lab} between 1–100 GeV/c , and 20 equal-sized p_T bins in the range of 0–2 GeV/c .

The total fit in each bin is a sum of four functions [194, 195], each corresponding to the expected dE/dx distribution of one of the particle types. The (anti)deuterons contribution is negligible in the dE/dx analysis and was set to zero. The model dE/dx distribution for tracks of a given particle type i is parametrized as a Gaussian distribution with width parameter $\sigma_{i,l}$. The widths depend on the particle type i and the number of points l measured along the track in the TPCs. To simplify the fit formula notation, the peak positions of the model dE/dx distributions are denoted by x_i for particle type i. The contribution of a reconstructed particle track to the fit function is given by:

$$\rho(x) = \sum_i \rho_i(x) = \sum_{i=\pi,p,K,e} A_i \frac{1}{\sum_l n_l} \sum_l \frac{n_l}{\sqrt{2\pi}\sigma_{i,l}} exp\left[-\frac{1}{2}\left(\frac{x - x_i}{\sigma_{i,l}}\right)^2\right] , \qquad (4.3)$$

where x is the dE/dx of the particle, n_l is the number of tracks with l points in the sample, and A_i is the amplitude of the contribution of particles of type i. Pions are the most abundant particles in the majority of kinematic bins, making their peak

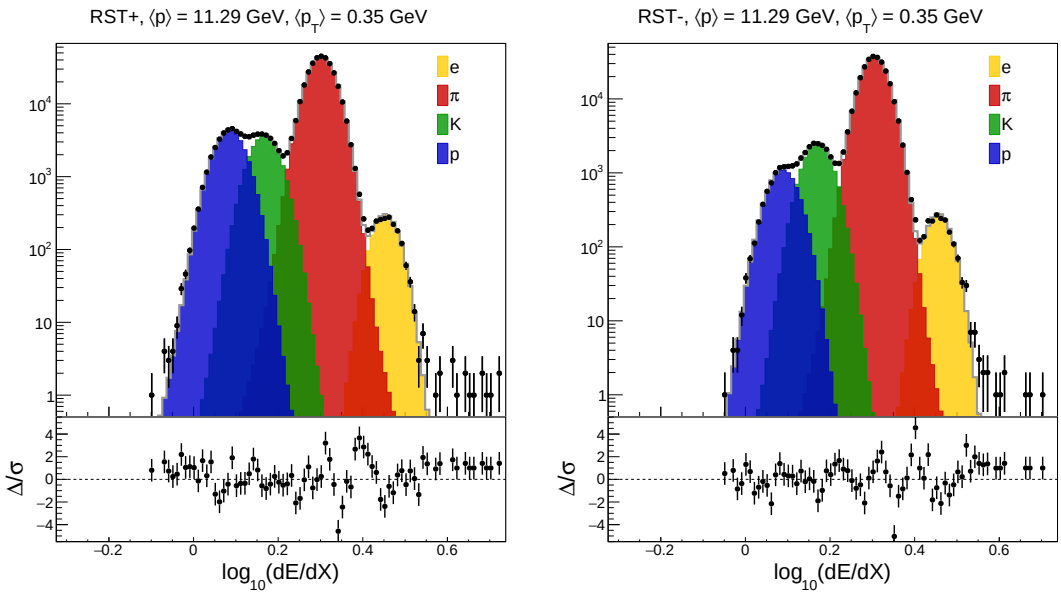

Figure 4.14: Typical $\mathrm{d}E/\mathrm{d}x$ distributions for positive (left) and negative (right) charged tracks in a single phase space bin in the high-statistics p–p data at 158 GeV/c are shown in the top panel. The fit by a sum of contributions from different particles is shown by the shaded histograms. The corresponding residuals (the difference between the data and fit divided by the uncertainty of the data) is shown in the bottom panel.

positions relatively easier to fit. The second sum is the weighted average of the line-shapes from the different numbers of measured points (which are proportional to the track's length) in the sample. The quantity $\sigma_{i,l}$ is defined as:

$$\sigma_{i,l} = \sigma_0 \left(\frac{x_i}{x_\pi} \right)^{0.625} / \sqrt{n_l}, \tag{4.4}$$

where the width parameter σ_0 was assumed to be common for all particle types and bins. A statistical $1/\sqrt{l}$ dependence on the number of points of a track was assumed. The Gaussian distributions were tested for possible asymmetry due to Landau distribution tails persisting after the truncated mean $\mathrm{d}E/\mathrm{d}x$ calculation [196]. However, no significant asymmetry was found.

The total fit function has 9 parameters (4 amplitudes, 4 peak positions and the width parameter σ_0). The following conditions were used to constrain the fit parameters:

1. The relative peak positions of electrons, kaons and protons to pions (i.e., x_i/x_π) were assumed to be p_T-independent.
2. The electron amplitude was set to zero for momentum bins above 23.4 GeV/c (i.e., starting from the 13^{th} bin), as the electron contribution vanishes at high p_{lab} .

3. Wherever possible, the relative peaks positions of the positive-charged kaons was set equal to that of negative-charged kaons in the same $(p_{\rm lab}, p_{\rm T})$ bin. This helped to overcome the large overlap between K^+ and proton $\mathrm{d}E/\mathrm{d}x$ distributions in some bins.

These constraints reduce the number of independently-fitted parameters in each bin from 9 to 6, i.e., the amplitudes of the four particle types, the pion peak positions and the width parameter σ_0. Fig. 4.14 shows the measured $\mathrm{d}E/\mathrm{d}x$ distribution and the resultant fits, using the procedure described above, in an example kinematic bin for both positively and negatively charged particles.

To ensure a high-quality fit, only bins containing more than 300 tracks were selected for fitting. The fitting process continues until either the $(p_{\rm lab}, p_{\rm T})$ bin has low statistics, or the fit cannot converge. Bethe-Bloch curves for various particle types intersect at low total momentum values, resulting in inadequate separation for particle identification. Consequently, bins up to the 5^{th} ($p_{\rm lab}$ ¡ 3.98 GeV $/c$) are excluded from the analysis. Separation between kaon and proton peaks is particularly challenging. The quality of these fits is a major source of systematic uncertainty in the final measurements, and its evaluation is discussed in Sec. 4.4.5.2.

4.4.3 Probability Method

The $\mathrm{d}E/\mathrm{d}x$ fits from Eq. 4.3 were used to calculate the probabilities P_i that a TPC track is of a given particle-type $i = \pi, K, p, e$. These probabilities can be calculated as:

$$P_i(\mathrm{d}E/\mathrm{d}x, p_{\rm lab}, p_{\rm T}) = \frac{\rho_i(\mathrm{d}E/\mathrm{d}x, p_{\rm lab}, p_{\rm T})}{\sum\limits_{i=\pi,K,p,e} \rho_i(\mathrm{d}E/\mathrm{d}x, p_{\rm lab}, p_{\rm T})}, \tag{4.5}$$

where ρ_i is the value of the fit function for particle-type i in a given $(p_{\rm lab}, p_{\rm T})$ bin, evaluated at the $\mathrm{d}E/\mathrm{d}x$ of the track. The denominator is the value of the total fit in that bin, evaluated at the $\mathrm{d}E/\mathrm{d}x$ of the track.

Using the probability technique, each track in data was assigned four values or probabilities for being pion-like, kaon-like, proton-like and electron-like. In the case of perfect particle identification with no overlap between different particles, the calculated probabilities would either 0 or 1. However, because of overlapping $\mathrm{d}E/\mathrm{d}x$ distributions, the calculated particle probabilities range between the two extremes. The probability method also allows to transform fit results performed in ($p_{\rm lab}$, p_T) bins to results in $(y, p_{\rm T})$ bins. For a track characterized with ($p_{\rm lab}$, p_T, $\mathrm{d}E/\mathrm{d}x$, P_i), its rapidity (y) can be calculated as:

$$y = \frac{1}{2} \ln \frac{E + p_z c}{E - p_z c}, \tag{4.6}$$

where E is the particle's total energy ($E = \sqrt{p^2 + m^2}$), p_z is the z-component of the particle's momentum (i.e., along the beam axis), and c is the speed of light. The transformation from the laboratory frame to the center-of-mass frame can be done using:

$$y_{\text{cm}} = y_{\text{lab}} - \frac{1}{2}\, y_{\text{beam}} \tag{4.7}$$

After this, the track can be added to the (y, p_{T}) histogram of particle i with weight P_i. The total number of raw (i.e., uncorrected for detector effects) identified particles n^{raw} of particle-type i in a given kinematic bin of the (y, p_{T}) histogram is given by [197]:

$$n^{raw}_{i=\pi,K,P} = \sum_{j=1}^{N_{trk}} P_i, \tag{4.8}$$

where P_i is the probability or weight of particle type i given by Eq. 4.5, and j is the index to sum the weights over all N_{trk} in the given kinematic bin.

4.4.4 Corrections

The (y, p_{T}) raw particle yields (i.e., count distributions) measured in the $\mathrm{d}E/\mathrm{d}x$ analysis need to be corrected for three main biases: the off-target interaction background, the detector's geometric acceptance and efficiencies, and particle produced in weak decays.

4.4.4.1 Correction for Off-Target Interactions

About 10% of the recorded data were collected without the liquid hydrogen in the target. This is called the target-removed or target-out data. This was done to estimate the background from off-target interactions. Before the particle identification procedure described in Sec. 4.4.2, a normalized target-removed particle counts were subtracted from the target-inserted data. This correction was applied for each (p_{lab}, p_T) bin.

The normalization or scaling factor was estimated based on the z-coordinate distribution of the fitted main vertex positions. The factor was calculated as the ratio of the numbers of events with fitted main vertex outside the target, in the range from -400 to -200 cm, for target-inserted and removed data. It was found to be 2.91. The scaled-up distribution for target-removed events is shown in Fig. 4.15. This subtraction procedure removed the interactions of the beam protons with the target aquarium and the detector materials. Together with the cut on the z-coordinate of the fitted main vertex, it ensured that the subtracted particle count distributions shown in Fig. 4.16 contained only particles produced from interactions within the LHT.

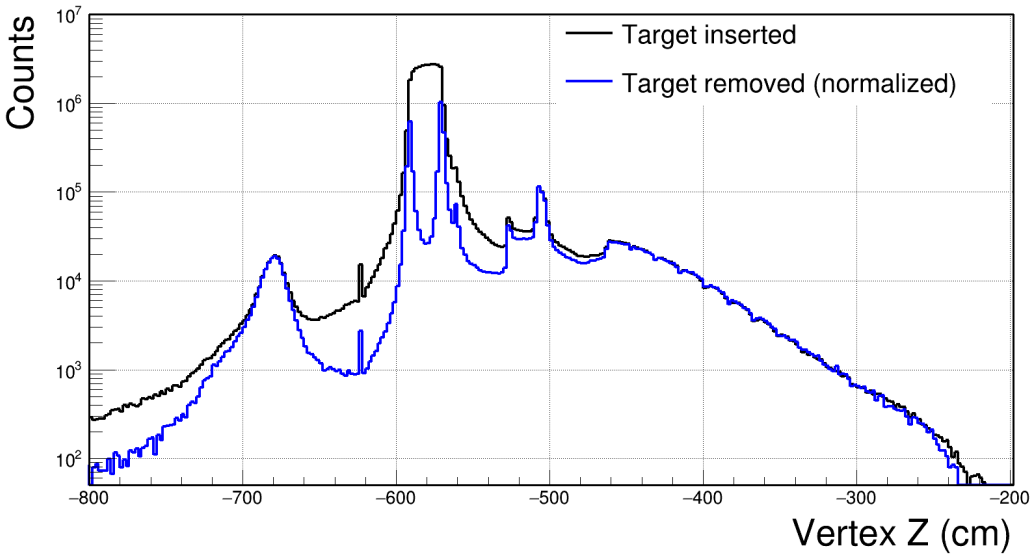

Figure 4.15: The z-coordinate of the fitted vertex positions measured in p–p interactions at $p_{\text{beam}} = 158\,\text{GeV}/c$ is shown in black for target-inserted events. The fiducial volume of the Liquid Hydrogen target can be seen in the range from -600 cm to -560 cm in the NA61/SHINE coordinate system. The normalized distribution for target-removed events is also shown in blue. Sec. 4.4.4.1 shows the details of this normalization procedure.

4.4.4.2 Correction for Detector Effects and Weak Decays

In the detector simulation described in Sec. 4.3.1, more than 200 million p–p interactions were simulated at $p_{\text{beam}} = 158\,\text{GeV}/c$ using the `EPOS-1.99` hadronic generator model. These simulations were used to calculate corrections for detector effects. A significant fraction of the selected tracks may consist of hadrons that were produced in weak decays of particles produced in the primary p–p interaction. The main source of weak decays are the lambda hyperons, and their feed down was found to be well modelled in `EPOS-1.99` [181]. Therefore, the simulation was used to correct this feed-down effect as well.

In the $\mathrm{d}E/\mathrm{d}x$ analysis, the MC correction factors $C_i(y, p_{\text{T}})$ were calculated for each of the six particle types i (i = p, $\overline{\text{p}}$, $\pi^{\pm}$ and $K^{\pm}$) as following:

$$C_i(y, p_{\text{T}}) = \frac{n_{i_{gen}}^{MC}(y, p_{\text{T}})}{n_{i_{sel}}^{MC}(y, p_{\text{T}})}, \tag{4.9}$$

where $n_{i_{gen}}^{MC}(y, p_{\text{T}})$ is the multiplicity of particle type i generated by the `EPOS-1.99` model in a given (y, p_{T}) bin, and $n_{i_{sel}}^{MC}(y, p_{\text{T}})$ is the multiplicity of particle type i after reconstructed and applying the event and track selection criteria described in the previous sections. Particle multiplicities for particle type i were calculated in the

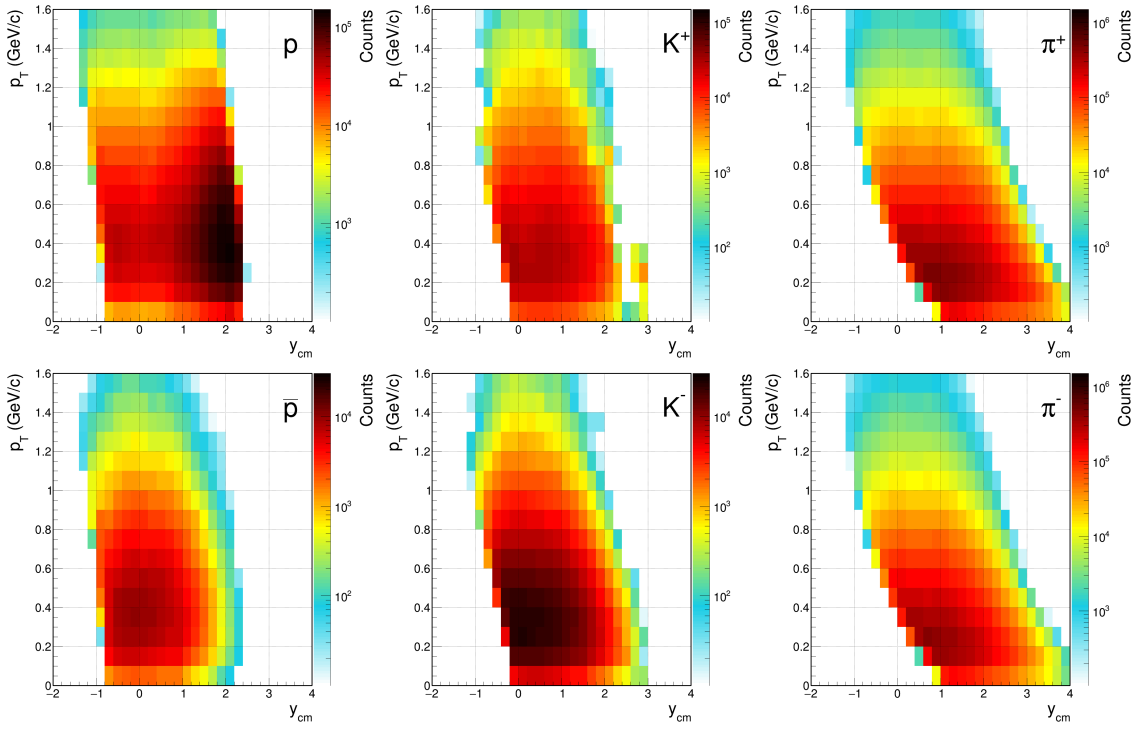

Figure 4.16: Background-subtracted particle count distributions in bins of transverse momentum (p_T) and center-of-mass rapidity (y_{cm}), for positive (top) and negative (bottom) charged protons, kaons, and pions produced in inelastic p–p interactions at $p_{\text{beam}} = 158\,\text{GeV}/c$.

MC analysis by dividing the number of generated (or selected) particles of type i in each bin by the total number of generated (or selected) p–p events.

The correction factors were calculated in the same $C_i(y, p_{\text{T}})$ bins as the particle count distributions. Fig. 4.17 shows the (y, p_{T}) distribution of correction factors for all six particle types. Bins with correction factors smaller than 0.5 and larger than 1.5 were removed from the final results, as either their acceptance was too low, or the contamination from particles coming from weak decays was high. The uncertainties in the correction factors were estimated using binomial statistics, but due to the very large number of particles simulated in each kinematic bin, this error was found to be less than one percent.

4.4.5 Corrected Spectra and Uncertainties

The final hadron multiplicities from the inelastic p–p interactions measured by the $\mathrm{d}E/\mathrm{d}x$ technique can be defined as the sum of track probabilities corrected for different biases, divided by the number of background-subtracted collision events.

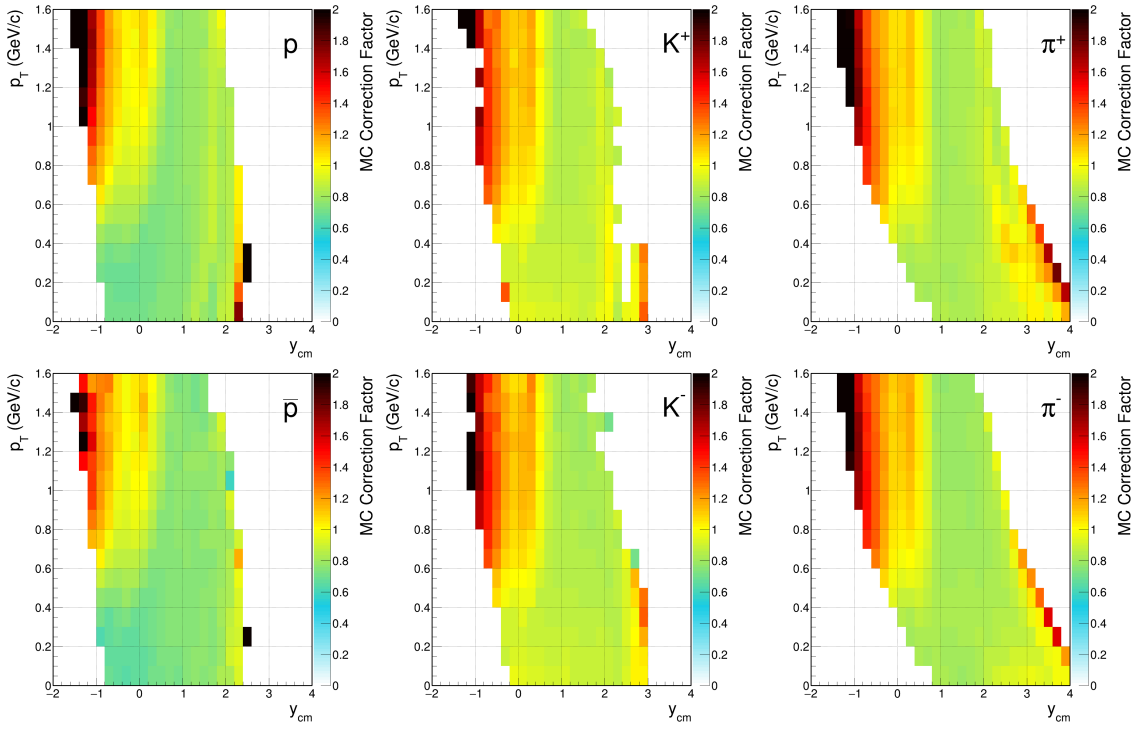

Figure 4.17: Correction factor distributions for the $\mathrm{d}E/\mathrm{d}x$ analysis, in bins of transverse momentum (p_T) and center-of-mass rapidity (y_{cm}), for positive (top) and negative (bottom) charged protons, kaons, and pions produced in inelastic p–p interactions at $p_{\mathrm{beam}} = 158\,\mathrm{GeV}/c$.

For particle type i (where $i = \mathrm{p}$, $\overline{\mathrm{p}}$, $\pi^{\pm}$ and $K^{\pm}$), the multiplicity is defined as:

$$\frac{n_i(y, p_{\mathrm{T}})}{N} = C_i(y, p_{\mathrm{T}}) \frac{\sum\limits_{I} P_i(\mathrm{d}E/\mathrm{d}x)_{y,p_{\mathrm{T}}} - B \sum\limits_{R} P_i(\mathrm{d}E/\mathrm{d}x)_{y,p_{\mathrm{T}}}}{N_I - B N_R}, \tag{4.10}$$

where:

- C_i are the correction factors defined in Eq. 4.9,
- $\sum\limits_{I} P_i(\mathrm{d}E/\mathrm{d}x)_{y,p_{\mathrm{T}}}$ is the sum of probabilities P_i defined in Eq. 4.5 for all tracks in a (y, p_{T}) bin, for target-inserted (I) events,
- $\sum\limits_{R} P_i(\mathrm{d}E/\mathrm{d}x)_{y,p_{\mathrm{T}}}$ is the sum of probabilities P_i defined in Eq. 4.5 for all tracks in a (y, p_{T}) bin, for target-removed (R) events,
- B - is the normalization or scaling factor applied to target removed events described in Sec. 4.4.4.1, and

– N_I and N_R are the number of events recorded with target inserted and target removed, respectively.

4.4.5.1 Estimation of Statistical Uncertainty

Due to the usage of identity method (Sec. 4.4.3) in calculation of $y - -p_T$ spectra, it is not clear how to propagate the statistical errors in Eq. 4.10 from the raw $p - -p_T$ data. Since a direct propagation of uncertainties is not possible, a bootstrapping technique developed for NA61/SHINE analyses in [190] was employed.

Bootstrapping is a powerful resampling technique in statistics, used to estimate the uncertainty associated with a given estimator, such as the mean or standard deviation [198]. The method involves repeating the entire analysis process multiple times on samples built by resampling the original data. These simulated samples, also referred to as bootstrap samples, are created by randomly selecting collision events with replacement. By creating a large number of these resampled data sets, and computing the desired statistic for each of them, an empirical distribution of the statistic can be constructed. This distribution can then be used to estimate uncertainties, such as confidence intervals and errors. Bootstrapping is particularly useful when the underlying distribution of the data is unknown or when traditional parametric methods may not be applicable or reliable.

The problem of estimating the statistical uncertainty was solved by repeating the $\mathrm{d}E/\mathrm{d}x$ analysis on different simulated bootstrap samples constructed from collision events in the real data. In a bootstrap sample, each of the ~30 million selected events can appear m times, where m follows the multinomial distribution:

$$P(m) = \binom{M}{m} p^m (1-p)^{M-m} \tag{4.11}$$

where M is the total number of events, and $p = 1/M$. The probability of a real event to be skipped from the bootstrap sample or to be included exactly once is ~37%. It decreases to ~18% for appearing twice, and quickly approaches zero for higher m. The expectation value of an event to be included in a bootstrap sample is one.

A hundred bootstrap samples, each containing nearly 30 million events, were created by random sampling with replacement of real events from p–p data. Particle yields are generated for each bootstrap sample. The standard deviation of yields from these bootstrap samples is set as the statistical uncertainty of the measurement. The average statistical uncertainty for hadrons in all measured bins is shown in Table 4.4.

4.4.5.2 Estimation of Systematic Uncertainties

There are multiple sources of systematic uncertainties in the final particle yields. These include the method of event and track selection ($\sigma_{\text{Selection}}$), the feed-down

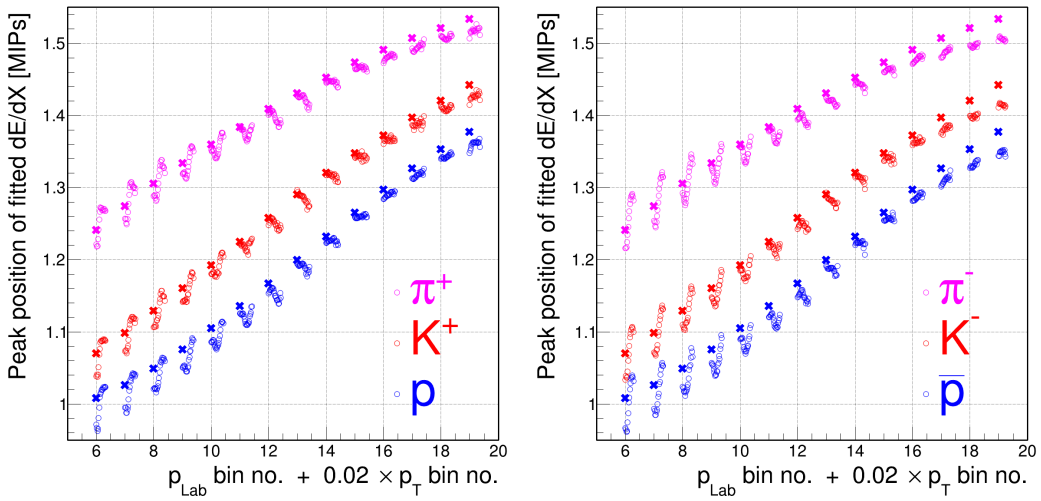

Figure 4.18: Fitted $\mathrm{d}E/\mathrm{d}x$ peak positions of positive (left) and negative (right) charged particles in different momentum bins. The small p_T dependence for each momentum is shown by adding a small p_T-dependent shift within the momentum bin. The expected peak positions from the Bethe-Bloch parametrization for each momentum bin are also labelled with "**x**".

effect of particle decays ($\sigma_{\text{Feed-down}}$), and the $\mathrm{d}E/\mathrm{d}x$ fitting procedure for particle identification (σ_{PID}).

Uncertainties of the $\mathrm{d}E/\mathrm{d}x$ identification method were estimated by evaluating the quality assurance of the fitting procedure. The fitted peak positions for positively and negatively charged particles in Fig. 4.18 exhibit a smooth dependence on p_{lab}, but also a non-trivial dependence on p_T. This was anticipated because of the established characteristics of the data, the detector, and specifically, the $\mathrm{d}E/\mathrm{d}x$ calibration and reconstruction procedure. A potential explanation for this unanticipated dependency could be a faulty y-dependence in the calibration, which also leads to a drift in the $\mathrm{d}E/\mathrm{d}x$ values as the azimuthal angle ϕ varies [190]. To estimate the systematic uncertainty due to these fit variations, the distribution of the Bethe-Bloch-normalized relative peak positions x_K/x_π and x_p/x_π (see Fig. 4.19 left) were checked for both positive and negative charges in all (p_{lab}, p_T) bins. The RMS of these distribution for antiprotons is shown in Fig. 4.19 (right). The fitted peak positions were varied by ±RMS (e.g., ± 0.7% for antiprotons). The difference in yields from these varied $\mathrm{d}E/\mathrm{d}x$ fits was estimated to be the systematic uncertainty of the fits.

Uncertainty related to the rejection of events with off-time beam particles was estimated by changing the time window width by $\pm\,1\,\mu$s with respect to the nominal value, and assigning the maximum difference as the uncertainty. The potential systematic bias arising from unintended loss of inelastic collision events because of the interaction trigger, meant to exclude only elastic scattering events, was estimated

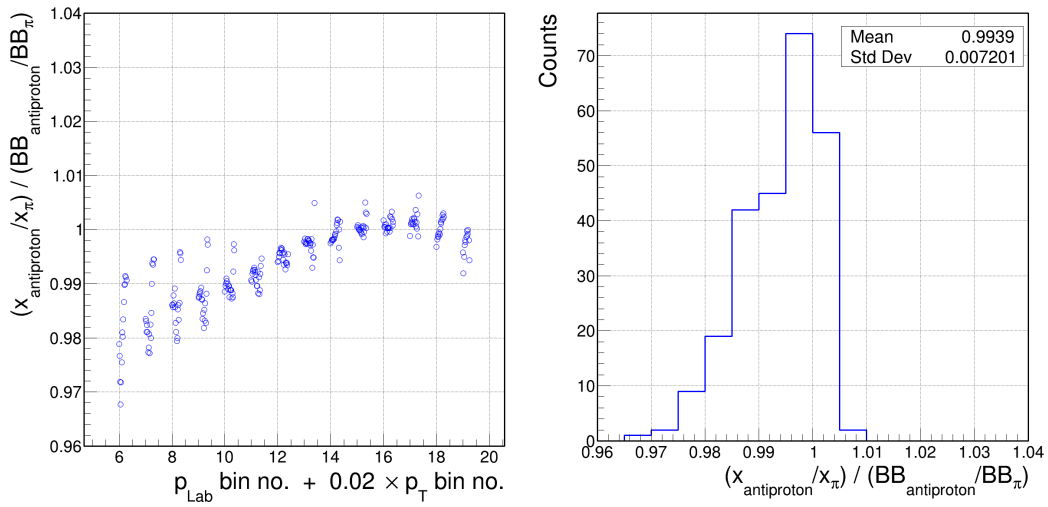

Figure 4.19: (Left) Bethe-Bloch-normalized relative peak positions for protons in different momentum bins. The p_T dependence for each momentum is shown by adding a small p_T-dependent shift within the momentum bin. The distribution of all fitted Bethe-Bloch-normalized relative peak positions for antiprotons. The RMS of such distributions were used to estimate the systematic uncertainty due to the fitting procedure.

by comparing outcomes with and without applying the S4 trigger in the Monte Carlo simulation. Uncertainty in the target-removed normalization, which came from the selection window of the z-position of the fitted main vertex within the target, was estimated by varying the selection criteria by $\pm 10\,\mathrm{cm}$ (50%) around the nominal value. Similarly, the choice of the acceptable track impact parameter ranges and the minimum measured track clusters requirements can also add systematic bias. This was estimated by independently varying the minimum number of requested points on a track in all TPCs by ± 5 (33% of nominal value).

The systematic uncertainty in the feed-down correction is based on the `EPOS-1.99` model, which effectively describes the available cross section data for strange particle decays at the level of a few percent (e.g., Λ decays [181, 199], as well as $K^{\pm}$ production [181]). Systematic uncertainty arises from the absence of accurate knowledge regarding the production cross sections of K^+, K^-, Λ, Σ^+, Σ^-, K^0_s and $\bar{\Lambda}$ in case of pions, and additionally Σ^+ in case of protons and $\bar{\Lambda}$ in case of antiprotons. Given that the corrections are only a few percent in the phase space region of the measurements, a small additional systematic error of 1% was assumed for pions and 2% for protons and antiprotons.

Assuming the independence of all sources of systematic uncertainties, the total systematic error can be calculated as the square root of the sum of squares of the

Table 4.4: Average Statistical and Systematic Errors For Produced Hadrons in p–p 158 GeV/c Interactions in NA61/SHINE, in all measured (y, p_T) bins.

Particle	Average Statistical Error (%)	Average Systematic Error (%)
p	4	10
$\overline{\text{p}}$	9	24
K^+	8	10
K^-	7	20
π^+	4	7
π^-	3	3

individual components:

$$\sigma^2_{\text{stat}} = \sigma^2_{\text{Selection}} + \sigma^2_{\text{PID}} + \sigma^2_{\text{Feed-down}} \tag{4.12}$$

In the analysis, it was found that the largest source of systematic uncertainty was the particle identification fits. Hence, for the purpose of the presented results, only σ_{PID} was considered. The average systematic uncertainty for hadrons in all measured bins is shown in Table 4.4.

4.4.6 Results

4.4.6.1 Preliminary Particle Spectra

The background-subtracted particle count distributions in Fig. 4.16 were corrected using the correction factors shown in Fig. 4.17. The corrected distributions were normalized per event, and also by the bin widths of the two-dimensional (y, p_T) bins. The preliminary transverse momentum particle spectra in rapidity slices for positively and negatively charged protons, kaons, and pions produced in inelastic p–p interactions at $p_{\text{beam}} = 158$ GeV/c are presented in Fig. 4.20. The figures also shows the previously-published results from Ref. [181] from the analysis of the low-statistics p–p data set from 2009. Fig. 4.20 also show the comparison of the (anti)proton spectra with the `EPOS-LHC` model.

4.4.6.2 Comparisons with Previous Measurements

The new spectra from high-statistics data were compared to the previous results from the analysis of the low-statistics 2009 p–p data. Fig. 4.21 a) and b) show these ratios for the common transverse momentum bins in sections of rapidity, for protons (top) and antiprotons (bottom), respectively. The total uncertainty of both spectra were propagated to calculate the uncertainty bands of the ratios. These ratios are equal to one in most bins within the calculated error bands. The fluctuations in the error bands is because of low statistics in the 2009 analysis.

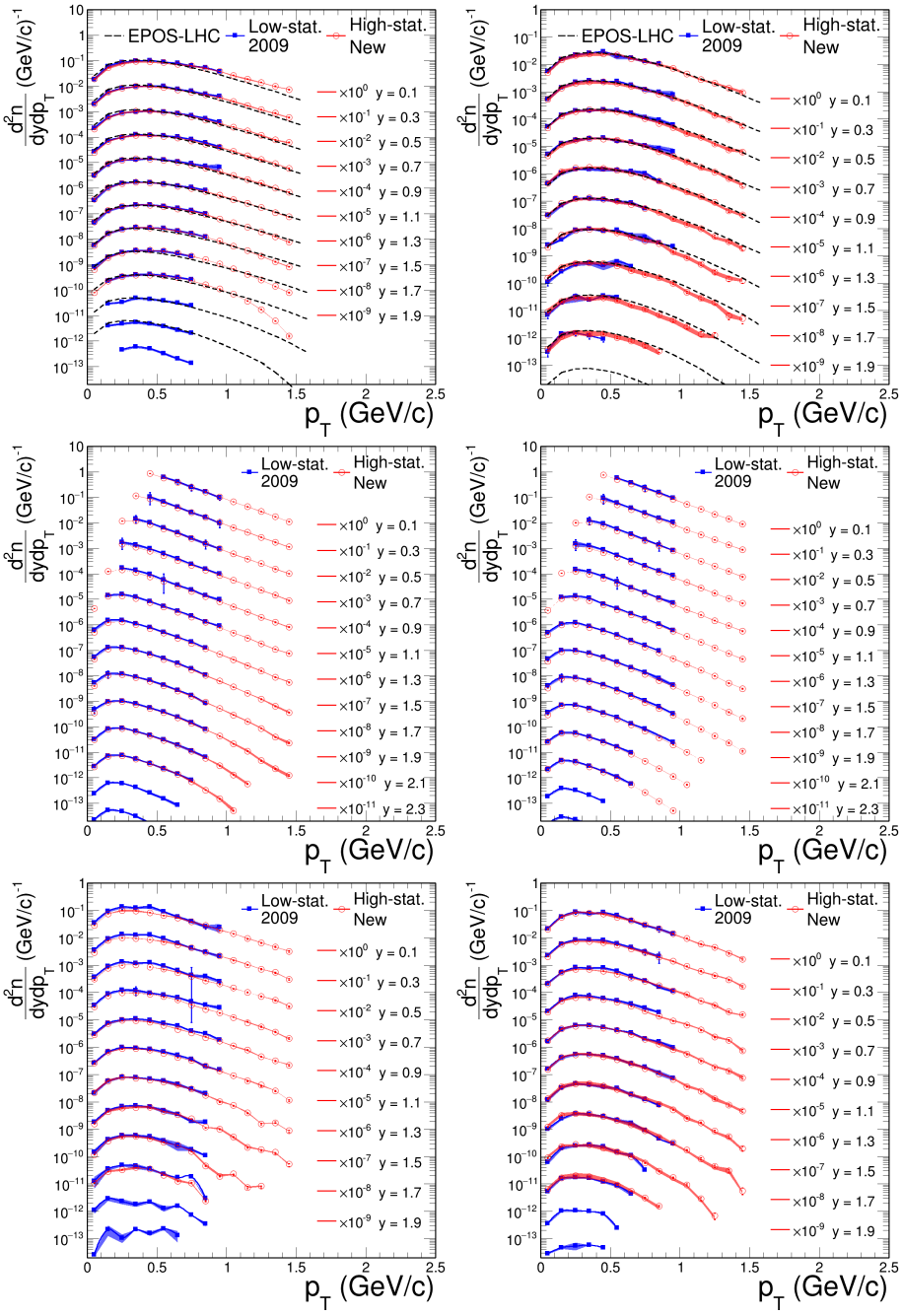

Figure 4.20: Transverse momentum particle spectra in rapidity slices for positive (left) and negative (right) charged protons (top), pion (middle) and kaons (bottom) produced in inelastic p–p interactions at $p_{\text{beam}} = 158\,\text{GeV}/c$. New results from the high-statistics p–p data set are shown in red, and the previously NA61/SHINE results from Ref. [181] are shown in blue. Shaded bands show systematic uncertainties, and error bars show statistical uncertainties. Comparison with `EPOS-LHC` is shown for protons and antiprotons in black.

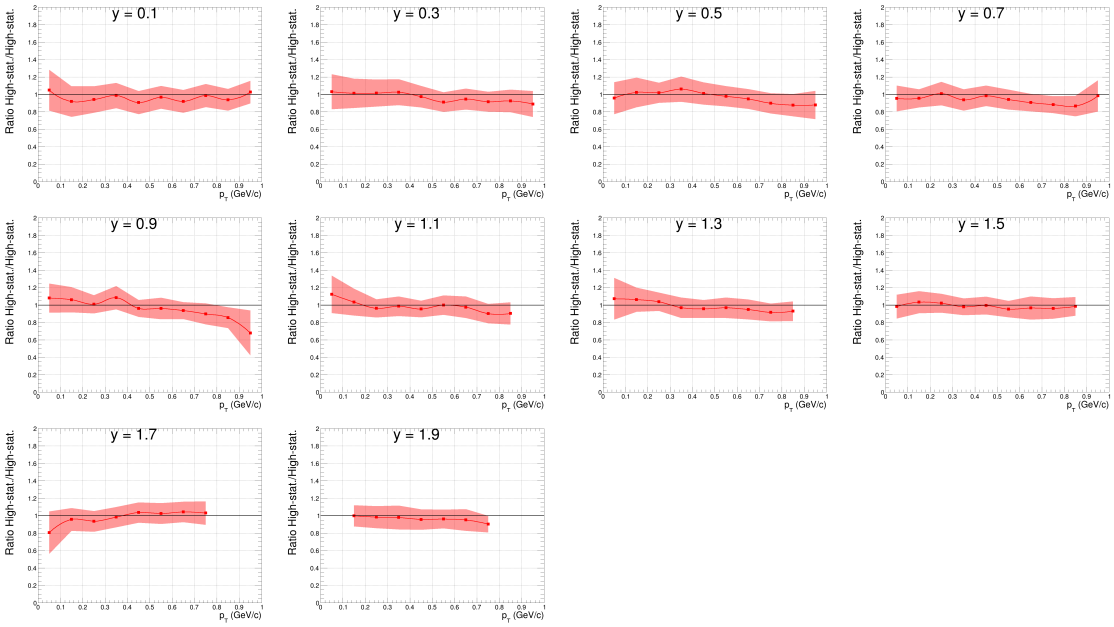

(a) Ratio for protons

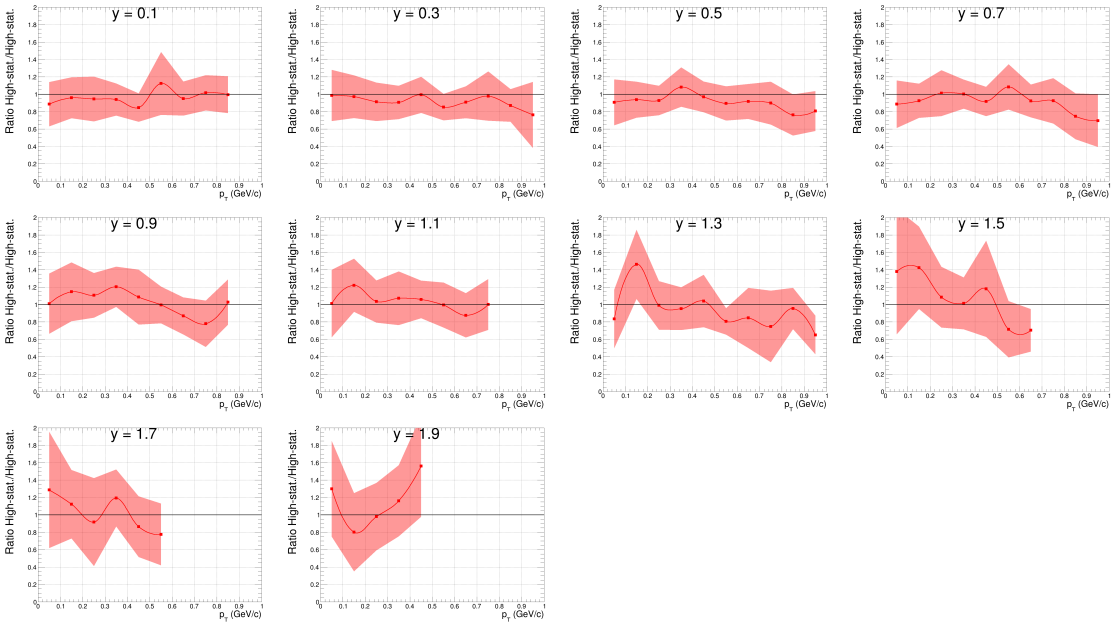

(b) Ratio for antiprotons

Figure 4.21: The preliminary particle spectra ratios between the presented high-statistics analysis and the low-statistics analysis from [181], for protons (top) and antiprotons (bottom), for inelastic p–p interactions at $p_{\text{beam}} = 158\,\text{GeV}/c$. The $y = 1$ line is highlighted. The ratio are close to one within the propagated total uncertainty bands.

As expected, compared to the previous results, the new results are able to reduce the statistical uncertainties by a factor of three for most kinematic bins. They also extend the accessible transverse momentum region to 1.5 GeV/c for all six charged hadrons. The reduction in statistical fluctuations is particularly noticeable for the antiproton production spectra.

For the previous measurements, the systematic errors were comparable to the statistical errors. For the new high-statistics measurements, Table 4.4 shows that systematic errors are now dominant for most particles. Limitations in the $\mathrm{d}E/\mathrm{d}x$ resolution of the TPCs directly affected the particle identification procedure. This was especially significant for kinematic bins with a high proton–K^+ or antiproton–K^- overlap.

If systematic errors are greater than statistical errors, decreasing the latter will not substantially improve the overall quality of results. Consequently, for further higher-precision production measurements, systematic errors need to be reduced to the level of statistical errors for them to be beneficial. A better quality of the $\mathrm{d}E/\mathrm{d}x$ signal and other improvements after the NA61/SHINE detector upgrades (see Sec.5.2) will help in the reduction of systematic uncertainties in future measurements.

4.4.6.3 Comparisons with `EPOS-LHC`

The new hadron spectra were also compared to the latest `EPOS-LHC` hadronic generator model in Fig. 4.22. `EPOS-LHC` is an updated version of the `EPOS 1.99` model that incorporates several improvements to provide a better description of experimental measurement obtained from experiments at the LHC at CERN. `EPOS-LHC` was chosen for these comparisons as it can offer a more accurate modeling of the hadronization process in high-energy particle collisions.

The ratios between data and `EPOS-LHC` indicate deviations in the (y, p_{T}) spectra of more than 20% between the measurements and the model, especially for antiprotons in the new high p_T, y regime. These comparisons suggests that `EPOS-LHC` requires further refinement to better match the experimental results. Improving physics models, including newer versions like `EPOS4` is an important aim of these new results. Complementing the results from LHC experiments with these new lower-energy measurements at NA61/SHINE can help build a more comprehensive understanding of the fundamental interactions and properties of matter across a wide range of energies.

4.4.6.4 Antiproton Differential Production Cross Section

As shown in Sec. 3.6, the antinuclei differential production cross sections as a function of kinetic energy are an important measurement to boost cosmic-ray interpretations. These measurements are needed as an input for Galactic cosmic-ray transport models,

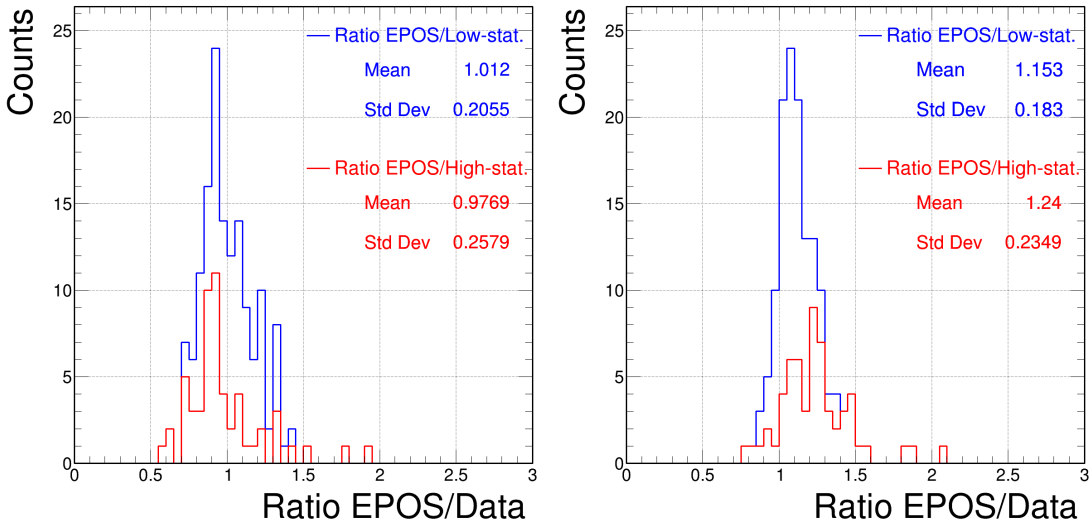

Figure 4.22: Ratios of the (y, p_{T}) spectra between NA61/SHINE measurements and `EPOS-LHC` hadronic generator model, for p–p 158 GeV/c. Ratios are shown for the previous low-statistics measurements (blue) as well as the new high-statistics measurements (red), for the proton spectra (left) and the antiproton spectra (right).

where they are used to calculate the antinuclei source terms and their flux received at Earth. The differential production cross section of a particle can be calculated as a function of kinetic energy in the laboratory frame by modifying Eq. 4.10 as [200]:

$$\frac{\mathrm{d}\sigma}{\mathrm{d}E_{\mathrm{Kin}}} = \frac{\sigma_{trig}}{N_I - B \cdot N_R}\left(\frac{\mathrm{d}n_I - B \cdot \mathrm{d}n_R}{\mathrm{d}E_{\mathrm{Kin,\ Lab}}}\right) \tag{4.13}$$

where σ_{trig} is the trigger cross section for interactions within the target and is calculated from the interaction probability p_{int}, N_I (N_R) are the number of events analyzed with target inserted (removed), $\mathrm{d}n_I$ ($\mathrm{d}n_R$) is the number of particles produced with target inserted (removed) corrected for acceptance and detector efficiency, and $\mathrm{d}p$ is the size of the lab kinetic energy bin.

The corresponding trigger cross section σ_{trig} can be calculated by taking into account the exponential beam attenuation in the target, the reduction of beam intensity due to interactions upstream of the target, and the reduction of the downstream interaction probability in target-inserted operation [201]. It is calculated according to the formula [202]:

$$\sigma_{trig} = \frac{A}{\rho_H \cdot L \cdot N_A} \ln\left(\frac{1}{1 - p_{int}}\right), \tag{4.14}$$

where L, N_A, A and ρ_H denote, respectively, the target length (20 cm), the Avogadro constant, the atomic mass of hydrogen (1.00794 g) and the liquid hydrogen target density (0.07 g/cm^3). The interaction probability p_{int} in the LHT has to be extracted

from the measured event counts in the target-inserted and target-removed data:

$$p_{int} = \frac{P^I_{T2} - P^R_{T2}}{1 - P^R_{T2}}, \quad \text{where} \tag{4.15}$$

$$P^{I/R}_{T2} = \left[\frac{N(T1 \;\&\&\; T2)}{N(T1)}\right]^{I/R}, \tag{4.16}$$

where $N(T1 \;\&\&\; T2)$ are the number of events satisfying both T1 and T2 trigger conditions, and $N(T1)$ are the number of events satisfying the T1 trigger condition. The measured uncorrected values of trigger cross section and σ_{trig} for Runs 2009, 2010 and 2011 are shown in Table 4.5 [200].

To calculate the final corrected trigger probability, the trigger bias caused by the S4 counter needs to be taken into account. The bias can be caused by inelastic events which have an S4 hit, resulting in a loss of inelastic events. It can also be caused by elastic interactions which do not have an S4 hit (false positives).

The correction procedure for p–p data in NA61/SHINE was established in [202], using Monte Carlo simulations of the proton beam with divergence corresponding to the beam properties during data taking. The average measured p–p inelastic trigger cross section (32.0 ± 0.6 mb) was found to agree with the PDG value of 31.78 mb [201]. The PDG value was used for the subsequent cross section calculation in Eq. 4.13.

Fig. 4.23 shows the measured antiproton differential production cross section as a function of kinetic energy in the laboratory frame, for p–p interactions at 158 GeV/c. As particle identification was possible only for tracks with momentum higher than 4 GeV/c, the production could be measured only for particles with kinetic energy above ~3.6 GeV. The ratio of this measurement to the `EPOS-LHC` model is also presented. As discussed earlier in Sec. 3.6.1, `EPOS-LHC` was found to overpredict data by ~10–20%, particularly at low kinetic energies with the highest $\bar{p}$ production. These new measurements can aid in refining the antiproton production parametrizations used in cosmic-ray studies. They can also help further fine-tune hadronic generator models, and contribute to constraining the astrophysical production of antinuclei within our Galaxy.

Table 4.5: Measured uncorrected trigger cross sections and σ_{trig} for Runs 2009, 2010 and 2011.

Run	p_{int}	σ_{trig} (mb)
2009	0.0225 ± 0.0004	27.0 ± 0.4
2010	0.0240 ± 0.0003	28.8 ± 0.3
2011	0.0235 ± 0.0004	28.2 ± 0.4

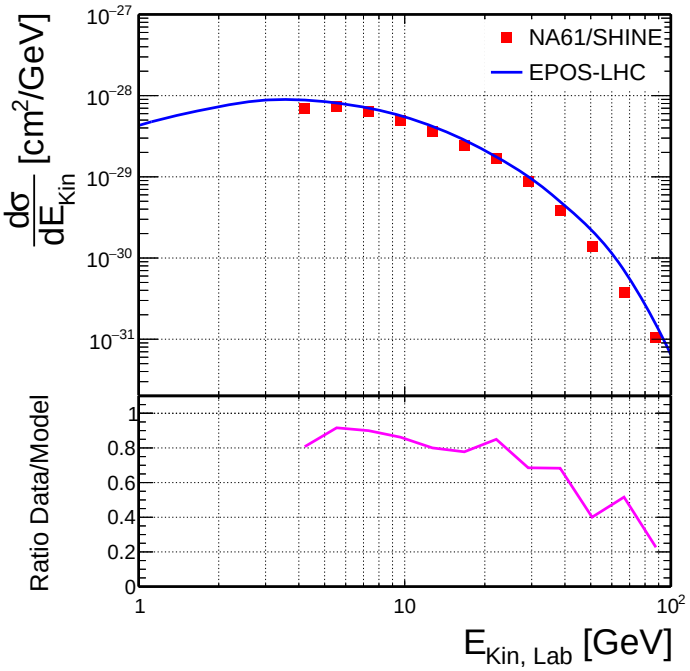

Figure 4.23: The measured antiproton differential production cross section as a function of kinetic energy in the laboratory frame for p–p interactions at 158 GeV/c. The error bars are smaller than the data point symbols. The ratio of data to the `EPOS-LHC` model is also presented in the bottom panel.

4.5 Measurement of Deuteron Production in NA61/SHINE

This section presents the tof–dE/dx analysis to estimate the production of deuterons in p–p interactions at $p_{\text{beam}} = 158\,\text{GeV}/c$. Apart from the importance of these results for both nuclear physics and interpretation of cosmic-ray measurements, this analysis will also serve as the basis of future antideuteron searches with ultra-high statistics at NA61/SHINE (see Sec. 4.6).

Unlike antideuterons, deuterons have been measured in cosmic rays [203, 204], and they are the most abundant secondary cosmic-ray species in the Galaxy. Cosmic-ray deuterons are known to disintegrate during the nuclear processes that take place in star formation. Therefore, unlike primary cosmic-ray particles like protons and helium, they are not anticipated to be accelerated in supernova remnants. Rather, deuteron formation in CRs is understood to be mainly because of CR interactions with the ISM [205]. These secondary cosmic-ray deuterons can come from two main channels: the fragmentation of CR nuclei like ^{3}He and ^{4}He with the interstellar

hydrogen and helium, and also from the resonance reaction:

$$p + p \rightarrow d + \pi^{+} \tag{4.17}$$

Fragmentation is the main source of CR deuterons, because the resonance production channel is only possible at very low collision energies below 1 GeV. Deuteron production in this process happens in a narrow energy distribution (FWHM ~320 MeV) with a maximum energy of around ~0.6 GeV [92, 206]. Besides these two mechanisms, deuteron production in p–p and p–A interactions has also been measured in ground-based collider experiments, for example via:

$$p + p \rightarrow p + \overline{n} + d \tag{4.18}$$

This third deuteron production mechanism was discussed in Sec. 3.2 within the framework of the coalescence model, where free nucleons resulting from CR–ISM interactions can coalesce to form deuterons. Such production sources have not been incorporated yet in the standard calculation of the secondary CR deuteron flux. In collider experiments, both resonance and coalescence production can contribute at low momentum (see Sec. 4.5.1.1). Fig. 4.24 (left) shows deuterons produced via resonance at low energies below ~1 GeV, as well the predictions from various models at higher energies.

Is is important to note that of the three deuteron-producing mechanisms described above, coalescence is the only process that also allows the formation of secondary antinuclei like antideuterons and antihelium. Understanding deuteron production in these types of interactions is a necessary first step to understand how CR antinuclei are produced [92]. This can also help towards developing a quantum mechanical description of the (anti)nuclei formation process [90, 125–127].

4.5.1 Deuteron Search in Proton–Proton Interactions

The NA49 experiment [207], the predecessor of NA61/SHINE at CERN-SPS, analyzed Pb–Pb interactions at 158 GeV/c with a Pb beam. It was demonstrated that both deuterons and antideuterons can be identified in this experimental setup [208]. While measurements from heavy-ion collisions, shown in Fig. 4.24 (right), cannot be directly applied to p–p interactions due to the large difference in the system size (see discussion in Sec. 3.5.2), the NA49 analysis demonstrated the feasibility of a similar tof–dE/dx analysis of the high-statistics p–p data sets in NA61/SHINE.

It is worth noting that deuteron production is quite rare in p–p interactions at SPS energies of ~100–400 GeV. For $p_{\text{beam}} = 158$ GeV/c, the coalescence parametrization developed in [92, 93] predicted a per-event production probability of 0.0004, with an uncertainty band from 0.0002–0.0009. This can be seen in Fig. 4.24 (left), where the total deuteron production cross section (with is equal to the total p–p interaction cross

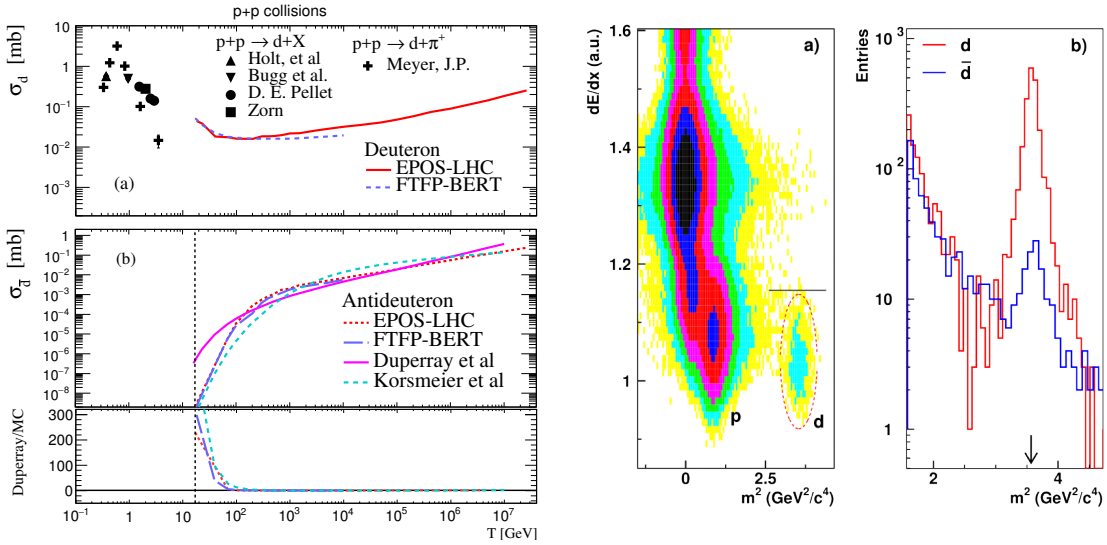

Figure 4.24: (Left) d and $\overline{d}$ total production cross section in p–p collisions. Expected d production from Duperray's parametrization [209] has been added. In the lower panel, ratio of Duperray to MC predictions are compared for $\overline{d}$. Vertical broken lines show the $\overline{d}$ production threshold. Figure adapted from [92]. (Right) (a) $\mathrm{d}E/\mathrm{d}x$ versus m^2 for positive-charged tracks in the momentum interval $7 < p < 8\,\mathrm{GeV}/c$. Deuterons can be identified. (b) m^2-distributions for both charges for momenta from 4 to $10\,\mathrm{GeV}/c$ after $\mathrm{d}E/\mathrm{d}x$ PID cut for $d(\overline{d})$ was applied. Figure adapted from [208].

section × deuteron production probability in a p–p interaction) at kinetic energies around ~100 GeV was estimated in [92] to be close to 0.02 mb. Using these estimates, about ~10,000–60,000 deuterons should have been produced in the ~60 million p–p interaction events recorded in NA61/SHINE. However, because of the limited phase space acceptance of the detector, only a fraction of the total deuterons produced can be identified.

To estimate the phase space acceptance for deuterons, about 2.7 trillion p–p interactions were simulated at $p_{\mathrm{beam}} = 158\,\mathrm{GeV}/c$. Deuteron production in these interactions was simulated by applying the coalescence condition for seven different values of the coalescence momentum p_0 in the multiparticle coalescence model described in Sec. 3.3. Fig. 4.25 (left) presents the predicted deuteron rapidity spectra in the center-of-mass frame. While most of this rapidity region is theoretically accessible with the $\mathrm{d}E/\mathrm{d}x$-only identification strategy using energy loss in the TPCs, the additional ToF information is essential for deuteron identification due to the extremely high background of $q = 1$ charged particles. The deuteron rapidity region accessible to the TOF detectors is represented within the vertical black lines, and coincides with peak deuteron production in the center-of-mass frame's backward hemisphere.

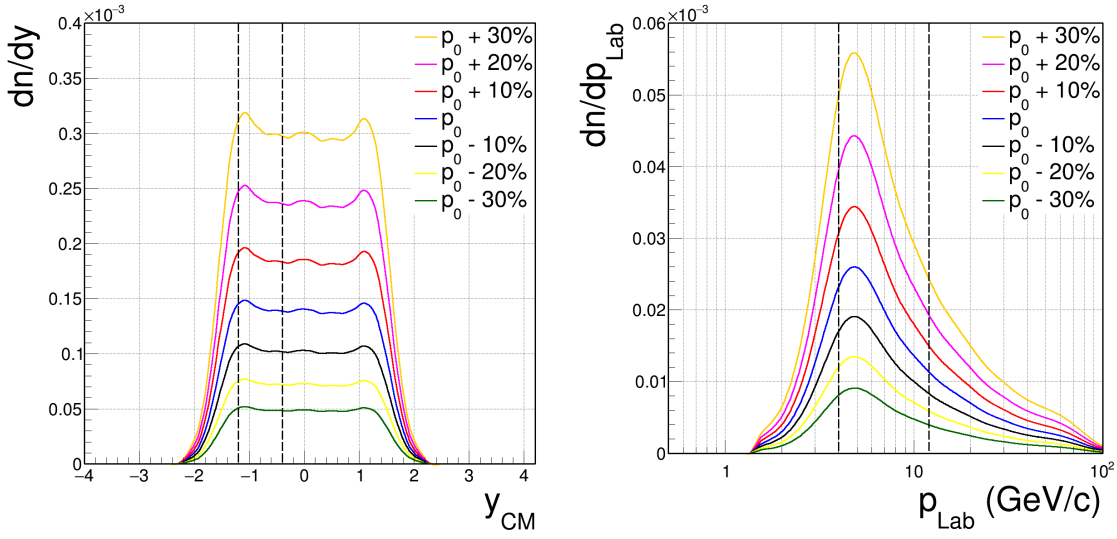

Figure 4.25: Simulated deuteron spectra, for rapidity in the center-of-mass frame (y_{cm}) (left), and momentum in the laboratory frame (p_{Lab}) (right). To generate these distributions, about 2.7 trillion p–p interactions were simulated at $p_{\text{beam}} = 158\,\text{GeV}/c$, and the conditions from the coalescence model were applied for seven different values of the coalescence momentum p_0 (see Sec. 3.3 for details.)

As the available energy in this collision system is limited ($\sim\sqrt{s} = 17.3\,\text{GeV}$), deuterons in these interactions are mostly generated at low momentum. This is because of their relatively larger mass compared to commonly produced hadrons like pions, kaons and protons. Fig. 4.25 (right) shows the deuteron lab momentum spectra predicted by the coalescence model for different values of p_0. The vertical black lines illustrate that most deuterons are expected to be produced within the momentum phase space that is accessible in NA61/SHINE in the $tof - \text{d}E/\text{d}x$ analysis.

4.5.1.1 Limitations of dE/dx-based Deuteron Identification

The identification of low-momentum deuterons is challenging. As evident from Fig. 4.26 (left), which shows the average number of clusters on a track as a function of track momentum, low-momentum tracks tend to be shorter in length, as the magnetic field quickly bends them out of the detector. The track selection cuts (see Sec. 4.4.1) based on the total number of dE/dx clusters along the track can penalize otherwise well-reconstructed low-momentum tracks. To solve this issue, a new selection cut based on the ratio of measured to potential clusters along the track was developed. Potential clusters are the maximum number of dE/dx clusters a track is expected to have along its trajectory, and it depends on the TPC construction and the track topography. It was found that selecting tracks which had this ratio between 0.7 and 1.0 optimized the selection of deuterons at low momentum.

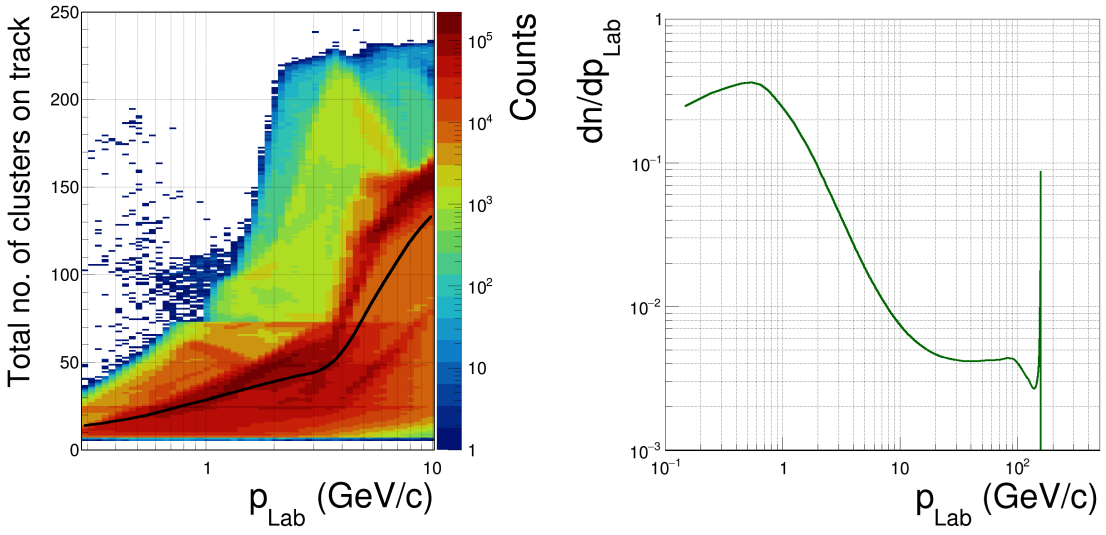

Figure 4.26: (Left) The distribution of track momentum versus total number of clusters on a track for all selected low-momentum tracks, without the minimum cluster requirement cuts. A profile histogram showing the average number of clusters on a track as a function of momentum is overlaid to help visualize the proportional relationship between the two variables. (Right) The momentum spectra of secondary protons produced in p–p interaction at 158 GeV/c, predicted using `EPOS-LHC`.

Fig. 4.27 (left) shows the truncated mean $\mathrm{d}E/\mathrm{d}x$ for all particle tracks in the high-statistics p–p data at 158 GeV/c, in the particle momentum range between 100 keV/c and 100 GeV/c. Fig. 4.27 (right) shows how the new, optimized cuts boosted particle identification in the low-momentum tails. About 1100 deuteron tracks could be counted in this tail region. However, the production of primary deuterons in processes like Eq. 4.17 and Eq. 4.18 in p–p interactions has a momentum threshold which depends on the beam proton's momentum. From energy–momentum conservation, the deuteron production threshold for $p_{\mathrm{beam}} = 158\,\mathrm{GeV}/c$ is ~1.4 GeV/c in the laboratory frame. This "boost" can be seen clearly in the simulated primary deuteron spectra in Fig. 4.25 (right). It is, in fact, the reason why background production of (anti)nuclei in CR–ISM interactions is boosted to higher kinetic energies, as compared to exotic processes like dark-matter decays, which happen in the ISM rest frame.

The source of these low-momentum deuterons was investigated. The background-subtraction process described in Sec. 4.4.4.1 was checked, but no excess of deuteron events were found from the target holders of the LHT. Since the interactions of secondary protons (i.e., protons produced in the interaction of the beam proton with the LHT) within LHT target cannot be measured directly, `EPOS-LHC` was used to estimate the total number, as well as the momentum distribution of secondary protons produced in 60 million p–p interaction at 158 GeV/c (see Fig. 4.26 (right)).

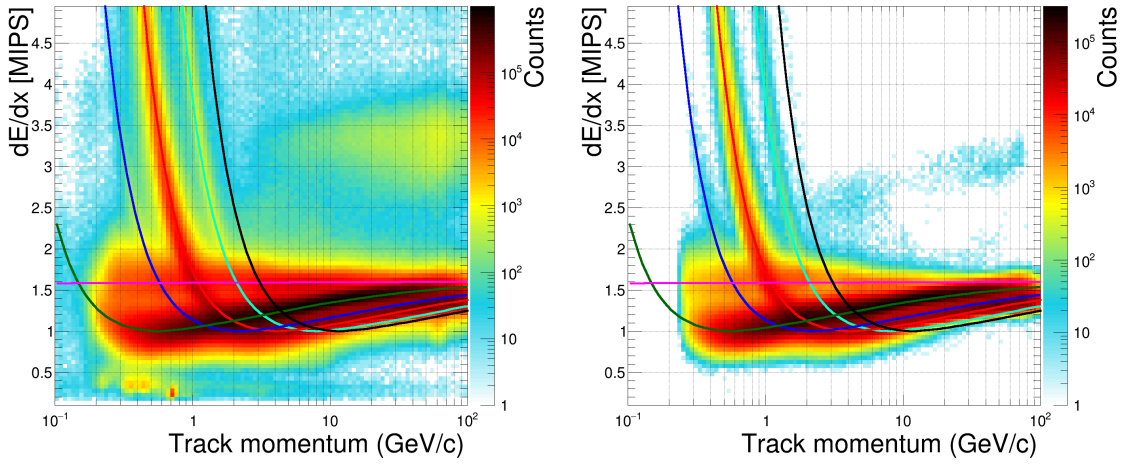

Figure 4.27: $\mathrm{d}E/\mathrm{d}x$ versus momentum distribution for (left) all TPC tracks, and (right) tracks selected by the optimized deuteron selection cuts described in Sec. 4.5.1.1. The mean $\mathrm{d}E/\mathrm{d}x$ for positrons (magenta), pions (green), kaons (blue), protons (red), deuteron (azure) and tritons (black), is superimposed on selected particle tracks from the high-statistics p–p data, for particle momentum range between 100 keV/c and 100 GeV/c. The particle identification procedure is discussed in Sec. 4.4.2.

The secondary protons were found to be produced almost uniformly throughout the LHT, and hence their interaction length was assumed to be half of that of beam protons in the LHT. p–p interaction cross sections of these low-momentum secondary protons with the protons in the LHT were obtained from the Particle Data Group (PDG) [210]. The deuteron production cross sections in these low-energy p–p interactions was obtained from Fig. 4.24 (left), via the dominant resonance production channel (i.e., Eq. 4.17). This calculation predicted the production of about 2400 secondary deuterons, most with momentum below the 1.4 GeV/c threshold for primary deuterons. After taking into account detector acceptance and inefficiencies, this process could completely explain the observed low-momentum deuteron tail seen in Fig. 4.27 (right).

4.5.2 Particle Identification Based on Time of Flight and Energy Loss Measurement ($tof - \mathrm{d}E/\mathrm{d}x$)

For particles with momentum higher than 2 GeV/c, the identification of primary deuterons in the $\mathrm{d}E/\mathrm{d}x$-only analysis described in 4.4.2 could not be achieved because of the excessive background from other positive-charged particles. Neither the $\mathrm{d}E/\mathrm{d}x$–momentum plane (refer to Fig. 4.27) nor the y–p_{T} plane (refer to Fig. 4.13) allows for deuteron identification.

Deuteron identification was determined to be viable only in the regions of large negative rapidity, in the backward hemisphere of the center-of-mass frame (approximately $y_{cm} \sim -1$). A clean deuteron signal could be extracted by combining the $\mathrm{d}E/\mathrm{d}x$ measurements with additional m^2 measurements from the ToF detectors. Particle identification was performed using the $tof - \mathrm{d}E/\mathrm{d}x$ analysis.

4.5.2.1 Additional TOF-Specific Track Selection Cuts

The tof–$\mathrm{d}E/\mathrm{d}x$ analysis requires additional track selection cuts which are specific to the ToF systems. This ToF measurement is calibrated by extrapolating particle tracks in the MTPCs to the ToF walls. The extrapolated scintillator pixel's TDC and ADC channels are checked if they are above threshold. More detailed corrections take into account the charge deposition and relative position of the incident particle in each ToF pixel. These were applied after the standard event and track selection cuts described earlier in the $\mathrm{d}E/\mathrm{d}x$-only analysis. These cuts are:

1. The hit in the ToF scintillator pixel must be associated with only one reconstructed TPC track.
2. The hit pixel must be the same as the extrapolated pixel, which is found by extrapolating the reconstructed MTPC track to the TOF wall. For this technique, the last ten clusters of all MTPC tracks were fitted with straight lines in the x–z and y–z planes. The fits were extrapolated to the z-positions of all ToF pixels to find the extrapolated pixel.
3. The hit pixel must have corresponding ADC and TDC measurements [211].
4. The last point measured on the MTPC track was required to be in the last two padrows of the MTPC i.e., with $z > 575\,\mathrm{cm}$, to ensure good matching between the TPC tracks and ToF walls.
5. Track residual distance was calculated between the reconstructed global particle trajectory and the last point measured on the track in the MTPC. Fig. 4.28 shows the distribution of such residual distances, and it was required to be less than 2 cm.
6. Finally, the minimum overall efficiency of a ToF pixel used in these measurements was set to 50%. Pixel with hit efficiencies less than 50% were categorizes as dead, and were not used for measurements.

Applying these conditions provided reliable extrapolation of the MTPC trajectories toward the ToF detectors, and helped in reducing noise in the selected tracks.

4.5.2.2 Deuteron Identification using m^2 Distributions

Fig. 4.29 shows the distribution of m^2 versus $\mathrm{d}E/\mathrm{d}x$ for selected positive-charged tracks in p–p 158 GeV/c interactions in the high-statistics NA61/SHINE data. Different particles like proton, kaons and pions can be identified and the expected deuteron signal is also visible in the highlighted red box. Identification in the standard

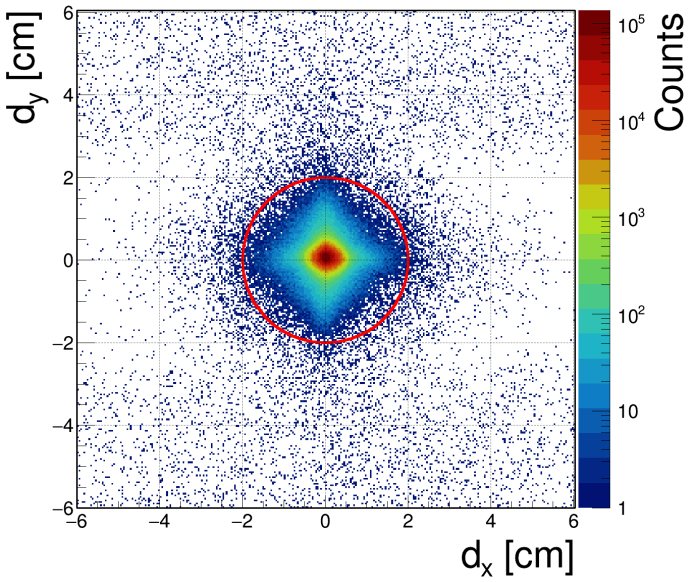

Figure 4.28: The distribution of residuals d_x and d_y between the reconstructed track and the last measured point in the TPCs for the selected positive-charged tracks in p–p 158 GeV/c interactions in the high-statistics NA61/SHINE data. The inside of the red circle represents the tracks accepted in the analysis.

NA61/SHINE tof-dE/dx analysis employs simultaneous fits with a two-dimensional function. This fit function is the product of a Gaussian function in dE/dx with the sum of two Gaussian functions, one to fit the m^2 peak and the second to fit the m^2 tails.

Due to detector effects, the high-statistics p–p data contains long pion, proton and kaon tails in the high-m^2 region, which are not modelled well by common distribution functions. The standard analysis in NA61/SHINE is conducted in a small m^2 range from -0.8 to 1.8 GeV/c^2, and deuteron contributions to the total fits are not considered [211]. For measuring deuteron yields, a new data-driven template-fitting method was developed for particle identification in this analysis. For each (p, p_T) bin, pions and positrons were separated from the other particles by identifying them using their measured dE/dx values. Fig. 4.30 shows the two black curves to illustrate their identification. Tracks above the top black curve were identified as positrons, and tracks between the two black curves were identified as pions.

To estimate the remaining kaon, proton, and deuterons contributions in the overlapping mass-squared distributions, the kinematic phase space was divided into 40 two-dimensional bins, with 10 equal-sized bins in p_{lab} between 1–20 GeV/c , and 4 equal-sized p_T bins in the range of 0–2 GeV/c . This was done to ensure that most bins had sufficient statistics for accurate fits while also being adequately sized to reduce bin-to-bin migration to less than 2%. The pion m^2 distribution in each kinematic bin

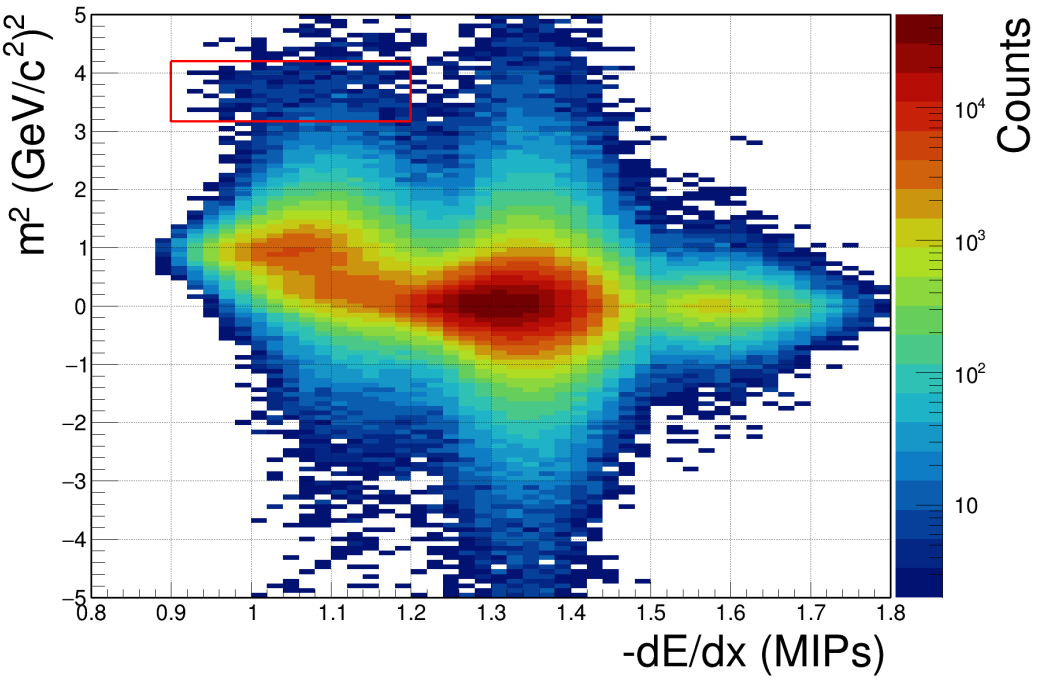

Figure 4.29: The distribution of m^2 versus $\mathrm{d}E/\mathrm{d}x$ for positive-charged tracks in p–p 158 GeV/c interactions in the high-statistics NA61/SHINE data. Different particles like proton, kaons and pions can be identified and the visible deuteron signal is also shown in the red box.

were first smoothened around the edges using the average of the nearest neighboring bins. They were then appropriately broadened for detector resolution effects and particle mass, and used as fit templates for the other particles. These data-driven mass templates were the input for the combined template fit of the higher-mass $Z = 1$ m^2 spectrum. In this technique, the fit templates had their peak positions fixed at their respective particle m^2 values, and the widths were also precalculated. The three amplitudes, one for each particle, were the only free parameters in the fit.

Fig. 4.31 shows example template fits for two (p, p_T) bins, and reveals a clear evidence of deuteron peaks. A realistic estimation of the proton tail under the deuteron peak in the m^2 distribution is of critical importance in these fits. The proton and kaon yields from the new fitting procedure were compared to the standard NA61/SHINE two-dimensional simultaneous fits for the tof–$\mathrm{d}E/\mathrm{d}x$ analysis conducted in the narrower m^2 range. It was confirmed that the ratio of the proton and kaon yields from both methods was close to one for all kinematic phase phase bins in which the fits were performed. This indicated that the new fitting procedure was robust, at least for the peak regions and hence the fitted particle yields. Fig. 4.32 shows this ratio for the fitted protons counts for each bin.

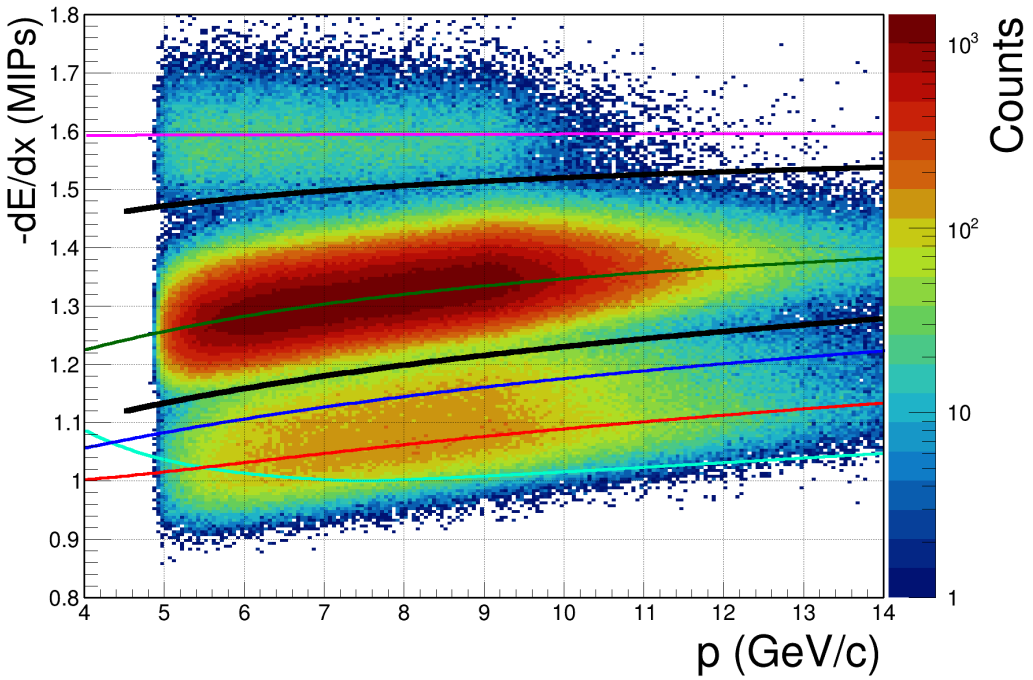

Figure 4.30: The distribution of track momentum versus $\mathrm{d}E/\mathrm{d}x$ for positive-charged tracks which have a hit in the ToF detectors, in p–p 158 GeV/c interactions in the high-statistics NA61/SHINE data. The Bethe-Bloch parametrization for different particles like pions (green), proton (red), kaons (blue), positrons (magenta) and deuterons (azure) have been added.

The estimation of the deuteron yields was done using a modified probability method, which was developed in a similar manner as for the $\mathrm{d}E/\mathrm{d}x$-only analysis in Sec. 4.4.3. The fits from the new tof–$\mathrm{d}E/\mathrm{d}x$ identification strategy were used to compute the probabilities P_i for a track being a given particle type $i = p, K, d$. After obtaining the m^2 fits described above, these probabilities can be calculated as:

$$P_i(m^2, p_{\mathrm{lab}}, p_{\mathrm{T}}) = \frac{\rho_i(m^2, p_{\mathrm{lab}}, p_{\mathrm{T}})}{\sum\limits_{i=p,K,d} \rho_i(m^2, p_{\mathrm{lab}}, p_{\mathrm{T}})}, \tag{4.19}$$

where ρ_i is the value of the fitted function for particle-type i in a given $(p_{\mathrm{lab}}, p_{\mathrm{T}})$ bin, evaluated at the m^2 of the particle. The denominator represents the total fit value for that bin at the particle's m^2. It is assumed that pions and positrons were perfectly identified using the cuts on $\mathrm{d}E/\mathrm{d}x$–momentum plane.

This modified probability technique was used to assign five probability values to each track in data, for being a pion, a positron, or kaon-like, proton-like, and deuteron like. The probabilities are either 0 or 1 if the particle was identified as a pion or an electron. However, as was the case for the $\mathrm{d}E/\mathrm{d}x$-only analysis in Sec. 4.4.3, because of the

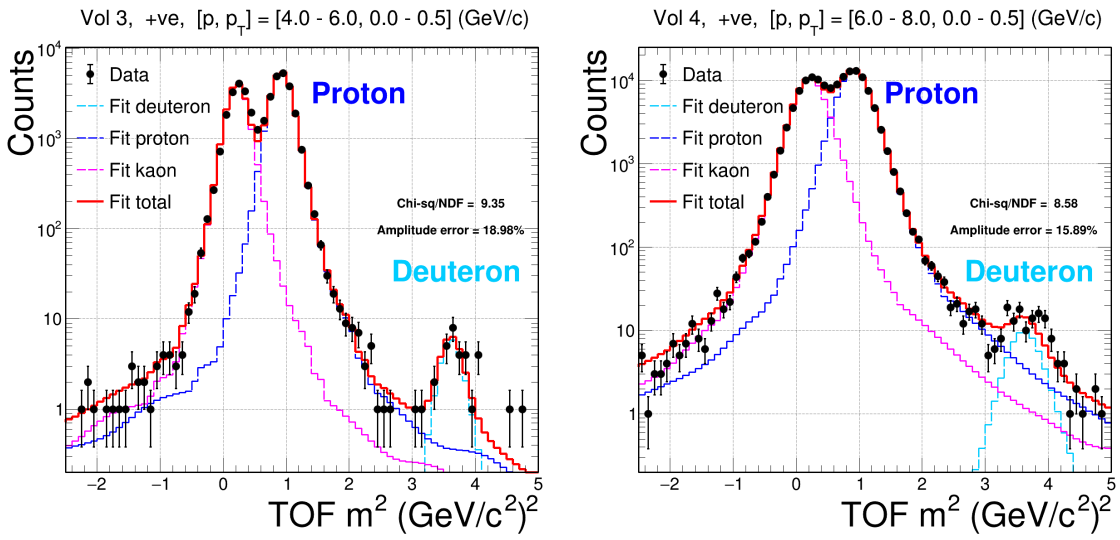

Figure 4.31: Data-driven pion mass template fits were used to fit the kaon, proton and deuteron peaks and tail regions, shown here for two example kinematic bins. Data along with fitted protons, kaons and deuterons are shown. A clear deuteron signal is visible in both bins. A correct estimate of the proton tail under the deuteron signal is of critical importance.

overlapping m^2 distributions, the calculated particle probability values for kaons, protons and deuterons range between 0 and 1. The majority of tracks exhibited either no or an extremely minimal probability of being identified as a deuteron. The fit results performed in ($p_{\rm lab}$, p_T) bins were transformed to count distribution in $(y, p_{\rm T})$ bins. The total number of raw (i.e., uncorrected) identified particles n^{raw} of particle-type i in a given kinematic bin (e.g., $(y, p_{\rm T})$) is given by [197]:

$$n^{raw}_{i=\pi,K,P,d} = \sum_{j=1}^{N_{trk}} P_i, \tag{4.20}$$

where P_i is the probability of particle type i given by Eq. 4.19, and j is the index to sum over all N_{trk} weights in the given kinematic bin.

4.5.2.3 Cross Checks for Secondary Deuteron Production

Many cross-checks were developed to account for primary versus secondary deuterons, which can be produced by the interactions of secondary protons within the LHT or the target holder. Possible contribution from beam protons interacting with various detector components was subtracted using the target-removed data, similar to the correction shown in Sec. 4.4.4.1. Deuterons can be also be produced via the fragmentation of larger nuclei, for example in the interactions of both primary and

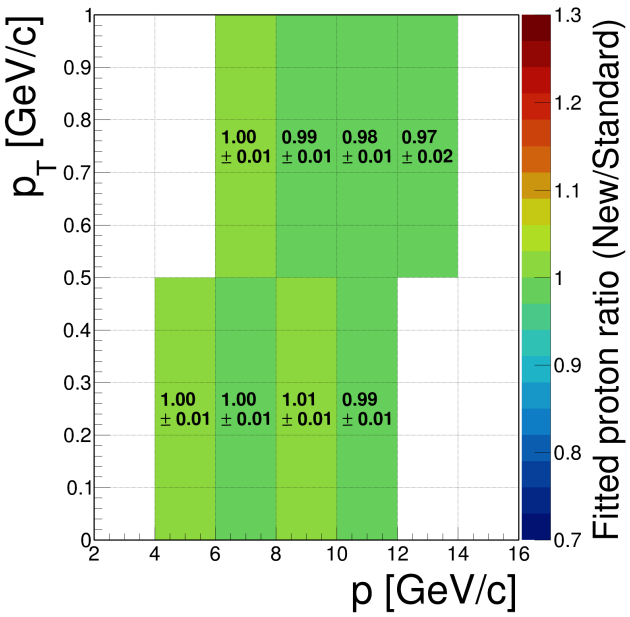

Figure 4.32: The ratio of proton yields from the new fitting procedure vs. the standard NA61/SHINE two-dimensional simultaneous fitting procedure. The ratio of the fitted proton counts from both methods was found to be almost exactly one for all kinematic phase phase bins in which the fits were performed.

secondary protons with carbon in the target holders. Fragmentation products are expected to be produced nearly at rest in the laboratory frame, at center-of-mass rapidity $y_{cm} \sim -3$. This background contribution was ruled out as the deuterons observed in data were measured at sufficiently high momentum (~4–10 GeV/c) as compared to deuterons produced via fragmentation. This lab momentum range corresponds to $y_{cm} \sim -1$ for the deuteron signal, and it is well separated from the expected phase space of fragmentation products.

Reinteractions of secondary protons within the LHT can also produce deuterons. These secondary protons are produced in the main p–p interaction, and their reinteractions with other protons in the LHT cannot be directly observed. To estimate the production of secondary deuterons via this process, a data-based estimate was developed. Fig. 4.33 shows the distribution of the z-coordinate of the main vertex of events which contain a deuteron, before and after the midpoint of the LHT [212]. All p–p events which contained a track with a non-zero probability of being a deuteron, as calculated in Eq. 4.19, were considered. Each such event was weighted by its deuteron probability, and added to the vertex-Z distribution. Background-subtraction was done by using the standard procedure developed in Sec. 4.4.4.1.

It was assumed that, on an average, secondary protons produced upstream of the target midpoint were three times more likely to interact within the LHT compared to

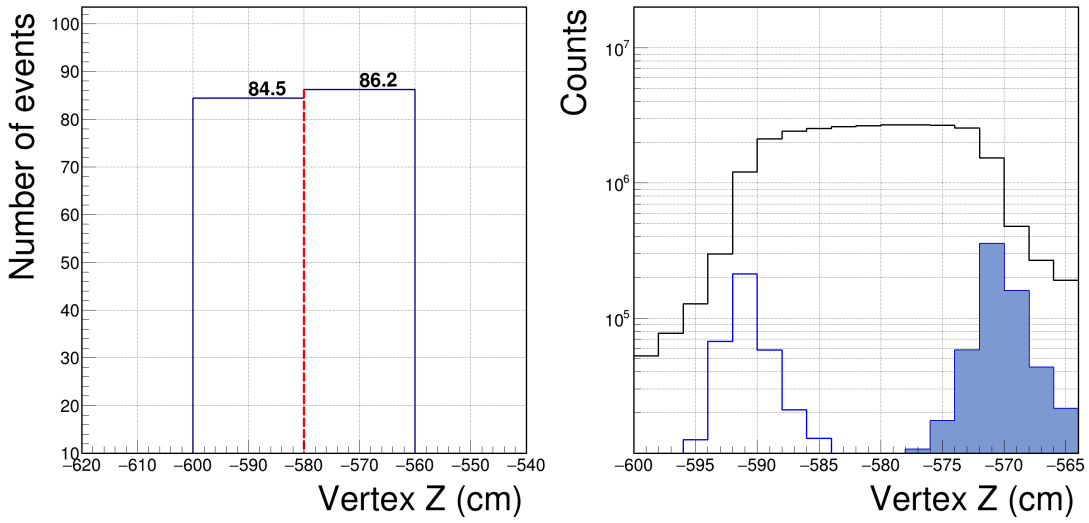

Figure 4.33: Left: The z-coordinate distribution of the main interaction vertex of those events which contain a deuteron-like track. The background-subtracted event counts have been weighted with the deuteron probabilities calculated using the modified probability method. To estimate deuteron production via secondary proton reinteractions within the LHT, events have been binned either before or after the middle of the target (red line). See 4.5.2.3 for details. Right: Vertex-Z distribution of background-subtracted target-inserted events in black. The events originating from the right target window can be seen shaded in blue.

those produced downstream. For example, if all observed deuterons were secondary in nature, the observed downstream deuteron event counts in this simplified model would have been three times the upstream event counts. Fig. 4.33 (left) shows that only a small excess of deuteron-producing events downstream of the target was observed. Using this, it was estimated that the contribution of secondary proton reinteractions to the observed deuteron production was less than 2%.

Another data-based estimate was developed to estimate deuteron production in the interactions of secondary protons with carbon in the right target window (RTW) of the LHT aquarium. About 630,000 well-reconstructed interactions of the beam proton with the right window of the LHT were selected and analyzed in the target-removed data. Fig. 4.33 (right) shows the vertex-Z distribution of such interactions in the right target window, the blue shaded region. Using the tof–dE/dx analysis, a total of six deuterons were identified in this region of the LHT. This was used to calculate the deuteron production probability in the RTW. The maximum interaction probability of the secondary protons with the right target window, $p_{int}^{Sec.\ proton-RTW}$,

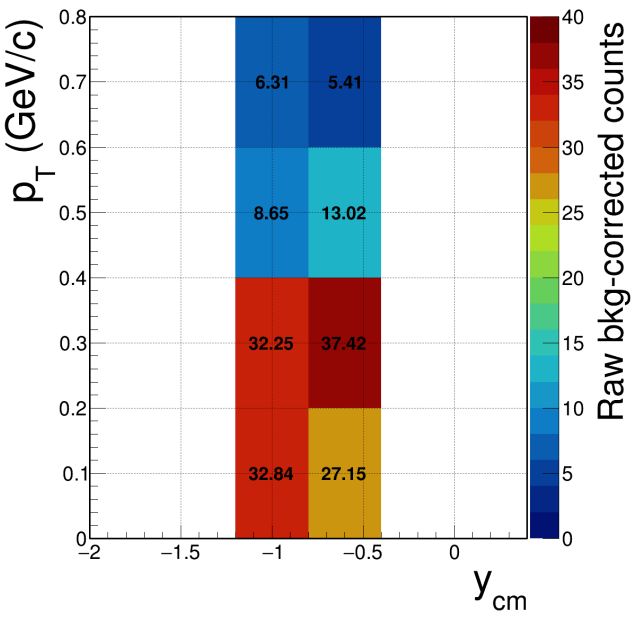

Figure 4.34: Background-subtracted raw particle count distribution in bins of transverse momentum (p_T) and center-of-mass rapidity (y_{cm}), for deuterons identified in the tof–dE/dx analysis, produced in inelastic p–p interactions at $p_{\text{beam}} = 158\,\text{GeV}/c$. The raw counts shown here have not been corrected for geometric acceptance and detector efficiencies.

was estimated as following:

$$p_{int}^{Sec.\ proton-RTW} = p_{int}^{beam\ proton-LHT}\ \frac{N_{evt,R}^{RTW}}{N_{evt,I}^{LHT}}, \tag{4.21}$$

where $p_{int}^{beam\ proton-LHT}$ is the interaction probability of the beam proton with the LHT (i.e., 2.8%), $N_{evt,R}^{RTW}$ is the number of events in target-removed data originating from the right target window, and $N_{evt,I}^{LHT}$ is the total number of background-subtracted events recorded in the LHT. This probability was calculated to be 0.06%. It was multiplied by the previously-calculated deuteron production probability, and a contamination upper-bound of ~0.1% in the observed deuteron counts was estimated.

4.5.3 Results

From the m^2 fits, about 150-200 deuteron tracks were identified in data. The background-subtracted count distribution in bins of transverse momentum (p_T) and center-of-mass rapidity (y_{cm}) for the identified deuterons, produced in inelastic p–p interactions at $p_{\text{beam}} = 158\,\text{GeV}/c$ is shown in Fig. 4.34. This is the first measurement of deuteron production in p–p interactions near the deuteron production

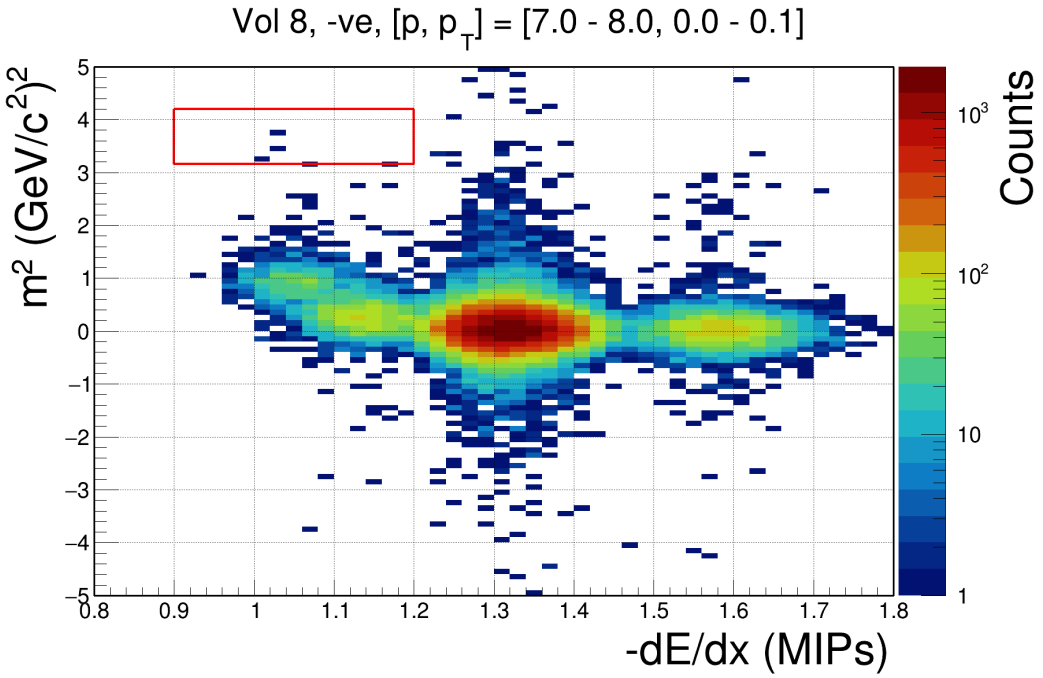

Figure 4.35: Initial measurements of negative-charged particles with the distribution of m^2 versus $\mathrm{d}E/\mathrm{d}x$ in a two-dimensional kinematic phase space bin, using the tof–$\mathrm{d}E/\mathrm{d}x$ analysis in p–p 158 GeV/c in NA61/SHINE. Antiprotons, K^-, π^- and electrons can be identified. The expected antideuteron region is also shown within the red box.

threshold. These counts are subject to an uncertainty of ~15–30%, stemming from the uncertainty in fitting deuterons within the m^2 distributions.

The raw counts have been presented here without applying corrections for geometric acceptance and detector efficiencies. Since the NA61/SHINE ToF detectors have close to ~1% acceptance, it can be estimated that about 20,000 deuteron were produced in the 30 million events selected in the high-statistics data. As discussed in Sec. 4.5.1, this is within the coalescence model's prediction of 0.02–0.09% probability of deuteron production in p–p interactions at this collision energy. In future, these measurements will be followed by a detailed spectra calculation.

4.6 Estimates of Antideuteron Production

Following the success of the first deuteron yield measurement in the p–p 158 GeV/c data set using the tof–$\mathrm{d}E/\mathrm{d}x$ analysis presented in this work, the next step was to look at the negatively charged tracks. About $5 \cdot 10^4$ antiprotons were identified by the preliminary application of the tof–$\mathrm{d}E/\mathrm{d}x$ analysis framework developed in the previous sections to analyze negative-charged tracks. Fig. 4.35 shows an example kinematic phase space bin where antiprotons, K^-, π^-, and electrons can be identified.

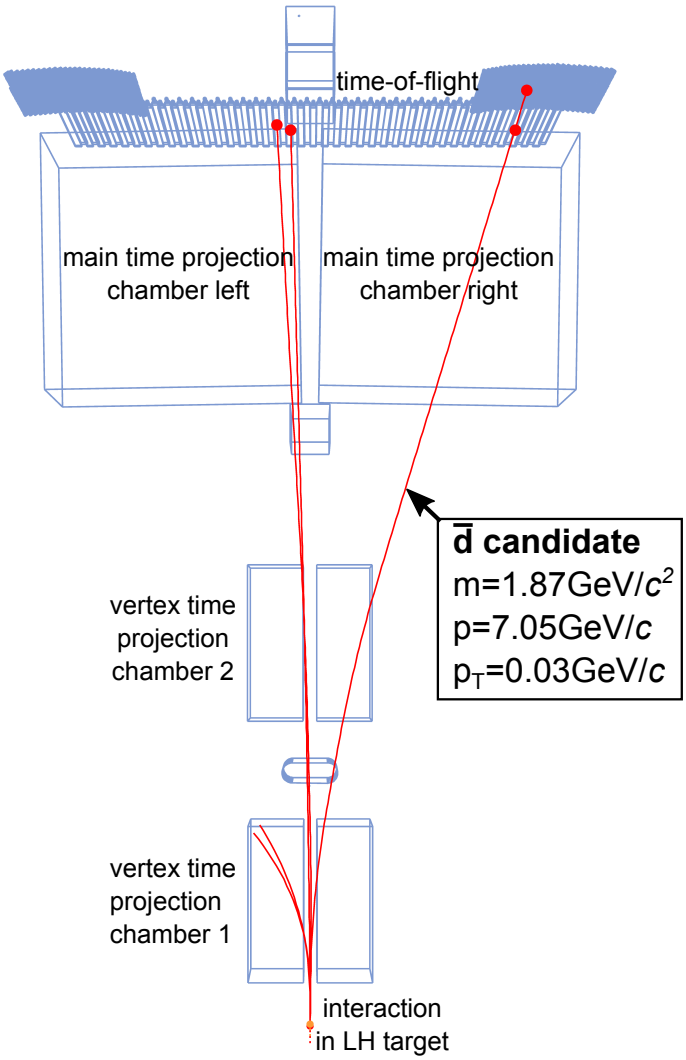

Figure 4.36: NA61/SHINE detector with an antideuteron candidate in p–p 158 GeV/c.

For the same collision system, antideuteron production is about ~1000 times smaller than antiproton production [93]. Applying this to all measurable phase space bins leads to an expectation of about 50 antideuterons in the existing p–p 158 GeV/c data sets. Fig. 4.36 shows a p–p collision event with an antideuteron candidate. In the future, after carefully considering detector effects with simulations, the first ever antideuteron production cross section measurements in p–p at p_{lab} ~100 GeV/c can be attempted.

Chapter 5
Future Outlook

5.1 Towards a Data-driven Quantum-mechanical Coalescence Model for Light (Anti)nuclei Formation

The new coalescence model discussed in Chapter 3 cannot be the final answer. The probability of (anti)nucleus formation depends on two factors: the overlap between single-particle nuclear wave functions and the separation between (anti)nucleons in phase space. In the current implementation of the coalescence model, two (anti)nucleons can coalesce to produce a larger (anti)nucleus if their momentum difference in the two-(anti)nucleon center-of-mass frame is smaller than a threshold value, called the coalescence momentum p_0.

This definition of p_0 is not adequate. For instance, as the value of p_0 is small ($\sim$100 MeV/c), it is unintentionally sensitive to two-particle correlations between the participating (anti)nucleons. This is especially crucial for (anti)nuclei production close to the production threshold energy. Furthermore, using hadronic generators that fail to describe (anti)proton and (anti)neutron spectra automatically results in a shift of p_0, making the value dependent on the hadronic generator model. Developing a deeper understanding of the underlying constituent spectra is a key step towards further improvements of coalescence modeling. Overall, the lack of available p–p data leads to uncertainties in the order of magnitude in the predicted antinuclei yield. To address issues related to hadronic generators, two-particle angular correlation (femtoscopy) studies with the 158 and 400 GeV/c data sets at NA61/SHINE will prove beneficial.

Following the precedent of similar studies on other NA61/SHINE data sets that have already been conducted [213], future angular correlation measurements of pp, $\bar{p}p$, and $\bar{p}\bar{p}$ pairs are crucial. The extracted particle correlations in light (anti)nuclei pairs can serve as an input for developing a modern data-driven quantum mechanical antinuclei formation model.

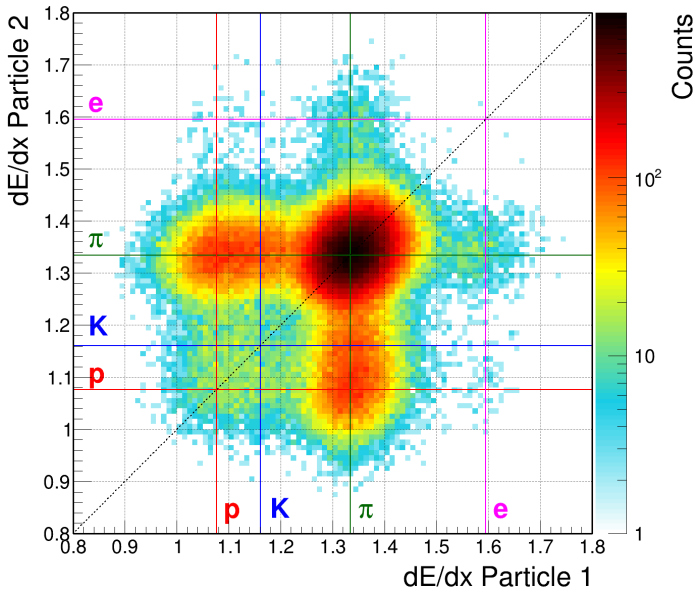

Figure 5.1: Distribution of particle pairs in p–p interactions at 158 GeV/c, in the momentum interval 8–10 GeV/c. The intersection points of the labelled horizontal and vertical lines indicates the expected positions of various particle pairs.

5.1.1 Angular Correlation Measurements

NA61/SHINE has conducted $(\Delta\eta, \Delta\phi)$ angular correlation studies before, without particle-pair identification (e.g., [213]). However, to overcome the challenge posed by incomplete particle-pair identification, preliminary studies of the high-statistics p–p data at 158 GeV/c have indicated that, for the first time, correlation studies with identified particle pairs are feasible in this energy range.

In the framework of the Particle-Set Identification (PSET) method [214] method, particle pair probability can be calculated using fits of the two-dimensional particle pair $\mathrm{d}E/\mathrm{d}x$ distributions. Fig. 5.1 (left) shows the two-dimensional $\mathrm{d}E/\mathrm{d}x$ distribution of randomly-ordered unique track pairs, such that no pair of tracks is included more than once. Paired tracks produced within a p–p interaction event are shown for a momentum slice between 8–10 GeV/c. Pion–pion pairs are the most abundant and are clearly visible, followed by proton–pion and pion–proton pairs. Because of the overlapping proton and kaon-pair distributions, identifying different types of particle pairs requires fitting the data with two-dimensional models like the bi-variate function. Similar to the probability method in Sec. 4.4.3, particle-pair probabilities can be calculated from the fits.

After the calculation of particle pair probability for a given pair of tracks, their angular correlations $(\Delta y, \Delta\phi)$ can be extracted. However, the interpretation of the measured correlations can be challenging, as they can have multiple underlying causes unrelated

to true correlations, including detector effects [214]. Experimentally, the correlation function is defined as:

$$\mathcal{C}(k) = \mathcal{N} \frac{N_{same}(k)}{N_{mixed}(k)}, \tag{5.1}$$

where $N_{same}(k)$ is the relative momentum k distribution of correlated particle pairs obtained from the same event, $N_{mixed}(k)$ is the corresponding distribution of uncorrelated pairs obtained by pairing identified particles of one event with particles from a different ("mixed") event, and $\mathcal{N}$ being a normalization factor [215].

5.1.2 Quantum-mechanical Coalescence

The simple coalescence approach does not take into account the size of the formation region [90, 165, 215]. A recent ALICE p–p study for antideuterons [215] showed that the source size can be experimentally determined from the two-particle correlations $\mathcal{C}(k)$ measured in Eq. 5.1 by equating:

$$\mathcal{C}(k) = \int \mathrm{d}^3 r S(r) |\Psi(r,k)|^2 \tag{5.2}$$

and making reasonable assumptions for the emission source function $S(r)$ (e.g., Gaussian or Hulthén) and the two-antinucleon wave function $\Psi(r,k)$ (e.g., with CATS [216]). This enables determining the source size in a quantum-mechanical model with a data-driven approach. The source size can then be used in an alternative definition of B_2 [131, 217, 218]:

$$B_2(p_T) \approx \frac{3}{2m} \int \mathrm{d}^3 q D(q) \exp\left(-R(p_T)^2 q^2\right), \tag{5.3}$$

$$\text{with } D(q) = \int \mathrm{d}^3 r |\phi_d(r)|^2 \exp(-iqr), \tag{5.4}$$

with the internal antideuteron wave function $\phi_d(r)$, the antideuteron mass m, and the source size $R(p_T)$ as function of the antideuteron's p_T. In comparison to [127], this data-driven approach can overcome the limitations of hadronic generators, as most generators only provide information on momentum correlations of nucleons and not their full phase space distributions. Although the ALICE p–p measurements are valuable for providing asymptotic high-energy limits to (anti)nuclei production models [165], NA61/SHINE can measure these correlations at energies much closer to the (anti)nuclei production threshold. Results at lower energies are most relevant for cosmic antinuclei searches, and can potentially be quite different from the high-energy limit. Future results from NA61/SHINE can be used to compare to high-energy scans at ALICE, as well as to tune hadronic generator models.

5.2 NA61/SHINE Future Upgrades and Future Ultra-high Statistics Data

Along with the measurement of particle production at 158 GeV/c presented in this dissertation, NA61/SHINE has also recorded 10 million p–p collision data sets at 400 GeV/c. Like the 158 GeV/c data, the 400 GeV/c measurements can fill an essential gap, especially for antiprotons and antideuterons. Their analysis will help in further constraining nuclear production models in the most critical range for antinuclei production in cosmic-ray interactions. Although the current 400 GeV/c p–p data set recorded in NA61/SHINE is smaller than the high-statistics 158 GeV/c p–p data sets, a similar overall antideuteron production of ~50 is expected at this energy as well [92, 93].

The identification of antideuteron candidates in existing data also motivates continued measurements with the upgraded NA61/SHINE detector. During the CERN Long Shutdown 2, significant improvements to TPC backend electronics resulted in a reduction of noise and a factor of ~2 improvement in the dE/dx resolution. The replacement of the readout electronics increased the data-taking rate to 2 kHz (~20× faster). New TOF detectors with $\sigma_t = 50\,ps$ [212, 219] were installed, and additional detectors increased the acceptance for highly forward-boosted tracks. Therefore, NA61/SHINE can be used in the future to conduct more studies to reduce systematic uncertainties for cosmic-ray interpretation. Based on the data-taking rate for the first runs in 2022 with the upgraded detector, it becomes possible to collect ~1 billion p–p collisions over ~3 months of data-taking. Such a data set can be recorded possibly before the next Long Shutdown 3, which will start in 2026. It will exceed the current high-statistics data by more than an order of magnitude. With ultra-high p–p statistics in the ~100 GeV/c range, and significantly reduced systematic errors, detailed studies of light antinuclei, which have never been possible before, can be performed in the most relevant energy range for cosmic rays.

Chapter 6
Summary

The detection of cosmic-ray antinuclei represents a potential breakthrough approach for the identification of dark matter. This is because the predicted antinuclei flux at kinetic energies below approximately 1 GeV from a broad range of dark matter models is several orders of magnitude larger than the astrophysical antinuclei background prediction. Moreover, the astrophysical production has a different spectral shape due to the underlying kinematics. The dominant source of antinuclei in the astrophysical background are proton–proton interactions. The two most common models to describe light (anti)nuclei production in such interactions are the thermal and coalescence models, but they are based on different underlying physics. Hence, enhancing our understanding of (anti)nuclei formation mechanism is vital. Typically, modeling light antinuclei production requires $\overline{p}$ production cross sections as input. However, much of the $\overline{p}$ data used for developing (anti)nuclei formation models dates back several decades. Therefore, new precision measurements from modern experiments are crucial to distinguish between the predictions made by the two formation models. This highlights the important of this study, which aims to improve the modeling of (anti)nuclei formation while also measuring (anti)nuclei production using experimental data from contemporary experiments. This study's contributions will enhance our understanding of antinuclei production mechanisms in cosmic rays, and ultimately help in the search for dark matter.

To model the astrophysical antinuclei background, a multiparticle coalescence model was developed to predict the production of antinuclei in cosmic-ray interactions with the interstellar medium. The new model was employed in a large-scale simulation of approximately 100 trillion proton–proton collisions at different collision energies, simulating the energy spectra of cosmic-ray protons. The simulation was used to calculate differential production cross sections of $\overline{p}$, $\overline{d}$, antitriton, $^3\overline{\mathrm{He}}$, and for the first time, $^4\overline{\mathrm{He}}$, as a function of kinetic energy. This model was successfully validated for light antinuclei production in proton–proton collisions at LHC energies of $\sqrt{s} =$ 7 and 13 TeV by comparing it with the most recent data from ALICE. It was also validated for $^3\overline{\mathrm{He}}$ and antitriton production in p–Be and p–Al collisions at $\sqrt{s} =$ 19.4 GeV. Consequently, this model was proved successful in describing the formation

of light antinuclei in a variety of systems across a wide range of energies, using a single energy-dependent coalescence parametrization.

This study marks the first instance of successfully simulating a sufficient number of p–p collisions to generate $^4\overline{\mathrm{He}}$ spectra using the coalescence model approach. Because of the lack of experimental measurements of $^4\overline{\mathrm{He}}$ production, the validity of this model could not be evaluated for this regime. However, the predicted $^4\overline{\mathrm{He}}$ spectra as a function of p_{T} at collision energies of $\sqrt{s} = 7$ and 13 TeV can be compared to data from future collider experiments like ALICE when they become available. These comparisons would be necessary to validate or further refine the model.

Using the new antinuclei production cross sections as input, a Galactic cosmic-ray propagation model was employed to predict the top-of-the-atmosphere astrophysical antinuclei fluxes. These fluxes were compared to studies that relied on a simpler methodology for estimating the production cross sections of heavier antinuclei, which involved scaling the $\overline{p}$ cross section parametrizations. This comparison helped to evaluate the performance of the new model and understand the differences between the predictions made by the two approaches. Notably, the new model predicted antideuteron and antihelium fluxes that were about an order of magnitude lower than the numerical scaling models. In light of the AMS-02 antihelium candidate events, this result reinforces the prediction of extremely low antinuclei backgrounds for cosmic rays at low energies below approximately 1 GeV.

The multiparticle coalescence model was also compared to a semi-classical coalescence model, revealing differences in their predictions of up to an order of magnitude at low energies. A significant contributor to this disparity is the absence of precise antinuclei measurements at these low energies. However, despite such large differences, it was found that the uncertainty in the underlying modeling of antinuclei formation mechanisms exceeds the uncertainty in the determination of coalescence parameters within any given coalescence model. This underscores the critical requirement of more measurements of $\overline{p}$ and $\overline{d}$ production cross sections in p–p and p–He collisions to tune hadronic event generators and improve antinuclei formation modeling.

The lack of high-precision proton-proton experimental data at low energies remains a crucial gap affecting the antinuclei formation modeling and, as a result, the predictions of cosmic-ray backgrounds. Uncertainties in the measured antinuclei production cross sections, as well as in the modeling of antinuclei formation mechanisms, hinder the interpretation of cosmic-ray data. The fixed-target experiment NA61/SHINE at the Super Proton Synchrotron facility at CERN is ideally suited to address this issue, as it can study the collision of protons beams with different targets over an incident beam momentum range of 9–400 GeV/c. To reduce these uncertainties in proton–proton interactions, this study conducted two different types of analyses on the latest high-statistics p–p data sets recorded at NA61/SHINE.

The first analysis in this study measured the spectra of p, $\bar{\text{p}}$, π^+, π^-, K^+, and K^- produced in inelastic p–p interactions with the NA61/SHINE spectrometer at beam momenta of 158 GeV/c . A probability-based particle identification technique was employed, which relied on the energy loss $\text{d}E/\text{d}x$ in the TPCs. Systematic and statistical error were evaluated, and it was found that these new measurements had significantly lower statistical errors because of the ~15 times larger statistics used for this analysis. The phase space coverage of the measured hadron spectra as a function of rapidity and transverse momentum was substantially improved. Furthermore, the antiproton differential production cross section as a function of kinetic energy was also presented for p–p interactions at 158 GeV/c. It was shown that `EPOS-LHC` overpredicts the measurement by ~10–20%, particularly at low kinetic energies with the highest $\bar{p}$ production, as well as in the high y, p_T regime. These new measurements are crucial for refining antiproton production parametrizations used in cosmic-ray modeling. They can also assist in the further improvement of hadronic generator models and help constrain the astrophysical production mechanism of antinuclei within our Galaxy.

Deuterons are produced much more frequently than antideuterons in low-energy p–p interactions close to their production thresholds. Gaining an understanding of deuteron production via the coalescence mechanism can be a crucial first step towards understanding how CR antinuclei are produced. In the second analysis, $\text{d}E/\text{d}x$ measurements were combined with additional m^2 measurements from the ToF detectors. This allowed for the measurement of deuteron production for the first time in proton–proton interactions at energies close to the deuteron production threshold. Extensive deuteron production simulations and comprehensive detector cross checks were conducted to validate the measured deuteron signal and rule out instrumental origin. This work paves the way for future detailed measurements of the deuteron differential production cross sections. Following the success of the deuteron yield measurement with the p–p 158 GeV/c data, the tof–$\text{d}E/\text{d}x$ analysis was also employed to analyze negatively charged tracks. Approximately $5 \cdot 10^4$ antiprotons were identified, suggesting an expectation of about 50 antideuterons in the existing p–p 158 GeV/c data.

The identification of antideuteron candidates in existing data motivates further measurements with the upgraded NA61/SHINE detector. Upcoming measurements at NA61/SHINE include angular correlation studies in the high-statistics p–p data sets and the analysis of p–p 400 GeV/c data. Additionally, with the enhanced data acquisition rate, preparations are underway for ultra-high statistics p–p data sets featuring approximately one billion collision events. Such a data set, intended for measuring antideuteron production cross sections, will enable detailed studies of light (anti)nuclei production in the most relevant range for cosmic rays (p_{lab} ~100 GeV/c), which have never been possible before. This might even include the first potential measurement of antihelium production in p–p interactions close to the production threshold.

Ultimately, these measurements can contribute to the development of a data-driven quantum-mechanical coalescence model to describe the (anti)nuclei formation process. This would complete our understanding of the underlying physics involved in antinuclei production and ultimately provide more precise constraints on dark matter models and astrophysical processes. The improved understanding of antinuclei production would also enhance our ability to interpret cosmic-ray data, potentially leading to breakthroughs in the identification of dark matter signatures and insights into the nature of dark matter itself.

List of Abbreviations

ADC	Analog to Digital Converter
ALICE	A Large Ion Collider Experiment
BPD	Beam Position Detector
CEDAR	Cherenkov Differential Counter with Achromatic Ring Focus
CERN	European Organization for Nuclear Research
CMB	Cosmic Microwave Background
CR	Cosmic Rays
CRMC	Cosmic Ray Monte Carlo software package
GTPC	Gap Time Projection Chamber
ISM	Interstellar medium
LHC	Large Hadron Collider
LHT	Liquid Hydrogen Target
MC	Monte-Carlo Simulation
MIP	Minimum Ionization Particle
MTPC	Main Time Projection Chamber
MWPC	Multi-Wire Proportional Chamber
NA61/SHINE	North Area 61 / SPS Heavy Ion and Neutrino Experiment
PDG	Particle Data Group
PID	Particle Identification
PSET	Particle-Set Identification method
PMT	Photomultiplier Tube

PSD	Projectile Spectator Detector
QCD	Quantum Chromodynamics
QDC	Charge to Digital Converter
QGP	Quark-Gluon Plasma
RST	Right Side Tracks
RTW	Right Target Window
SM	Standard Model of particle physics
SPS	Super Proton Synchrotron
TDC	Time to Digital Converter
THC	Threshold Counter
ToF	Time of Flight detector
tof	time of flight measurement
ToF-F	Forward Time of Flight detector
ToF-L	Left Time of Flight detector
ToF-R	Right Time of Flight detector
ToA	Top of the Atmosphere
TPC	Time Projection Chamber
VTPC	Vertex Time Projection Chamber
WFA	Wave Form Analyzer
WIMP	Weakly Interacting Massive Particle
WST	Wrong Side Tracks

Appendix A

A.1 Tabulated Results

This appendix presents numerical results of the $\mathrm{d}E/\mathrm{d}x$ analysis described in Sec. 4.4. The measured double differential particle spectra of p, $\overline{\mathrm{p}}$, π^+, π^-, K^+, and K^-, produced in inelastic p–p interactions at $p_{\mathrm{beam}} = 158\,\mathrm{GeV}/c$ are provided as a function of transverse momentum (p_{T}) and center-of-mass rapidity (y). These spectra were shown in Fig. 4.20. The values in the tables have the following form:

$$\frac{\mathrm{d}^2 n}{\mathrm{d}y\mathrm{d}p_T} \pm \sigma_{stat} \pm {}^{\sigma_{sys\,+}}_{\sigma_{sys\,-}}, \tag{A.1}$$

where $\frac{\mathrm{d}^2 n}{\mathrm{d}y\mathrm{d}p_T}$ $(\mathrm{GeV}/c)^{-1}$ is the mean number of particles produced per p–p event per unit volume of the y–p_T phase space. σ_{stat} denotes statistical uncertainties, and $\sigma_{sys\,\pm}$ are the upper and lower limits of the systematic uncertainties.

Table A.1: Proton $\frac{\mathrm{d}^2 n}{\mathrm{d}y\mathrm{d}p_T}$ spectra

y	p_T (GeV/c)				
	0.1	0.2	0.3	0.4	0.5
0.1	$0.0191 \pm 0.0003\ ^{+0.0019}_{-0.0025}$	$0.0537 \pm 0.0005\ ^{+0.0058}_{-0.0068}$	$0.0791 \pm 0.0006\ ^{+0.0055}_{-0.0094}$	$0.0946 \pm 0.0007\ ^{+0.0052}_{-0.0104}$	$0.0920 \pm 0.0007\ ^{+0.0000}_{-0.0093}$
0.3	$0.0206 \pm 0.0003\ ^{+0.0000}_{-0.0026}$	$0.0573 \pm 0.0005\ ^{+0.0035}_{-0.0069}$	$0.0835 \pm 0.0006\ ^{+0.0013}_{-0.0084}$	$0.0986 \pm 0.0007\ ^{+0.0055}_{-0.0106}$	$0.0990 \pm 0.0007\ ^{+0.0033}_{-0.0100}$
0.5	$0.0210 \pm 0.0003\ ^{+0.0000}_{-0.0025}$	$0.0601 \pm 0.0005\ ^{+0.0036}_{-0.0069}$	$0.0886 \pm 0.0006\ ^{+0.0055}_{-0.0051}$	$0.1047 \pm 0.0007\ ^{+0.0059}_{-0.0108}$	$0.1060 \pm 0.0007\ ^{+0.0058}_{-0.0105}$
0.7	$0.0252 \pm 0.0003\ ^{+0.0012}_{-0.0027}$	$0.0683 \pm 0.0006\ ^{+0.0035}_{-0.0039}$	$0.0983 \pm 0.0007\ ^{+0.0103}_{-0.0054}$	$0.1158 \pm 0.0007\ ^{+0.0067}_{-0.0106}$	$0.1164 \pm 0.0008\ ^{+0.0067}_{-0.0087}$
0.9	$0.0329 \pm 0.0004\ ^{+0.0027}_{-0.0005}$	$0.0884 \pm 0.0006\ ^{+0.0077}_{-0.0026}$	$0.1247 \pm 0.0008\ ^{+0.0079}_{-0.0056}$	$0.1401 \pm 0.0008\ ^{+0.0082}_{-0.0062}$	$0.1368 \pm 0.0008\ ^{+0.0072}_{-0.0046}$
1.1	$0.0368 \pm 0.0004\ ^{+0.0030}_{-0.0005}$	$0.1020 \pm 0.0007\ ^{+0.0086}_{-0.0008}$	$0.1475 \pm 0.0008\ ^{+0.0030}_{-0.0094}$	$0.1687 \pm 0.0009\ ^{+0.0022}_{-0.0113}$	$0.1595 \pm 0.0009\ ^{+0.0061}_{-0.0071}$
1.3	$0.0473 \pm 0.0005\ ^{+0.0034}_{-0.0014}$	$0.1314 \pm 0.0008\ ^{+0.0103}_{-0.0021}$	$0.1893 \pm 0.0010\ ^{+0.0104}_{-0.0070}$	$0.2135 \pm 0.0010\ ^{+0.0128}_{-0.0057}$	$0.2096 \pm 0.0010\ ^{+0.0147}_{-0.0037}$
1.5	$0.0559 \pm 0.0005\ ^{+0.0029}_{-0.0029}$	$0.1647 \pm 0.0009\ ^{+0.0088}_{-0.0069}$	$0.2417 \pm 0.0011\ ^{+0.0113}_{-0.0099}$	$0.2801 \pm 0.0012\ ^{+0.0096}_{-0.0092}$	$0.2752 \pm 0.0012\ ^{+0.0169}_{-0.0085}$
1.7	$0.0644 \pm 0.0005\ ^{+0.0024}_{-0.0045}$	$0.1846 \pm 0.0009\ ^{+0.0062}_{-0.0111}$	$0.2841 \pm 0.0012\ ^{+0.0112}_{-0.0126}$	$0.3505 \pm 0.0014\ ^{+0.0083}_{-0.0155}$	$0.3647 \pm 0.0014\ ^{+0.0180}_{-0.0097}$
1.9	$0.0796 \pm 0.0006\ ^{+0.0026}_{-0.0047}$	$0.2259 \pm 0.0011\ ^{+0.0069}_{-0.0120}$	$0.3338 \pm 0.0013\ ^{+0.0162}_{-0.0080}$	$0.3883 \pm 0.0014\ ^{+0.0115}_{-0.0141}$	$0.3912 \pm 0.0014\ ^{+0.0154}_{-0.0073}$

y	p_T (GeV/c)				
	0.6	0.7	0.8	0.9	1.0
0.1	$0.0851 \pm 0.0007\ ^{+0.0005}_{-0.0075}$	$0.0721 \pm 0.0007\ ^{+0.0032}_{-0.0062}$	$0.0620 \pm 0.0006\ ^{+0.0043}_{-0.0028}$	$0.0499 \pm 0.0006\ ^{+0.0027}_{-0.0032}$	$0.0378 \pm 0.0005\ ^{+0.0016}_{-0.0013}$
0.3	$0.0898 \pm 0.0007\ ^{+0.0040}_{-0.0084}$	$0.0711 \pm 0.0006\ ^{+0.0033}_{-0.0035}$	$0.0578 \pm 0.0006\ ^{+0.0029}_{-0.0030}$	$0.0451 \pm 0.0005\ ^{+0.0027}_{-0.0030}$	$0.0351 \pm 0.0005\ ^{+0.0025}_{-0.0014}$
0.5	$0.0950 \pm 0.0007\ ^{+0.0073}_{-0.0058}$	$0.0821 \pm 0.0007\ ^{+0.0064}_{-0.0034}$	$0.0627 \pm 0.0006\ ^{+0.0051}_{-0.0026}$	$0.0471 \pm 0.0005\ ^{+0.0021}_{-0.0019}$	$0.0341 \pm 0.0004\ ^{+0.0019}_{-0.0017}$
0.7	$0.1066 \pm 0.0007\ ^{+0.0075}_{-0.0039}$	$0.0915 \pm 0.0007\ ^{+0.0054}_{-0.0029}$	$0.0713 \pm 0.0006\ ^{+0.0037}_{-0.0022}$	$0.0527 \pm 0.0005\ ^{+0.0023}_{-0.0023}$	$0.0400 \pm 0.0005\ ^{+0.0015}_{-0.0025}$
0.9	$0.1223 \pm 0.0008\ ^{+0.0056}_{-0.0046}$	$0.1029 \pm 0.0007\ ^{+0.0042}_{-0.0040}$	$0.0814 \pm 0.0007\ ^{+0.0011}_{-0.0053}$	$0.0620 \pm 0.0006\ ^{+0.0025}_{-0.0048}$	$0.0451 \pm 0.0005\ ^{+0.0017}_{-0.0034}$
1.1	$0.1462 \pm 0.0009\ ^{+0.0061}_{-0.0060}$	$0.1197 \pm 0.0008\ ^{+0.0065}_{-0.0036}$	$0.0960 \pm 0.0007\ ^{+0.0051}_{-0.0028}$	$0.0733 \pm 0.0006\ ^{+0.0021}_{-0.0051}$	$0.0522 \pm 0.0005\ ^{+0.0016}_{-0.0035}$
1.3	$0.1893 \pm 0.0010\ ^{+0.0102}_{-0.0062}$	$0.1535 \pm 0.0009\ ^{+0.0106}_{-0.0032}$	$0.1201 \pm 0.0008\ ^{+0.0079}_{-0.0031}$	$0.0929 \pm 0.0007\ ^{+0.0044}_{-0.0038}$	$0.0608 \pm 0.0006\ ^{+0.0030}_{-0.0032}$
1.5	$0.2499 \pm 0.0012\ ^{+0.0144}_{-0.0078}$	$0.2043 \pm 0.0011\ ^{+0.0110}_{-0.0064}$	$0.1592 \pm 0.0009\ ^{+0.0072}_{-0.0046}$	$0.1202 \pm 0.0008\ ^{+0.0039}_{-0.0031}$	$0.0840 \pm 0.0007\ ^{+0.0002}_{-0.0038}$
1.7	$0.3376 \pm 0.0014\ ^{+0.0097}_{-0.0153}$	$0.2837 \pm 0.0013\ ^{+0.0069}_{-0.0067}$	$0.2136 \pm 0.0011\ ^{+0.0050}_{-0.0062}$	$0.1557 \pm 0.0010\ ^{+0.0030}_{-0.0037}$	$0.1053 \pm 0.0008\ ^{+0.0013}_{-0.0043}$
1.9	$0.3582 \pm 0.0014\ ^{+0.0116}_{-0.0078}$	$0.3022 \pm 0.0013\ ^{+0.0046}_{-0.0116}$	$0.2313 \pm 0.0011\ ^{+0.0034}_{-0.0085}$	$0.1626 \pm 0.0009\ ^{+0.0017}_{-0.0044}$	$0.1097 \pm 0.0008\ ^{+0.0013}_{-0.0029}$

y	p_T (GeV/c)				
	1.1	1.2	1.3	1.4	1.5
0.1	$0.0262 \pm 0.0005\ ^{+0.0010}_{-0.0021}$	$0.0190 \pm 0.0004\ ^{+0.0009}_{-0.0013}$	$0.0140 \pm 0.0003\ ^{+0.0005}_{-0.0008}$	$0.0098 \pm 0.0003\ ^{+0.0002}_{-0.0006}$	$0.0073 \pm 0.0003\ ^{+0.0005}_{-0.0000}$
0.3	$0.0253 \pm 0.0004\ ^{+0.0010}_{-0.0019}$	$0.0172 \pm 0.0003\ ^{+0.0015}_{-0.0009}$	$0.0119 \pm 0.0003\ ^{+0.0005}_{-0.0008}$	$0.0088 \pm 0.0003\ ^{+0.0001}_{-0.0007}$	$0.0059 \pm 0.0002\ ^{+0.0001}_{-0.0004}$
0.5	$0.0247 \pm 0.0004\ ^{+0.0011}_{-0.0011}$	$0.0176 \pm 0.0003\ ^{+0.0013}_{-0.0002}$	$0.0118 \pm 0.0003\ ^{+0.0007}_{-0.0009}$	$0.0078 \pm 0.0002\ ^{+0.0003}_{-0.0005}$	$0.0062 \pm 0.0002\ ^{+0.0003}_{-0.0005}$
0.7	$0.0282 \pm 0.0004\ ^{+0.0017}_{-0.0014}$	$0.0185 \pm 0.0003\ ^{+0.0008}_{-0.0015}$	$0.0131 \pm 0.0003\ ^{+0.0008}_{-0.0007}$	$0.0090 \pm 0.0002\ ^{+0.0005}_{-0.0002}$	$0.0059 \pm 0.0002\ ^{+0.0003}_{-0.0004}$
0.9	$0.0310 \pm 0.0004\ ^{+0.0015}_{-0.0020}$	$0.0217 \pm 0.0004\ ^{+0.0004}_{-0.0017}$	$0.0154 \pm 0.0003\ ^{+0.0005}_{-0.0010}$	$0.0099 \pm 0.0002\ ^{+0.0004}_{-0.0004}$	$0.0069 \pm 0.0002\ ^{+0.0002}_{-0.0004}$
1.1	$0.0358 \pm 0.0005\ ^{+0.0013}_{-0.0023}$	$0.0255 \pm 0.0004\ ^{+0.0009}_{-0.0014}$	$0.0177 \pm 0.0003\ ^{+0.0002}_{-0.0009}$	$0.0110 \pm 0.0003\ ^{+0.0005}_{-0.0003}$	$0.0074 \pm 0.0002\ ^{+0.0001}_{-0.0005}$
1.3	$0.0438 \pm 0.0005\ ^{+0.0017}_{-0.0022}$	$0.0295 \pm 0.0004\ ^{+0.0007}_{-0.0014}$	$0.0192 \pm 0.0003\ ^{+0.0004}_{-0.0010}$	$0.0124 \pm 0.0003\ ^{+0.0002}_{-0.0007}$	$0.0077 \pm 0.0002\ ^{+0.0001}_{-0.0005}$
1.5	$0.0536 \pm 0.0006\ ^{+0.0011}_{-0.0024}$	$0.0348 \pm 0.0004\ ^{+0.0003}_{-0.0015}$	$0.0217 \pm 0.0003\ ^{+0.0004}_{-0.0008}$	$0.0130 \pm 0.0003\ ^{+0.0002}_{-0.0005}$	$0.0082 \pm 0.0002\ ^{+0.0003}_{-0.0004}$
1.7	$0.0679 \pm 0.0006\ ^{+0.0011}_{-0.0027}$	$0.0414 \pm 0.0005\ ^{+0.0006}_{-0.0015}$	$0.0248 \pm 0.0004\ ^{+0.0004}_{-0.0006}$	$0.0139 \pm 0.0003\ ^{+0.0002}_{-0.0004}$	$0.0079 \pm 0.0002\ ^{+0.0002}_{-0.0002}$
1.9	$0.0685 \pm 0.0006\ ^{+0.0011}_{-0.0019}$	$0.0372 \pm 0.0005\ ^{+0.0004}_{-0.0007}$	$0.0171 \pm 0.0003\ ^{+0.0003}_{-0.0005}$	$0.0061 \pm 0.0002\ ^{+0.0001}_{-0.0002}$	$0.0016 \pm 0.0001\ ^{+0.0000}_{-0.0000}$

Table A.2: Antiproton $\frac{\mathrm{d}^2 n}{\mathrm{d}y \mathrm{d}p_T}$ spectra

y	p_T (GeV/c)				
	0.1	0.2	0.3	0.4	0.5
0.1	$0.0050 \pm 0.0001\ ^{+0.0007}_{-0.0006}$	$0.0144 \pm 0.0002\ ^{+0.0029}_{-0.0016}$	$0.0210 \pm 0.0003\ ^{+0.0040}_{-0.0036}$	$0.0238 \pm 0.0003\ ^{+0.0028}_{-0.0040}$	$0.0245 \pm 0.0003\ ^{+0.0020}_{-0.0037}$
0.3	$0.0052 \pm 0.0002\ ^{+0.0010}_{-0.0008}$	$0.0137 \pm 0.0002\ ^{+0.0026}_{-0.0014}$	$0.0205 \pm 0.0003\ ^{+0.0034}_{-0.0030}$	$0.0232 \pm 0.0003\ ^{+0.0031}_{-0.0039}$	$0.0228 \pm 0.0003\ ^{+0.0016}_{-0.0037}$
0.5	$0.0047 \pm 0.0001\ ^{+0.0009}_{-0.0000}$	$0.0129 \pm 0.0002\ ^{+0.0015}_{-0.0010}$	$0.0187 \pm 0.0003\ ^{+0.0021}_{-0.0017}$	$0.0219 \pm 0.0003\ ^{+0.0019}_{-0.0031}$	$0.0214 \pm 0.0003\ ^{+0.0019}_{-0.0026}$
0.7	$0.0045 \pm 0.0001\ ^{+0.0009}_{-0.0005}$	$0.0119 \pm 0.0002\ ^{+0.0014}_{-0.0021}$	$0.0171 \pm 0.0003\ ^{+0.0020}_{-0.0031}$	$0.0194 \pm 0.0003\ ^{+0.0020}_{-0.0016}$	$0.0188 \pm 0.0003\ ^{+0.0025}_{-0.0015}$
0.9	$0.0044 \pm 0.0001\ ^{+0.0006}_{-0.0003}$	$0.0118 \pm 0.0002\ ^{+0.0023}_{-0.0013}$	$0.0160 \pm 0.0003\ ^{+0.0014}_{-0.0028}$	$0.0173 \pm 0.0003\ ^{+0.0015}_{-0.0019}$	$0.0156 \pm 0.0003\ ^{+0.0028}_{-0.0013}$
1.1	$0.0030 \pm 0.0001\ ^{+0.0006}_{-0.0001}$	$0.0083 \pm 0.0002\ ^{+0.0006}_{-0.0013}$	$0.0125 \pm 0.0002\ ^{+0.0002}_{-0.0023}$	$0.0134 \pm 0.0003\ ^{+0.0000}_{-0.0024}$	$0.0119 \pm 0.0002\ ^{+0.0014}_{-0.0011}$
1.3	$0.0021 \pm 0.0001\ ^{+0.0005}_{-0.0000}$	$0.0057 \pm 0.0002\ ^{+0.0008}_{-0.0006}$	$0.0085 \pm 0.0002\ ^{+0.0013}_{-0.0008}$	$0.0091 \pm 0.0002\ ^{+0.0018}_{-0.0006}$	$0.0084 \pm 0.0002\ ^{+0.0020}_{-0.0003}$
1.5	$0.0015 \pm 0.0001\ ^{+0.0004}_{-0.0001}$	$0.0037 \pm 0.0001\ ^{+0.0009}_{-0.0003}$	$0.0052 \pm 0.0002\ ^{+0.0012}_{-0.0004}$	$0.0055 \pm 0.0002\ ^{+0.0007}_{-0.0008}$	$0.0052 \pm 0.0002\ ^{+0.0009}_{-0.0004}$
1.7	$0.0009 \pm 0.0001\ ^{+0.0003}_{-0.0002}$	$0.0021 \pm 0.0001\ ^{+0.0005}_{-0.0004}$	$0.0029 \pm 0.0001\ ^{+0.0007}_{-0.0004}$	$0.0029 \pm 0.0001\ ^{+0.0004}_{-0.0006}$	$0.0029 \pm 0.0001\ ^{+0.0008}_{-0.0004}$
1.9	$0.0004 \pm 0.0000\ ^{+0.0001}_{-0.0001}$	$0.0011 \pm 0.0001\ ^{+0.0004}_{-0.0003}$	$0.0015 \pm 0.0001\ ^{+0.0005}_{-0.0002}$	$0.0014 \pm 0.0001\ ^{+0.0003}_{-0.0003}$	$0.0014 \pm 0.0001\ ^{+0.0004}_{-0.0002}$

y	p_T (GeV/c)				
	0.6	0.7	0.8	0.9	1.0
0.1	$0.0221 \pm 0.0003\ ^{+0.0033}_{-0.0001}$	$0.0162 \pm 0.0003\ ^{+0.0021}_{-0.0012}$	$0.0129 \pm 0.0003\ ^{+0.0014}_{-0.0011}$	$0.0102 \pm 0.0003\ ^{+0.0003}_{-0.0013}$	$0.0071 \pm 0.0002\ ^{+0.0010}_{-0.0009}$
0.3	$0.0203 \pm 0.0003\ ^{+0.0017}_{-0.0026}$	$0.0156 \pm 0.0003\ ^{+0.0011}_{-0.0023}$	$0.0116 \pm 0.0002\ ^{+0.0017}_{-0.0003}$	$0.0083 \pm 0.0002\ ^{+0.0007}_{-0.0006}$	$0.0058 \pm 0.0002\ ^{+0.0009}_{-0.0005}$
0.5	$0.0187 \pm 0.0003\ ^{+0.0027}_{-0.0018}$	$0.0150 \pm 0.0003\ ^{+0.0011}_{-0.0023}$	$0.0104 \pm 0.0002\ ^{+0.0008}_{-0.0010}$	$0.0069 \pm 0.0002\ ^{+0.0011}_{-0.0002}$	$0.0049 \pm 0.0002\ ^{+0.0008}_{-0.0006}$
0.7	$0.0169 \pm 0.0003\ ^{+0.0030}_{-0.0013}$	$0.0135 \pm 0.0003\ ^{+0.0021}_{-0.0013}$	$0.0099 \pm 0.0002\ ^{+0.0017}_{-0.0008}$	$0.0063 \pm 0.0002\ ^{+0.0010}_{-0.0006}$	$0.0045 \pm 0.0002\ ^{+0.0006}_{-0.0007}$
0.9	$0.0135 \pm 0.0003\ ^{+0.0016}_{-0.0016}$	$0.0105 \pm 0.0002\ ^{+0.0014}_{-0.0009}$	$0.0079 \pm 0.0002\ ^{+0.0009}_{-0.0006}$	$0.0053 \pm 0.0002\ ^{+0.0001}_{-0.0009}$	$0.0034 \pm 0.0001\ ^{+0.0003}_{-0.0006}$
1.1	$0.0098 \pm 0.0002\ ^{+0.0002}_{-0.0017}$	$0.0075 \pm 0.0002\ ^{+0.0012}_{-0.0005}$	$0.0054 \pm 0.0002\ ^{+0.0010}_{-0.0002}$	$0.0039 \pm 0.0001\ ^{+0.0005}_{-0.0007}$	$0.0023 \pm 0.0001\ ^{+0.0003}_{-0.0004}$
1.3	$0.0070 \pm 0.0002\ ^{+0.0009}_{-0.0009}$	$0.0047 \pm 0.0002\ ^{+0.0012}_{-0.0002}$	$0.0035 \pm 0.0001\ ^{+0.0009}_{-0.0002}$	$0.0029 \pm 0.0001\ ^{+0.0006}_{-0.0003}$	$0.0014 \pm 0.0001\ ^{+0.0001}_{-0.0003}$
1.5	$0.0044 \pm 0.0001\ ^{+0.0012}_{-0.0004}$	$0.0029 \pm 0.0001\ ^{+0.0007}_{-0.0003}$	$0.0021 \pm 0.0001\ ^{+0.0005}_{-0.0002}$	$0.0016 \pm 0.0001\ ^{+0.0003}_{-0.0002}$	$0.0010 \pm 0.0001\ ^{+0.0002}_{-0.0001}$
1.7	$0.0023 \pm 0.0001\ ^{+0.0007}_{-0.0004}$	$0.0016 \pm 0.0001\ ^{+0.0001}_{-0.0004}$	$0.0011 \pm 0.0001\ ^{+0.0002}_{-0.0002}$	$0.0007 \pm 0.0001\ ^{+0.0001}_{-0.0001}$	$0.0004 \pm 0.0000\ ^{+0.0001}_{-0.0001}$
1.9	$0.0010 \pm 0.0001\ ^{+0.0003}_{-0.0001}$	$0.0008 \pm 0.0001\ ^{+0.0002}_{-0.0001}$	$0.0005 \pm 0.0001\ ^{+0.0002}_{-0.0001}$	$0.0003 \pm 0.0000\ ^{+0.0000}_{-0.0001}$	—

y	p_T (GeV/c)				
	1.1	1.2	1.3	1.4	1.5
0.1	$0.0044 \pm 0.0002\ ^{+0.0002}_{-0.0004}$	$0.0028 \pm 0.0001\ ^{+0.0002}_{-0.0003}$	$0.0020 \pm 0.0001\ ^{+0.0002}_{-0.0001}$	$0.0013 \pm 0.0001\ ^{+0.0002}_{-0.0000}$	$0.0009 \pm 0.0001\ ^{+0.0001}_{-0.0001}$
0.3	$0.0039 \pm 0.0002\ ^{+0.0006}_{-0.0004}$	$0.0026 \pm 0.0001\ ^{+0.0002}_{-0.0004}$	$0.0014 \pm 0.0001\ ^{+0.0002}_{-0.0001}$	$0.0010 \pm 0.0001\ ^{+0.0001}_{-0.0001}$	$0.0006 \pm 0.0001\ ^{+0.0001}_{-0.0000}$
0.5	$0.0030 \pm 0.0001\ ^{+0.0006}_{-0.0005}$	$0.0022 \pm 0.0001\ ^{+0.0004}_{-0.0003}$	$0.0012 \pm 0.0001\ ^{+0.0002}_{-0.0001}$	$0.0008 \pm 0.0001\ ^{+0.0001}_{-0.0001}$	$0.0006 \pm 0.0001\ ^{+0.0001}_{-0.0000}$
0.7	$0.0028 \pm 0.0001\ ^{+0.0004}_{-0.0004}$	$0.0017 \pm 0.0001\ ^{+0.0000}_{-0.0003}$	$0.0012 \pm 0.0001\ ^{+0.0002}_{-0.0001}$	$0.0007 \pm 0.0001\ ^{+0.0001}_{-0.0001}$	$0.0004 \pm 0.0000\ ^{+0.0001}_{-0.0000}$
0.9	$0.0022 \pm 0.0001\ ^{+0.0003}_{-0.0004}$	$0.0014 \pm 0.0001\ ^{+0.0002}_{-0.0002}$	$0.0009 \pm 0.0001\ ^{+0.0000}_{-0.0002}$	$0.0004 \pm 0.0000\ ^{+0.0001}_{-0.0000}$	$0.0003 \pm 0.0000\ ^{+0.0000}_{-0.0000}$
1.1	$0.0014 \pm 0.0001\ ^{+0.0002}_{-0.0002}$	$0.0010 \pm 0.0001\ ^{+0.0001}_{-0.0002}$	$0.0005 \pm 0.0001\ ^{+0.0000}_{-0.0001}$	$0.0003 \pm 0.0000\ ^{+0.0001}_{-0.0000}$	$0.0002 \pm 0.0000\ ^{+0.0000}_{-0.0000}$
1.3	$0.0009 \pm 0.0001\ ^{+0.0002}_{-0.0001}$	$0.0005 \pm 0.0001\ ^{+0.0001}_{-0.0001}$	$0.0003 \pm 0.0000\ ^{+0.0000}_{-0.0000}$	$0.0001 \pm 0.0000\ ^{+0.0000}_{-0.0000}$	$0.0001 \pm 0.0000\ ^{+0.0000}_{-0.0000}$
1.5	$0.0005 \pm 0.0000\ ^{+0.0001}_{-0.0000}$	$0.0003 \pm 0.0000\ ^{+0.0000}_{-0.0001}$	$0.0002 \pm 0.0000\ ^{+0.0000}_{-0.0000}$	$0.0001 \pm 0.0000\ ^{+0.0000}_{-0.0000}$	$0.0001 \pm 0.0000\ ^{+0.0000}_{-0.0000}$
1.7	$0.0003 \pm 0.0000\ ^{+0.0000}_{-0.0001}$	$0.0001 \pm 0.0000\ ^{+0.0000}_{-0.0000}$	$0.0001 \pm 0.0000\ ^{+0.0000}_{-0.0000}$	—	—
1.9	—	—	—	—	—

Table A.3: π^+ $\frac{\mathrm{d}^2n}{\mathrm{d}y\mathrm{d}p_T}$ spectra

y	p_T (GeV/c)				
	0.1	0.2	0.3	0.4	0.5
0.1	—	—	—	—	$0.8520 \pm 0.0023\ ^{+0.0110}_{-0.0092}$
0.3	—	—	—	$1.1633 \pm 0.0026\ ^{+0.0159}_{-0.0040}$	$0.8663 \pm 0.0023\ ^{+0.0076}_{-0.0137}$
0.5	—	—	$1.1522 \pm 0.0025\ ^{+0.0086}_{-0.0065}$	$1.2167 \pm 0.0027\ ^{+0.0137}_{-0.0163}$	$0.8642 \pm 0.0023\ ^{+0.0123}_{-0.0049}$
0.7	—	—	$1.4580 \pm 0.0029\ ^{+0.0090}_{-0.0134}$	$1.1106 \pm 0.0025\ ^{+0.0126}_{-0.0155}$	$0.7734 \pm 0.0021\ ^{+0.0110}_{-0.0005}$
0.9	—	$1.2371 \pm 0.0026\ ^{+0.0071}_{-0.0019}$	$1.4447 \pm 0.0028\ ^{+0.0032}_{-0.0136}$	$1.1234 \pm 0.0025\ ^{+0.0111}_{-0.0085}$	$0.7667 \pm 0.0021\ ^{+0.0102}_{-0.0001}$
1.1	$0.4374 \pm 0.0016\ ^{+0.0026}_{-0.0018}$	$1.3173 \pm 0.0027\ ^{+0.0023}_{-0.0051}$	$1.3851 \pm 0.0028\ ^{+0.0047}_{-0.0122}$	$1.0881 \pm 0.0024\ ^{+0.0104}_{-0.0019}$	$0.7535 \pm 0.0020\ ^{+0.0065}_{-0.0053}$
1.3	$0.5033 \pm 0.0017\ ^{+0.0022}_{-0.0012}$	$1.2404 \pm 0.0026\ ^{+0.0013}_{-0.0083}$	$1.2964 \pm 0.0027\ ^{+0.0086}_{-0.0066}$	$1.0231 \pm 0.0024\ ^{+0.0076}_{-0.0052}$	$0.7197 \pm 0.0020\ ^{+0.0046}_{-0.0085}$
1.5	$0.4476 \pm 0.0016\ ^{+0.0013}_{-0.0013}$	$1.1347 \pm 0.0025\ ^{+0.0037}_{-0.0084}$	$1.2058 \pm 0.0026\ ^{+0.0066}_{-0.0054}$	$0.9504 \pm 0.0023\ ^{+0.0055}_{-0.0098}$	$0.6704 \pm 0.0019\ ^{+0.0050}_{-0.0107}$
1.7	$0.3996 \pm 0.0015\ ^{+0.0012}_{-0.0023}$	$1.0285 \pm 0.0024\ ^{+0.0034}_{-0.0060}$	$1.1045 \pm 0.0025\ ^{+0.0004}_{-0.0143}$	$0.8578 \pm 0.0022\ ^{+0.0088}_{-0.0124}$	$0.6022 \pm 0.0018\ ^{+0.0039}_{-0.0141}$
1.9	$0.3499 \pm 0.0014\ ^{+0.0012}_{-0.0023}$	$0.9105 \pm 0.0022\ ^{+0.0034}_{-0.0052}$	$0.9803 \pm 0.0023\ ^{+0.0018}_{-0.0174}$	$0.7536 \pm 0.0021\ ^{+0.0139}_{-0.0149}$	$0.5229 \pm 0.0017\ ^{+0.0026}_{-0.0173}$
2.1	$0.3096 \pm 0.0013\ ^{+0.0008}_{-0.0011}$	$0.7925 \pm 0.0021\ ^{+0.0040}_{-0.0087}$	$0.8491 \pm 0.0022\ ^{+0.0112}_{-0.0162}$	$0.6461 \pm 0.0019\ ^{+0.0083}_{-0.0141}$	$0.4435 \pm 0.0016\ ^{+0.0084}_{-0.0187}$
2.3	$0.2711 \pm 0.0012\ ^{+0.0015}_{-0.0017}$	$0.6860 \pm 0.0020\ ^{+0.0036}_{-0.0138}$	$0.7247 \pm 0.0020\ ^{+0.0096}_{-0.0137}$	$0.5396 \pm 0.0018\ ^{+0.0099}_{-0.0190}$	$0.3591 \pm 0.0015\ ^{+0.0069}_{-0.0201}$

y	p_T (GeV/c)				
	0.6	0.7	0.8	0.9	1.0
0.1	$0.5791 \pm 0.0019\ ^{+0.0072}_{-0.0109}$	$0.3843 \pm 0.0016\ ^{+0.0073}_{-0.0080}$	$0.2472 \pm 0.0013\ ^{+0.0050}_{-0.0030}$	$0.1624 \pm 0.0011\ ^{+0.0023}_{-0.0045}$	$0.1039 \pm 0.0009\ ^{+0.0024}_{-0.0013}$
0.3	$0.5888 \pm 0.0020\ ^{+0.0104}_{-0.0046}$	$0.3859 \pm 0.0016\ ^{+0.0083}_{-0.0084}$	$0.2509 \pm 0.0014\ ^{+0.0041}_{-0.0067}$	$0.1610 \pm 0.0011\ ^{+0.0009}_{-0.0045}$	$0.1046 \pm 0.0009\ ^{+0.0014}_{-0.0020}$
0.5	$0.5732 \pm 0.0019\ ^{+0.0103}_{-0.0098}$	$0.3735 \pm 0.0016\ ^{+0.0083}_{-0.0089}$	$0.2403 \pm 0.0013\ ^{+0.0011}_{-0.0069}$	$0.1530 \pm 0.0010\ ^{+0.0033}_{-0.0028}$	$0.0964 \pm 0.0008\ ^{+0.0010}_{-0.0024}$
0.7	$0.5145 \pm 0.0018\ ^{+0.0054}_{-0.0070}$	$0.3366 \pm 0.0015\ ^{+0.0043}_{-0.0081}$	$0.2141 \pm 0.0012\ ^{+0.0037}_{-0.0061}$	$0.1401 \pm 0.0010\ ^{+0.0041}_{-0.0010}$	$0.0882 \pm 0.0008\ ^{+0.0003}_{-0.0034}$
0.9	$0.5060 \pm 0.0017\ ^{+0.0039}_{-0.0064}$	$0.3237 \pm 0.0014\ ^{+0.0020}_{-0.0069}$	$0.2057 \pm 0.0011\ ^{+0.0050}_{-0.0031}$	$0.1281 \pm 0.0009\ ^{+0.0038}_{-0.0003}$	$0.0810 \pm 0.0007\ ^{+0.0019}_{-0.0014}$
1.1	$0.4955 \pm 0.0017\ ^{+0.0060}_{-0.0056}$	$0.3150 \pm 0.0013\ ^{+0.0065}_{-0.0041}$	$0.1998 \pm 0.0011\ ^{+0.0030}_{-0.0044}$	$0.1249 \pm 0.0009\ ^{+0.0043}_{-0.0004}$	$0.0770 \pm 0.0007\ ^{+0.0031}_{-0.0007}$
1.3	$0.4744 \pm 0.0016\ ^{+0.0077}_{-0.0063}$	$0.3012 \pm 0.0013\ ^{+0.0032}_{-0.0071}$	$0.1866 \pm 0.0010\ ^{+0.0027}_{-0.0049}$	$0.1147 \pm 0.0008\ ^{+0.0049}_{-0.0011}$	$0.0699 \pm 0.0006\ ^{+0.0033}_{-0.0021}$
1.5	$0.4416 \pm 0.0016\ ^{+0.0037}_{-0.0106}$	$0.2816 \pm 0.0013\ ^{+0.0012}_{-0.0103}$	$0.1719 \pm 0.0010\ ^{+0.0034}_{-0.0063}$	$0.1020 \pm 0.0008\ ^{+0.0050}_{-0.0046}$	$0.0617 \pm 0.0006\ ^{+0.0026}_{-0.0029}$
1.7	$0.4050 \pm 0.0015\ ^{+0.0023}_{-0.0135}$	$0.2559 \pm 0.0012\ ^{+0.0047}_{-0.0115}$	$0.1577 \pm 0.0010\ ^{+0.0037}_{-0.0083}$	$0.0920 \pm 0.0008\ ^{+0.0029}_{-0.0050}$	$0.0519 \pm 0.0006\ ^{+0.0023}_{-0.0021}$
1.9	$0.3563 \pm 0.0014\ ^{+0.0091}_{-0.0118}$	$0.2271 \pm 0.0012\ ^{+0.0045}_{-0.0120}$	$0.1360 \pm 0.0009\ ^{+0.0028}_{-0.0080}$	$0.0781 \pm 0.0007\ ^{+0.0028}_{-0.0038}$	$0.0428 \pm 0.0005\ ^{+0.0042}_{-0.0002}$
2.1	$0.2925 \pm 0.0013\ ^{+0.0062}_{-0.0150}$	$0.1889 \pm 0.0011\ ^{+0.0048}_{-0.0102}$	$0.1093 \pm 0.0009\ ^{+0.0059}_{-0.0045}$	$0.0587 \pm 0.0006\ ^{+0.0033}_{-0.0034}$	$0.0293 \pm 0.0004\ ^{+0.0043}_{-0.0019}$
2.3	$0.2304 \pm 0.0013\ ^{+0.0133}_{-0.0124}$	$0.1380 \pm 0.0010\ ^{+0.0095}_{-0.0067}$	$0.0694 \pm 0.0007\ ^{+0.0097}_{-0.0040}$	$0.0329 \pm 0.0004\ ^{+0.0039}_{-0.0018}$	$0.0148 \pm 0.0003\ ^{+0.0022}_{-0.0011}$

y	p_T (GeV/c)				
	1.1	1.2	1.3	1.4	1.5
0.1	$0.0668 \pm 0.0007\ ^{+0.0003}_{-0.0021}$	$0.0428 \pm 0.0006\ ^{+0.0004}_{-0.0015}$	$0.0276 \pm 0.0005\ ^{+0.0009}_{-0.0008}$	$0.0172 \pm 0.0004\ ^{+0.0005}_{-0.0005}$	$0.0111 \pm 0.0003\ ^{+0.0004}_{-0.0003}$
0.3	$0.0649 \pm 0.0007\ ^{+0.0016}_{-0.0023}$	$0.0426 \pm 0.0006\ ^{+0.0015}_{-0.0015}$	$0.0268 \pm 0.0005\ ^{+0.0009}_{-0.0007}$	$0.0172 \pm 0.0004\ ^{+0.0004}_{-0.0005}$	$0.0114 \pm 0.0003\ ^{+0.0000}_{-0.0005}$
0.5	$0.0600 \pm 0.0007\ ^{+0.0015}_{-0.0022}$	$0.0383 \pm 0.0005\ ^{+0.0010}_{-0.0017}$	$0.0250 \pm 0.0004\ ^{+0.0007}_{-0.0005}$	$0.0154 \pm 0.0003\ ^{+0.0006}_{-0.0004}$	$0.0101 \pm 0.0003\ ^{+0.0005}_{-0.0003}$
0.7	$0.0564 \pm 0.0006\ ^{+0.0014}_{-0.0013}$	$0.0356 \pm 0.0005\ ^{+0.0009}_{-0.0009}$	$0.0229 \pm 0.0004\ ^{+0.0005}_{-0.0007}$	$0.0146 \pm 0.0003\ ^{+0.0006}_{-0.0004}$	$0.0089 \pm 0.0002\ ^{+0.0005}_{-0.0002}$
0.9	$0.0507 \pm 0.0005\ ^{+0.0019}_{-0.0004}$	$0.0316 \pm 0.0004\ ^{+0.0013}_{-0.0003}$	$0.0194 \pm 0.0004\ ^{+0.0007}_{-0.0005}$	$0.0126 \pm 0.0003\ ^{+0.0003}_{-0.0004}$	$0.0081 \pm 0.0002\ ^{+0.0004}_{-0.0004}$
1.1	$0.0483 \pm 0.0005\ ^{+0.0017}_{-0.0012}$	$0.0299 \pm 0.0004\ ^{+0.0016}_{-0.0006}$	$0.0182 \pm 0.0003\ ^{+0.0005}_{-0.0010}$	$0.0110 \pm 0.0003\ ^{+0.0002}_{-0.0006}$	$0.0075 \pm 0.0002\ ^{+0.0004}_{-0.0003}$
1.3	$0.0431 \pm 0.0005\ ^{+0.0022}_{-0.0020}$	$0.0251 \pm 0.0004\ ^{+0.0013}_{-0.0011}$	$0.0155 \pm 0.0003\ ^{+0.0008}_{-0.0003}$	$0.0087 \pm 0.0002\ ^{+0.0005}_{-0.0003}$	$0.0055 \pm 0.0002\ ^{+0.0004}_{-0.0001}$
1.5	$0.0361 \pm 0.0005\ ^{+0.0019}_{-0.0013}$	$0.0208 \pm 0.0004\ ^{+0.0009}_{-0.0010}$	$0.0121 \pm 0.0003\ ^{+0.0009}_{-0.0005}$	$0.0064 \pm 0.0002\ ^{+0.0006}_{-0.0003}$	$0.0036 \pm 0.0002\ ^{+0.0004}_{-0.0002}$
1.7	$0.0290 \pm 0.0004\ ^{+0.0022}_{-0.0013}$	$0.0159 \pm 0.0003\ ^{+0.0015}_{-0.0001}$	$0.0086 \pm 0.0002\ ^{+0.0007}_{-0.0005}$	$0.0040 \pm 0.0002\ ^{+0.0003}_{-0.0003}$	$0.0023 \pm 0.0001\ ^{+0.0003}_{-0.0003}$
1.9	$0.0212 \pm 0.0004\ ^{+0.0025}_{-0.0012}$	$0.0109 \pm 0.0003\ ^{+0.0016}_{-0.0006}$	$0.0047 \pm 0.0002\ ^{+0.0005}_{-0.0004}$	$0.0022 \pm 0.0001\ ^{+0.0004}_{-0.0002}$	$0.0012 \pm 0.0001\ ^{+0.0001}_{-0.0002}$
2.1	$0.0130 \pm 0.0003\ ^{+0.0024}_{-0.0012}$	$0.0056 \pm 0.0002\ ^{+0.0008}_{-0.0004}$	—	—	—
2.3	$0.0050 \pm 0.0002\ ^{+0.0013}_{-0.0007}$	—	—	—	—

Table A.4: π^- $\frac{\mathrm{d}^2n}{\mathrm{d}y\mathrm{d}p_T}$ spectra

y	p_T (GeV/c)				
	0.1	0.2	0.3	0.4	0.5
0.1	—	—	—	—	$0.7555 \pm 0.0022\ ^{+0.0073}_{-0.0094}$
0.3	—	—	—	$1.0383 \pm 0.0024\ ^{+0.0062}_{-0.0110}$	$0.7570 \pm 0.0022\ ^{+0.0099}_{-0.0085}$
0.5	—	—	$1.0042 \pm 0.0024\ ^{+0.0029}_{-0.0097}$	$1.0623 \pm 0.0025\ ^{+0.0047}_{-0.0086}$	$0.7395 \pm 0.0021\ ^{+0.0075}_{-0.0118}$
0.7	—	—	$1.2757 \pm 0.0027\ ^{+0.0050}_{-0.0134}$	$0.9900 \pm 0.0024\ ^{+0.0047}_{-0.0062}$	$0.6833 \pm 0.0020\ ^{+0.0078}_{-0.0098}$
0.9	—	$1.0620 \pm 0.0025\ ^{+0.0029}_{-0.0085}$	$1.2360 \pm 0.0026\ ^{+0.0062}_{-0.0104}$	$0.9662 \pm 0.0023\ ^{+0.0069}_{-0.0012}$	$0.6621 \pm 0.0019\ ^{+0.0069}_{-0.0018}$
1.1	$0.3696 \pm 0.0015\ ^{+0.0006}_{-0.0025}$	$1.0995 \pm 0.0025\ ^{+0.0022}_{-0.0067}$	$1.1414 \pm 0.0025\ ^{+0.0062}_{-0.0091}$	$0.8927 \pm 0.0022\ ^{+0.0067}_{-0.0070}$	$0.6093 \pm 0.0018\ ^{+0.0038}_{-0.0035}$
1.3	$0.4158 \pm 0.0015\ ^{+0.0013}_{-0.0015}$	$0.9973 \pm 0.0023\ ^{+0.0014}_{-0.0060}$	$1.0362 \pm 0.0024\ ^{+0.0055}_{-0.0089}$	$0.8019 \pm 0.0021\ ^{+0.0045}_{-0.0071}$	$0.5473 \pm 0.0017\ ^{+0.0033}_{-0.0073}$
1.5	$0.3702 \pm 0.0014\ ^{+0.0013}_{-0.0003}$	$0.8906 \pm 0.0022\ ^{+0.0028}_{-0.0058}$	$0.9243 \pm 0.0023\ ^{+0.0033}_{-0.0091}$	$0.7109 \pm 0.0020\ ^{+0.0041}_{-0.0078}$	$0.4834 \pm 0.0016\ ^{+0.0044}_{-0.0105}$
1.7	$0.3336 \pm 0.0013\ ^{+0.0003}_{-0.0012}$	$0.7806 \pm 0.0021\ ^{+0.0028}_{-0.0058}$	$0.7939 \pm 0.0021\ ^{+0.0014}_{-0.0091}$	$0.5967 \pm 0.0018\ ^{+0.0061}_{-0.0101}$	$0.4044 \pm 0.0015\ ^{+0.0048}_{-0.0083}$
1.9	$0.2942 \pm 0.0013\ ^{+0.0000}_{-0.0017}$	$0.6726 \pm 0.0019\ ^{+0.0007}_{-0.0062}$	$0.6597 \pm 0.0019\ ^{+0.0057}_{-0.0095}$	$0.4846 \pm 0.0016\ ^{+0.0076}_{-0.0058}$	$0.3238 \pm 0.0013\ ^{+0.0041}_{-0.0034}$
2.1	$0.2552 \pm 0.0012\ ^{+0.0006}_{-0.0021}$	$0.5629 \pm 0.0018\ ^{+0.0019}_{-0.0065}$	$0.5279 \pm 0.0017\ ^{+0.0069}_{-0.0069}$	$0.3770 \pm 0.0014\ ^{+0.0062}_{-0.0016}$	$0.2431 \pm 0.0011\ ^{+0.0030}_{-0.0060}$
2.3	$0.2187 \pm 0.0011\ ^{+0.0003}_{-0.0021}$	$0.4589 \pm 0.0016\ ^{+0.0034}_{-0.0078}$	$0.4101 \pm 0.0015\ ^{+0.0055}_{-0.0021}$	$0.2715 \pm 0.0012\ ^{+0.0037}_{-0.0058}$	$0.1671 \pm 0.0009\ ^{+0.0006}_{-0.0045}$

y	p_T (GeV/c)				
	0.6	0.7	0.8	0.9	1.0
0.1	$0.5097 \pm 0.0018\ ^{+0.0072}_{-0.0011}$	$0.3339 \pm 0.0015\ ^{+0.0043}_{-0.0014}$	$0.2125 \pm 0.0012\ ^{+0.0024}_{-0.0044}$	$0.1371 \pm 0.0010\ ^{+0.0028}_{-0.0002}$	$0.0851 \pm 0.0008\ ^{+0.0021}_{-0.0018}$
0.3	$0.5073 \pm 0.0018\ ^{+0.0077}_{-0.0055}$	$0.3319 \pm 0.0015\ ^{+0.0048}_{-0.0051}$	$0.2099 \pm 0.0012\ ^{+0.0012}_{-0.0047}$	$0.1335 \pm 0.0010\ ^{+0.0030}_{-0.0001}$	$0.0859 \pm 0.0008\ ^{+0.0021}_{-0.0013}$
0.5	$0.4912 \pm 0.0018\ ^{+0.0041}_{-0.0057}$	$0.3145 \pm 0.0015\ ^{+0.0038}_{-0.0044}$	$0.2005 \pm 0.0012\ ^{+0.0038}_{-0.0047}$	$0.1261 \pm 0.0010\ ^{+0.0017}_{-0.0015}$	$0.0790 \pm 0.0008\ ^{+0.0017}_{-0.0023}$
0.7	$0.4530 \pm 0.0017\ ^{+0.0007}_{-0.0078}$	$0.2923 \pm 0.0013\ ^{+0.0026}_{-0.0027}$	$0.1822 \pm 0.0011\ ^{+0.0025}_{-0.0044}$	$0.1160 \pm 0.0009\ ^{+0.0013}_{-0.0014}$	$0.0725 \pm 0.0007\ ^{+0.0001}_{-0.0021}$
0.9	$0.4275 \pm 0.0016\ ^{+0.0015}_{-0.0053}$	$0.2713 \pm 0.0012\ ^{+0.0019}_{-0.0032}$	$0.1675 \pm 0.0010\ ^{+0.0030}_{-0.0005}$	$0.1039 \pm 0.0008\ ^{+0.0014}_{-0.0018}$	$0.0631 \pm 0.0006\ ^{+0.0012}_{-0.0019}$
1.1	$0.3944 \pm 0.0015\ ^{+0.0012}_{-0.0058}$	$0.2506 \pm 0.0012\ ^{+0.0021}_{-0.0040}$	$0.1530 \pm 0.0009\ ^{+0.0025}_{-0.0035}$	$0.0928 \pm 0.0007\ ^{+0.0013}_{-0.0027}$	$0.0566 \pm 0.0006\ ^{+0.0008}_{-0.0014}$
1.3	$0.3537 \pm 0.0014\ ^{+0.0014}_{-0.0083}$	$0.2200 \pm 0.0011\ ^{+0.0030}_{-0.0059}$	$0.1339 \pm 0.0009\ ^{+0.0008}_{-0.0041}$	$0.0801 \pm 0.0007\ ^{+0.0008}_{-0.0017}$	$0.0475 \pm 0.0005\ ^{+0.0005}_{-0.0015}$
1.5	$0.3076 \pm 0.0013\ ^{+0.0043}_{-0.0067}$	$0.1887 \pm 0.0010\ ^{+0.0028}_{-0.0023}$	$0.1137 \pm 0.0008\ ^{+0.0009}_{-0.0035}$	$0.0655 \pm 0.0006\ ^{+0.0007}_{-0.0023}$	$0.0386 \pm 0.0005\ ^{+0.0007}_{-0.0008}$
1.7	$0.2568 \pm 0.0012\ ^{+0.0051}_{-0.0008}$	$0.1570 \pm 0.0009\ ^{+0.0023}_{-0.0039}$	$0.0907 \pm 0.0007\ ^{+0.0011}_{-0.0029}$	$0.0515 \pm 0.0005\ ^{+0.0004}_{-0.0017}$	$0.0283 \pm 0.0004\ ^{+0.0006}_{-0.0001}$
1.9	$0.2030 \pm 0.0011\ ^{+0.0038}_{-0.0034}$	$0.1192 \pm 0.0008\ ^{+0.0008}_{-0.0035}$	$0.0677 \pm 0.0006\ ^{+0.0002}_{-0.0018}$	$0.0371 \pm 0.0005\ ^{+0.0006}_{-0.0005}$	$0.0198 \pm 0.0003\ ^{+0.0003}_{-0.0001}$
2.1	$0.1477 \pm 0.0009\ ^{+0.0008}_{-0.0038}$	$0.0838 \pm 0.0007\ ^{+0.0008}_{-0.0014}$	$0.0450 \pm 0.0005\ ^{+0.0006}_{-0.0004}$	$0.0227 \pm 0.0004\ ^{+0.0004}_{-0.0001}$	$0.0113 \pm 0.0003\ ^{+0.0002}_{-0.0000}$
2.3	$0.0967 \pm 0.0007\ ^{+0.0004}_{-0.0026}$	$0.0533 \pm 0.0005\ ^{+0.0009}_{-0.0003}$	$0.0261 \pm 0.0004\ ^{+0.0002}_{-0.0005}$	$0.0119 \pm 0.0003\ ^{+0.0002}_{-0.0000}$	$0.0051 \pm 0.0002\ ^{+0.0000}_{-0.0000}$

y	p_T (GeV/c)				
	1.1	1.2	1.3	1.4	1.5
0.1	$0.0533 \pm 0.0006\ ^{+0.0012}_{-0.0007}$	$0.0346 \pm 0.0005\ ^{+0.0008}_{-0.0005}$	$0.0217 \pm 0.0004\ ^{+0.0004}_{-0.0005}$	$0.0142 \pm 0.0004\ ^{+0.0002}_{-0.0004}$	$0.0089 \pm 0.0003\ ^{+0.0001}_{-0.0003}$
0.3	$0.0531 \pm 0.0007\ ^{+0.0014}_{-0.0002}$	$0.0342 \pm 0.0005\ ^{+0.0009}_{-0.0001}$	$0.0216 \pm 0.0004\ ^{+0.0003}_{-0.0006}$	$0.0136 \pm 0.0003\ ^{+0.0000}_{-0.0005}$	$0.0089 \pm 0.0003\ ^{+0.0003}_{-0.0003}$
0.5	$0.0490 \pm 0.0006\ ^{+0.0013}_{-0.0010}$	$0.0307 \pm 0.0005\ ^{+0.0008}_{-0.0003}$	$0.0199 \pm 0.0004\ ^{+0.0003}_{-0.0006}$	$0.0125 \pm 0.0003\ ^{+0.0002}_{-0.0002}$	$0.0075 \pm 0.0002\ ^{+0.0002}_{-0.0001}$
0.7	$0.0459 \pm 0.0006\ ^{+0.0009}_{-0.0015}$	$0.0279 \pm 0.0004\ ^{+0.0004}_{-0.0008}$	$0.0173 \pm 0.0003\ ^{+0.0003}_{-0.0006}$	$0.0107 \pm 0.0003\ ^{+0.0002}_{-0.0003}$	$0.0071 \pm 0.0002\ ^{+0.0001}_{-0.0002}$
0.9	$0.0389 \pm 0.0005\ ^{+0.0004}_{-0.0013}$	$0.0244 \pm 0.0004\ ^{+0.0003}_{-0.0006}$	$0.0147 \pm 0.0003\ ^{+0.0000}_{-0.0005}$	$0.0093 \pm 0.0002\ ^{+0.0001}_{-0.0003}$	$0.0057 \pm 0.0002\ ^{+0.0001}_{-0.0002}$
1.1	$0.0348 \pm 0.0004\ ^{+0.0004}_{-0.0012}$	$0.0209 \pm 0.0003\ ^{+0.0002}_{-0.0006}$	$0.0126 \pm 0.0003\ ^{+0.0003}_{-0.0003}$	$0.0074 \pm 0.0002\ ^{+0.0000}_{-0.0002}$	$0.0045 \pm 0.0002\ ^{+0.0001}_{-0.0001}$
1.3	$0.0282 \pm 0.0004\ ^{+0.0007}_{-0.0009}$	$0.0164 \pm 0.0003\ ^{+0.0003}_{-0.0004}$	$0.0098 \pm 0.0002\ ^{+0.0003}_{-0.0000}$	$0.0051 \pm 0.0002\ ^{+0.0002}_{-0.0001}$	$0.0031 \pm 0.0001\ ^{+0.0001}_{-0.0000}$
1.5	$0.0217 \pm 0.0004\ ^{+0.0005}_{-0.0003}$	$0.0121 \pm 0.0003\ ^{+0.0003}_{-0.0000}$	$0.0070 \pm 0.0002\ ^{+0.0001}_{-0.0000}$	$0.0037 \pm 0.0001\ ^{+0.0001}_{-0.0001}$	$0.0021 \pm 0.0001\ ^{+0.0000}_{-0.0000}$
1.7	$0.0154 \pm 0.0003\ ^{+0.0003}_{-0.0001}$	$0.0080 \pm 0.0002\ ^{+0.0002}_{-0.0001}$	$0.0043 \pm 0.0002\ ^{+0.0001}_{-0.0000}$	$0.0023 \pm 0.0001\ ^{+0.0000}_{-0.0001}$	$0.0011 \pm 0.0001\ ^{+0.0000}_{-0.0000}$
1.9	$0.0100 \pm 0.0002\ ^{+0.0002}_{-0.0001}$	$0.0049 \pm 0.0002\ ^{+0.0001}_{-0.0000}$	—	—	—
2.1	$0.0053 \pm 0.0002\ ^{+0.0001}_{-0.0000}$	—	—	—	—
2.3	—	—	—	—	—

Table A.5: K^+ $\frac{\mathrm{d}^2n}{\mathrm{d}y\mathrm{d}p_T}$ spectra

y	p_T (GeV/c)				
	0.1	0.2	0.3	0.4	0.5
0.1	$0.0283 \pm 0.0004\ ^{+0.0005}_{-0.0005}$	$0.0753 \pm 0.0007\ ^{+0.0026}_{-0.0006}$	$0.0979 \pm 0.0008\ ^{+0.0115}_{-0.0056}$	$0.0967 \pm 0.0008\ ^{+0.0078}_{-0.0075}$	$0.0824 \pm 0.0007\ ^{+0.0015}_{-0.0031}$
0.3	$0.0290 \pm 0.0004\ ^{+0.0000}_{-0.0003}$	$0.0802 \pm 0.0007\ ^{+0.0021}_{-0.0031}$	$0.0991 \pm 0.0008\ ^{+0.0048}_{-0.0003}$	$0.0937 \pm 0.0007\ ^{+0.0046}_{-0.0029}$	$0.0857 \pm 0.0007\ ^{+0.0001}_{-0.0027}$
0.5	$0.0307 \pm 0.0004\ ^{+0.0003}_{-0.0017}$	$0.0780 \pm 0.0007\ ^{+0.0026}_{-0.0020}$	$0.0986 \pm 0.0008\ ^{+0.0035}_{-0.0000}$	$0.1028 \pm 0.0008\ ^{+0.0007}_{-0.0004}$	$0.0856 \pm 0.0007\ ^{+0.0000}_{-0.0009}$
0.7	$0.0298 \pm 0.0004\ ^{+0.0001}_{-0.0004}$	$0.0767 \pm 0.0007\ ^{+0.0000}_{-0.0017}$	$0.0975 \pm 0.0008\ ^{+0.0001}_{-0.0003}$	$0.0967 \pm 0.0008\ ^{+0.0008}_{-0.0057}$	$0.0868 \pm 0.0007\ ^{+0.0014}_{-0.0018}$
0.9	$0.0287 \pm 0.0004\ ^{+0.0006}_{-0.0019}$	$0.0728 \pm 0.0006\ ^{+0.0019}_{-0.0030}$	$0.0953 \pm 0.0007\ ^{+0.0049}_{-0.0032}$	$0.0943 \pm 0.0007\ ^{+0.0026}_{-0.0037}$	$0.0835 \pm 0.0007\ ^{+0.0045}_{-0.0028}$
1.1	$0.0260 \pm 0.0004\ ^{+0.0013}_{-0.0015}$	$0.0667 \pm 0.0006\ ^{+0.0005}_{-0.0038}$	$0.0903 \pm 0.0007\ ^{+0.0045}_{-0.0061}$	$0.0894 \pm 0.0007\ ^{+0.0015}_{-0.0053}$	$0.0796 \pm 0.0007\ ^{+0.0025}_{-0.0038}$
1.3	$0.0216 \pm 0.0004\ ^{+0.0037}_{-0.0005}$	$0.0568 \pm 0.0006\ ^{+0.0108}_{-0.0031}$	$0.0795 \pm 0.0007\ ^{+0.0051}_{-0.0030}$	$0.0740 \pm 0.0007\ ^{+0.0064}_{-0.0038}$	$0.0623 \pm 0.0006\ ^{+0.0048}_{-0.0001}$
1.5	$0.0158 \pm 0.0003\ ^{+0.0027}_{-0.0001}$	$0.0434 \pm 0.0005\ ^{+0.0074}_{-0.0011}$	$0.0602 \pm 0.0006\ ^{+0.0064}_{-0.0080}$	$0.0613 \pm 0.0006\ ^{+0.0081}_{-0.0021}$	$0.0639 \pm 0.0006\ ^{+0.0052}_{-0.0059}$
1.7	$0.0117 \pm 0.0003\ ^{+0.0016}_{-0.0001}$	$0.0375 \pm 0.0005\ ^{+0.0051}_{-0.0002}$	$0.0552 \pm 0.0005\ ^{+0.0051}_{-0.0050}$	$0.0545 \pm 0.0005\ ^{+0.0050}_{-0.0035}$	$0.0455 \pm 0.0005\ ^{+0.0042}_{-0.0029}$
1.9	$0.0107 \pm 0.0003\ ^{+0.0011}_{-0.0004}$	$0.0279 \pm 0.0004\ ^{+0.0030}_{-0.0017}$	$0.0327 \pm 0.0004\ ^{+0.0040}_{-0.0027}$	$0.0399 \pm 0.0005\ ^{+0.0022}_{-0.0043}$	$0.0352 \pm 0.0005\ ^{+0.0005}_{-0.0004}$

y	p_T (GeV/c)				
	0.6	0.7	0.8	0.9	1.0
0.1	$0.0651 \pm 0.0007\ ^{+0.0021}_{-0.0025}$	$0.0527 \pm 0.0006\ ^{+0.0053}_{-0.0017}$	$0.0382 \pm 0.0005\ ^{+0.0013}_{-0.0023}$	$0.0279 \pm 0.0005\ ^{+0.0017}_{-0.0003}$	$0.0194 \pm 0.0004\ ^{+0.0004}_{-0.0010}$
0.3	$0.0703 \pm 0.0007\ ^{+0.0067}_{-0.0010}$	$0.0555 \pm 0.0006\ ^{+0.0056}_{-0.0013}$	$0.0427 \pm 0.0006\ ^{+0.0005}_{-0.0016}$	$0.0294 \pm 0.0005\ ^{+0.0001}_{-0.0009}$	$0.0215 \pm 0.0004\ ^{+0.0004}_{-0.0004}$
0.5	$0.0728 \pm 0.0007\ ^{+0.0015}_{-0.0045}$	$0.0537 \pm 0.0006\ ^{+0.0035}_{-0.0016}$	$0.0383 \pm 0.0005\ ^{+0.0037}_{-0.0004}$	$0.0270 \pm 0.0005\ ^{+0.0004}_{-0.0014}$	$0.0206 \pm 0.0004\ ^{+0.0004}_{-0.0006}$
0.7	$0.0710 \pm 0.0006\ ^{+0.0032}_{-0.0025}$	$0.0535 \pm 0.0006\ ^{+0.0010}_{-0.0017}$	$0.0349 \pm 0.0005\ ^{+0.0011}_{-0.0011}$	$0.0241 \pm 0.0004\ ^{+0.0017}_{-0.0003}$	$0.0179 \pm 0.0003\ ^{+0.0008}_{-0.0000}$
0.9	$0.0616 \pm 0.0006\ ^{+0.0029}_{-0.0003}$	$0.0443 \pm 0.0005\ ^{+0.0035}_{-0.0000}$	$0.0337 \pm 0.0005\ ^{+0.0008}_{-0.0004}$	$0.0221 \pm 0.0004\ ^{+0.0021}_{-0.0000}$	$0.0169 \pm 0.0003\ ^{+0.0000}_{-0.0005}$
1.1	$0.0597 \pm 0.0006\ ^{+0.0001}_{-0.0026}$	$0.0419 \pm 0.0005\ ^{+0.0019}_{-0.0000}$	$0.0329 \pm 0.0004\ ^{+0.0009}_{-0.0014}$	$0.0203 \pm 0.0004\ ^{+0.0002}_{-0.0018}$	$0.0137 \pm 0.0003\ ^{+0.0003}_{-0.0010}$
1.3	$0.0541 \pm 0.0006\ ^{+0.0035}_{-0.0025}$	$0.0423 \pm 0.0005\ ^{+0.0025}_{-0.0040}$	$0.0297 \pm 0.0004\ ^{+0.0012}_{-0.0022}$	$0.0175 \pm 0.0003\ ^{+0.0010}_{-0.0004}$	$0.0103 \pm 0.0002\ ^{+0.0011}_{-0.0004}$
1.5	$0.0451 \pm 0.0005\ ^{+0.0035}_{-0.0025}$	$0.0342 \pm 0.0005\ ^{+0.0027}_{-0.0023}$	$0.0239 \pm 0.0004\ ^{+0.0003}_{-0.0022}$	$0.0122 \pm 0.0003\ ^{+0.0001}_{-0.0010}$	$0.0099 \pm 0.0003\ ^{+0.0016}_{-0.0002}$
1.7	$0.0338 \pm 0.0004\ ^{+0.0006}_{-0.0027}$	$0.0259 \pm 0.0004\ ^{+0.0003}_{-0.0002}$	$0.0152 \pm 0.0003\ ^{+0.0024}_{-0.0001}$	$0.0045 \pm 0.0002\ ^{+0.0009}_{-0.0002}$	$0.0019 \pm 0.0001\ ^{+0.0004}_{-0.0001}$
1.9	$0.0208 \pm 0.0004\ ^{+0.0035}_{-0.0002}$	$0.0126 \pm 0.0003\ ^{+0.0020}_{-0.0006}$	$0.0106 \pm 0.0003\ ^{+0.0004}_{-0.0009}$	$0.0024 \pm 0.0001\ ^{+0.0002}_{-0.0000}$	—

y	p_T (GeV/c)				
	1.1	1.2	1.3	1.4	1.5
0.1	$0.0140 \pm 0.0003\ ^{+0.0004}_{-0.0000}$	$0.0094 \pm 0.0003\ ^{+0.0003}_{-0.0002}$	$0.0064 \pm 0.0002\ ^{+0.0004}_{-0.0000}$	$0.0046 \pm 0.0002\ ^{+0.0000}_{-0.0002}$	$0.0032 \pm 0.0002\ ^{+0.0002}_{-0.0000}$
0.3	$0.0151 \pm 0.0004\ ^{+0.0011}_{-0.0001}$	$0.0103 \pm 0.0003\ ^{+0.0006}_{-0.0000}$	$0.0071 \pm 0.0003\ ^{+0.0001}_{-0.0000}$	$0.0055 \pm 0.0002\ ^{+0.0000}_{-0.0003}$	$0.0031 \pm 0.0002\ ^{+0.0001}_{-0.0000}$
0.5	$0.0147 \pm 0.0003\ ^{+0.0001}_{-0.0010}$	$0.0100 \pm 0.0003\ ^{+0.0002}_{-0.0000}$	$0.0072 \pm 0.0002\ ^{+0.0003}_{-0.0000}$	$0.0052 \pm 0.0002\ ^{+0.0003}_{-0.0000}$	$0.0031 \pm 0.0002\ ^{+0.0001}_{-0.0001}$
0.7	$0.0120 \pm 0.0003\ ^{+0.0007}_{-0.0000}$	$0.0078 \pm 0.0003\ ^{+0.0007}_{-0.0001}$	$0.0056 \pm 0.0002\ ^{+0.0003}_{-0.0002}$	$0.0035 \pm 0.0002\ ^{+0.0001}_{-0.0001}$	$0.0021 \pm 0.0001\ ^{+0.0001}_{-0.0002}$
0.9	$0.0110 \pm 0.0003\ ^{+0.0003}_{-0.0007}$	$0.0079 \pm 0.0002\ ^{+0.0002}_{-0.0007}$	$0.0045 \pm 0.0002\ ^{+0.0002}_{-0.0002}$	$0.0032 \pm 0.0001\ ^{+0.0000}_{-0.0001}$	$0.0022 \pm 0.0001\ ^{+0.0002}_{-0.0000}$
1.1	$0.0090 \pm 0.0002\ ^{+0.0001}_{-0.0001}$	$0.0059 \pm 0.0002\ ^{+0.0004}_{-0.0001}$	$0.0042 \pm 0.0002\ ^{+0.0001}_{-0.0004}$	$0.0026 \pm 0.0001\ ^{+0.0000}_{-0.0001}$	$0.0012 \pm 0.0001\ ^{+0.0000}_{-0.0000}$
1.3	$0.0076 \pm 0.0002\ ^{+0.0000}_{-0.0003}$	$0.0039 \pm 0.0002\ ^{+0.0004}_{-0.0001}$	$0.0016 \pm 0.0001\ ^{+0.0001}_{-0.0000}$	$0.0017 \pm 0.0001\ ^{+0.0001}_{-0.0001}$	$0.0009 \pm 0.0001\ ^{+0.0000}_{-0.0001}$
1.5	$0.0052 \pm 0.0002\ ^{+0.0003}_{-0.0006}$	$0.0022 \pm 0.0001\ ^{+0.0003}_{-0.0001}$	$0.0018 \pm 0.0001\ ^{+0.0000}_{-0.0001}$	$0.0014 \pm 0.0001\ ^{+0.0000}_{-0.0001}$	$0.0005 \pm 0.0001\ ^{+0.0000}_{-0.0000}$
1.7	$0.0024 \pm 0.0001\ ^{+0.0000}_{-0.0002}$	$0.0007 \pm 0.0001\ ^{+0.0001}_{-0.0000}$	$0.0008 \pm 0.0001\ ^{+0.0001}_{-0.0001}$	—	—
1.9	—	—	—	—	—

Table A.6: K^- $\frac{\mathrm{d}^2n}{\mathrm{d}y\mathrm{d}p_T}$ spectra

y	p_T (GeV/c)				
	0.1	0.2	0.3	0.4	0.5
0.1	$0.0206 \pm 0.0004\ ^{+0.0015}_{-0.0008}$	$0.0565 \pm 0.0006\ ^{+0.0063}_{-0.0029}$	$0.0798 \pm 0.0007\ ^{+0.0114}_{-0.0018}$	$0.0798 \pm 0.0007\ ^{+0.0085}_{-0.0013}$	$0.0735 \pm 0.0007\ ^{+0.0090}_{-0.0065}$
0.3	$0.0206 \pm 0.0004\ ^{+0.0003}_{-0.0010}$	$0.0566 \pm 0.0006\ ^{+0.0046}_{-0.0010}$	$0.0740 \pm 0.0007\ ^{+0.0072}_{-0.0045}$	$0.0731 \pm 0.0007\ ^{+0.0054}_{-0.0017}$	$0.0675 \pm 0.0007\ ^{+0.0079}_{-0.0058}$
0.5	$0.0205 \pm 0.0004\ ^{+0.0005}_{-0.0003}$	$0.0540 \pm 0.0006\ ^{+0.0039}_{-0.0020}$	$0.0694 \pm 0.0007\ ^{+0.0059}_{-0.0033}$	$0.0695 \pm 0.0006\ ^{+0.0010}_{-0.0038}$	$0.0606 \pm 0.0006\ ^{+0.0009}_{-0.0045}$
0.7	$0.0192 \pm 0.0003\ ^{+0.0015}_{-0.0003}$	$0.0498 \pm 0.0005\ ^{+0.0039}_{-0.0039}$	$0.0654 \pm 0.0006\ ^{+0.0057}_{-0.0034}$	$0.0659 \pm 0.0006\ ^{+0.0057}_{-0.0034}$	$0.0550 \pm 0.0006\ ^{+0.0009}_{-0.0012}$
0.9	$0.0173 \pm 0.0003\ ^{+0.0016}_{-0.0009}$	$0.0463 \pm 0.0005\ ^{+0.0047}_{-0.0032}$	$0.0592 \pm 0.0006\ ^{+0.0072}_{-0.0006}$	$0.0602 \pm 0.0006\ ^{+0.0043}_{-0.0007}$	$0.0505 \pm 0.0005\ ^{+0.0052}_{-0.0000}$
1.1	$0.0154 \pm 0.0003\ ^{+0.0020}_{-0.0016}$	$0.0420 \pm 0.0005\ ^{+0.0057}_{-0.0011}$	$0.0527 \pm 0.0006\ ^{+0.0093}_{-0.0007}$	$0.0526 \pm 0.0006\ ^{+0.0095}_{-0.0035}$	$0.0449 \pm 0.0005\ ^{+0.0088}_{-0.0041}$
1.3	$0.0130 \pm 0.0003\ ^{+0.0023}_{-0.0018}$	$0.0354 \pm 0.0004\ ^{+0.0077}_{-0.0041}$	$0.0453 \pm 0.0005\ ^{+0.0094}_{-0.0057}$	$0.0463 \pm 0.0005\ ^{+0.0085}_{-0.0072}$	$0.0374 \pm 0.0005\ ^{+0.0078}_{-0.0047}$
1.5	$0.0121 \pm 0.0003\ ^{+0.0032}_{-0.0003}$	$0.0316 \pm 0.0004\ ^{+0.0081}_{-0.0018}$	$0.0379 \pm 0.0005\ ^{+0.0062}_{-0.0062}$	$0.0370 \pm 0.0005\ ^{+0.0031}_{-0.0067}$	$0.0294 \pm 0.0004\ ^{+0.0016}_{-0.0040}$
1.7	$0.0089 \pm 0.0002\ ^{+0.0021}_{-0.0001}$	$0.0230 \pm 0.0004\ ^{+0.0050}_{-0.0005}$	$0.0280 \pm 0.0004\ ^{+0.0002}_{-0.0049}$	$0.0271 \pm 0.0004\ ^{+0.0022}_{-0.0047}$	$0.0204 \pm 0.0003\ ^{+0.0043}_{-0.0036}$
1.9	$0.0062 \pm 0.0002\ ^{+0.0017}_{-0.0004}$	$0.0169 \pm 0.0003\ ^{+0.0043}_{-0.0017}$	$0.0202 \pm 0.0003\ ^{+0.0048}_{-0.0039}$	$0.0185 \pm 0.0003\ ^{+0.0049}_{-0.0030}$	$0.0133 \pm 0.0003\ ^{+0.0040}_{-0.0008}$

y	p_T (GeV/c)				
	0.6	0.7	0.8	0.9	1.0
0.1	$0.0560 \pm 0.0006\ ^{+0.0049}_{-0.0043}$	$0.0430 \pm 0.0006\ ^{+0.0032}_{-0.0034}$	$0.0299 \pm 0.0005\ ^{+0.0033}_{-0.0004}$	$0.0210 \pm 0.0004\ ^{+0.0004}_{-0.0013}$	$0.0141 \pm 0.0003\ ^{+0.0002}_{-0.0013}$
0.3	$0.0533 \pm 0.0006\ ^{+0.0044}_{-0.0001}$	$0.0395 \pm 0.0005\ ^{+0.0016}_{-0.0028}$	$0.0285 \pm 0.0005\ ^{+0.0036}_{-0.0022}$	$0.0197 \pm 0.0004\ ^{+0.0005}_{-0.0010}$	$0.0138 \pm 0.0003\ ^{+0.0012}_{-0.0012}$
0.5	$0.0473 \pm 0.0005\ ^{+0.0049}_{-0.0000}$	$0.0342 \pm 0.0005\ ^{+0.0010}_{-0.0011}$	$0.0257 \pm 0.0004\ ^{+0.0029}_{-0.0026}$	$0.0175 \pm 0.0003\ ^{+0.0014}_{-0.0002}$	$0.0114 \pm 0.0003\ ^{+0.0013}_{-0.0001}$
0.7	$0.0440 \pm 0.0005\ ^{+0.0026}_{-0.0008}$	$0.0319 \pm 0.0004\ ^{+0.0017}_{-0.0006}$	$0.0212 \pm 0.0004\ ^{+0.0001}_{-0.0022}$	$0.0138 \pm 0.0003\ ^{+0.0000}_{-0.0014}$	$0.0090 \pm 0.0002\ ^{+0.0011}_{-0.0002}$
0.9	$0.0410 \pm 0.0005\ ^{+0.0034}_{-0.0014}$	$0.0292 \pm 0.0004\ ^{+0.0027}_{-0.0002}$	$0.0196 \pm 0.0003\ ^{+0.0015}_{-0.0020}$	$0.0129 \pm 0.0003\ ^{+0.0019}_{-0.0012}$	$0.0082 \pm 0.0002\ ^{+0.0011}_{-0.0006}$
1.1	$0.0351 \pm 0.0004\ ^{+0.0061}_{-0.0018}$	$0.0244 \pm 0.0004\ ^{+0.0042}_{-0.0025}$	$0.0162 \pm 0.0003\ ^{+0.0031}_{-0.0007}$	$0.0104 \pm 0.0002\ ^{+0.0018}_{-0.0001}$	$0.0066 \pm 0.0002\ ^{+0.0009}_{-0.0000}$
1.3	$0.0285 \pm 0.0004\ ^{+0.0028}_{-0.0038}$	$0.0192 \pm 0.0003\ ^{+0.0009}_{-0.0024}$	$0.0122 \pm 0.0003\ ^{+0.0030}_{-0.0002}$	$0.0081 \pm 0.0002\ ^{+0.0019}_{-0.0000}$	$0.0051 \pm 0.0002\ ^{+0.0013}_{-0.0001}$
1.5	$0.0216 \pm 0.0003\ ^{+0.0011}_{-0.0036}$	$0.0147 \pm 0.0003\ ^{+0.0028}_{-0.0024}$	$0.0089 \pm 0.0002\ ^{+0.0020}_{-0.0013}$	$0.0051 \pm 0.0002\ ^{+0.0014}_{-0.0001}$	$0.0032 \pm 0.0001\ ^{+0.0000}_{-0.0006}$
1.7	$0.0150 \pm 0.0003\ ^{+0.0031}_{-0.0027}$	$0.0099 \pm 0.0002\ ^{+0.0026}_{-0.0005}$	$0.0059 \pm 0.0002\ ^{+0.0014}_{-0.0001}$	$0.0029 \pm 0.0001\ ^{+0.0005}_{-0.0003}$	$0.0017 \pm 0.0001\ ^{+0.0000}_{-0.0003}$
1.9	$0.0093 \pm 0.0002\ ^{+0.0024}_{-0.0002}$	$0.0055 \pm 0.0002\ ^{+0.0009}_{-0.0004}$	$0.0031 \pm 0.0001\ ^{+0.0001}_{-0.0006}$	$0.0016 \pm 0.0001\ ^{+0.0000}_{-0.0004}$	—

y	p_T (GeV/c)				
	1.1	1.2	1.3	1.4	1.5
0.1	$0.0094 \pm 0.0003\ ^{+0.0001}_{-0.0008}$	$0.0059 \pm 0.0002\ ^{+0.0001}_{-0.0006}$	$0.0044 \pm 0.0002\ ^{+0.0003}_{-0.0001}$	$0.0027 \pm 0.0002\ ^{+0.0003}_{-0.0000}$	$0.0017 \pm 0.0001\ ^{+0.0002}_{-0.0001}$
0.3	$0.0090 \pm 0.0003\ ^{+0.0001}_{-0.0008}$	$0.0060 \pm 0.0002\ ^{+0.0000}_{-0.0006}$	$0.0041 \pm 0.0002\ ^{+0.0004}_{-0.0001}$	$0.0029 \pm 0.0002\ ^{+0.0003}_{-0.0000}$	$0.0017 \pm 0.0001\ ^{+0.0002}_{-0.0002}$
0.5	$0.0083 \pm 0.0002\ ^{+0.0009}_{-0.0009}$	$0.0049 \pm 0.0002\ ^{+0.0002}_{-0.0003}$	$0.0034 \pm 0.0002\ ^{+0.0004}_{-0.0002}$	$0.0020 \pm 0.0001\ ^{+0.0000}_{-0.0002}$	$0.0015 \pm 0.0001\ ^{+0.0000}_{-0.0001}$
0.7	$0.0065 \pm 0.0002\ ^{+0.0009}_{-0.0001}$	$0.0043 \pm 0.0002\ ^{+0.0005}_{-0.0000}$	$0.0023 \pm 0.0001\ ^{+0.0004}_{-0.0001}$	$0.0018 \pm 0.0001\ ^{+0.0002}_{-0.0000}$	$0.0007 \pm 0.0001\ ^{+0.0001}_{-0.0001}$
0.9	$0.0055 \pm 0.0002\ ^{+0.0010}_{-0.0000}$	$0.0031 \pm 0.0001\ ^{+0.0005}_{-0.0000}$	$0.0018 \pm 0.0001\ ^{+0.0003}_{-0.0000}$	$0.0013 \pm 0.0001\ ^{+0.0002}_{-0.0000}$	$0.0008 \pm 0.0001\ ^{+0.0002}_{-0.0001}$
1.1	$0.0036 \pm 0.0001\ ^{+0.0008}_{-0.0002}$	$0.0024 \pm 0.0001\ ^{+0.0005}_{-0.0000}$	$0.0013 \pm 0.0001\ ^{+0.0002}_{-0.0002}$	$0.0008 \pm 0.0001\ ^{+0.0001}_{-0.0000}$	$0.0005 \pm 0.0000\ ^{+0.0000}_{-0.0001}$
1.3	$0.0025 \pm 0.0001\ ^{+0.0004}_{-0.0003}$	$0.0017 \pm 0.0001\ ^{+0.0000}_{-0.0002}$	$0.0009 \pm 0.0001\ ^{+0.0000}_{-0.0001}$	$0.0005 \pm 0.0001\ ^{+0.0000}_{-0.0001}$	$0.0002 \pm 0.0000\ ^{+0.0000}_{-0.0000}$
1.5	$0.0017 \pm 0.0001\ ^{+0.0000}_{-0.0003}$	$0.0008 \pm 0.0001\ ^{+0.0000}_{-0.0002}$	$0.0004 \pm 0.0000\ ^{+0.0000}_{-0.0001}$	$0.0003 \pm 0.0000\ ^{+0.0001}_{-0.0001}$	$0.0001 \pm 0.0000\ ^{+0.0000}_{-0.0000}$
1.7	$0.0009 \pm 0.0001\ ^{+0.0000}_{-0.0002}$	$0.0003 \pm 0.0000\ ^{+0.0000}_{-0.0001}$	$0.0001 \pm 0.0000\ ^{+0.0000}_{-0.0000}$	—	—
1.9	—	—	—	—	—

References

[1] R. Pordes et al. The open science grid. *J. Phys. Conf. Ser.*, 78:012057, 2007. doi: 10.1088/1742-6596/78/1/012057.

[2] I. Sfiligoi et al. The pilot way to grid resources using glideinwms. *2009 WRI World Congress on Computer Science and Information Engineering*, 2:428–432, 2009. doi: 10.1109/CSIE.2009.950.

[3] K. Garrett and G. Duda. Dark matter: A primer. *Advances in Astronomy*, 2011: 1–22, 2011. doi: 10.1155/2011/968283. URL https://doi.org/10.1155%2F2011%2F968283.

[4] R. Engel T. Gaisser and E. Resconi. *Cosmic Rays and Particle Physics*. Cambridge University Press, 2 edition, 2016. doi: 10.1017/CBO9781139192194.

[5] Wikimedia Commons Public Domain image. Standard model of elementary particles, Sep 2019. URL https://commons.wikimedia.org/wiki/File:Standard_Model_of_Elementary_Particles.svg.

[6] P. A. R. Ade et al. Planck 2013 results. xvi. cosmological parameters. *Astronomy & Astrophysics*, 571:A16, oct 2014. doi: 10.1051/0004-6361/201321591.

[7] C. P. Burgess and G. D. Moore. *The standard model: A primer*. Cambridge University Press, 12 2006. ISBN 978-0-511-25485-7, 978-1-107-40426-7, 978-0-521-86036-9.

[8] CERN. The matter-antimatter asymmetry problem, 2023. URL https://home.cern/science/physics/matter-antimatter-asymmetry-problem.

[9] T. J. Sumner. Experimental searches for dark matter. *Living Reviews in Relativity*, 5:Article No. 2002–4, 2002. URL http://eudml.org/doc/230683.

[10] Antonio Boveia and Caterina Doglioni. Dark Matter Searches at Colliders. *Ann. Rev. Nucl. Part. Sci.*, 68:429–459, 2018. doi: 10.1146/annurev-nucl-101917-021008.

[11] F. Kahlhoefer. Review of LHC dark matter searches. *International Journal of Modern Physics A*, 32(13):1730006, May 2017. doi: 10.1142/s0217751x1730006x.

[12] V. C. Rubin et al. Motion of the galaxy and the local group determined from the velocity anisotropy of distant sc i galaxies. i. *The Astronomical Journal*, 81:687–718, 1976.

[13] V. C. Rubin et al. Motion of the galaxy and the local group determined from the velocity anisotropy of distant sc i galaxies. ii. *The Astronomical Journal*, 81:719–737, 1976.

[14] J. H. Oort. The force exerted by the stellar system in the direction perpendicular to the galactic plane and some related problems. *Bull. Astron. Inst. Netherlands*, 6:249, August 1932.

[15] K. Kuijken and G. Gilmore. The mass distribution in the galactic disc - III. The local volume mass density. *MNRAS*, 239:651–664, August 1989. doi: 10.1093/mnras/239.2.651.

[16] Katherine Freese. *The Cosmic Cocktail: Three Parts Dark Matter*. Princeton University Press, 2014. ISBN 9780691153353. URL http://www.jstor.org/stable/j.ctt5hhs1b.

[17] Katherine Freese. Review of Observational Evidence for Dark Matter in the Universe and in upcoming searches for Dark Stars. *EAS Publications Series*, 36:113–126, 2009. doi: 10.1051/eas/0936016.

[18] V. Springel et al. The aquarius project: The subhaloes of galactic haloes. *Monthly Notices of the Royal Astronomical Society*, 391(4):1685–1711, Dec 2008. doi: 10.1111/j.1365-2966.2008.14066.x.

[19] D. Clowe et al. A direct empirical proof of the existence of dark matter. *The Astrophysical Journal*, 648(2):L109–L113, aug 2006. doi: 10.1086/508162.

[20] F. Donato et al. Anti-deuterons as a signature of supersymmetric dark matter. *Physical Review D*, 62:043003, 2000. doi: 10.1103/PhysRevD.62.043003.

[21] Howard Baer and Stefano Profumo. Low energy antideuterons: shedding light on dark matter. *Journal of Cosmology and Astroparticle Physics*, 0512:008, 2005. doi: 10.1088/1475-7516/2005/12/008.

[22] R. Duperray et al. Flux of light antimatter nuclei near Earth, induced by cosmic rays in the Galaxy and in the atmosphere. *Phys. Rev. D*, 71:083013, 2005. doi: 10.1103/PhysRevD.71.083013.

[23] Fiorenza Donato, Nicolao Fornengo, and David Maurin. Antideuteron fluxes from dark matter annihilation in diffusion models. *Physical Review D*, 78:043506, 2008. doi: 10.1103/PhysRevD.78.043506.

[24] Carolin B. Bräuninger and Marco Cirelli. Anti-deuterons from heavy Dark Matter. *Physics Letters B*, 678:20–31, 2009. doi: 10.1016/j.physletb.2009.05.059.

[25] Y. Cui et al. General Analysis of Antideuteron Searches for Dark Matter. *Journal of High Energy Physics*, 1011:017, 2010. doi: 10.1007/JournalofHighEnergyPhysics11(2010)017.

[26] Alejandro Ibarra and Sebastian Wild. Prospects of antideuteron detection from dark matter annihilations or decays at AMS-02 and GAPS. *Journal of Cosmology and Astroparticle Physics*, 1302:021, 2013. doi: 10.1088/1475-7516/2013/02/021.

[27] Alejandro Ibarra and Sebastian Wild. Determination of the Cosmic Antideuteron Flux in a Monte Carlo approach. *Physical Review D*, 88:023014, 2013. doi: 10.1103/PhysRevD.88.023014.

[28] N. Fornengo, L. Maccione, and A. Vittino. Dark matter searches with cosmic antideuterons: status and perspectives. *Journal of Cosmology and Astroparticle Physics*, 1309:031, 2013. doi: 10.1088/1475-7516/2013/09/031.

[29] D.G. Cerdeño, M. Peiró, and S. Robles. Low-mass right-handed sneutrino dark matter: SuperCDMS and LUX constraints and the Galactic Centre gamma-ray excess. *Journal of Cosmology and Astroparticle Physics*, 1408:005, 2014. doi: 10.1088/1475-7516/2014/08/005.

[30] L.A. Dal and A.R. Raklev. Antideuteron Limits on Decaying Dark Matter with a Tuned Formation Model. *Physical Review D*, 89:103504, 2014. doi: 10.1103/PhysRevD.89.103504.

[31] M. Cirelli et al. Anti-helium from Dark Matter annihilations. *Journal of High Energy Physics*, 1408:009, 2014. doi: 10.1007/JournalofHighEnergyPhysics08(2014)009.

[32] E. Carlson, A. Coogan, T. Linden, S. Profumo, A. Ibarra, and S. Wild. Antihelium from dark matter. *Physical Review D*, 89(7):076005, April 2014. doi: 10.1103/PhysRevD.89.076005.

[33] Andrzej Hryczuk, Ilias Cholis, Roberto Iengo, Maryam Tavakoli, and Piero Ullio. Indirect Detection Analysis: Wino Dark Matter Case Study. *Journal of Cosmology and Astroparticle Physics*, 1407:031, 2014. doi: 10.1088/1475-7516/2014/07/031.

[34] T. Aramaki et al. Review of the theoretical and experimental status of dark matter identification with cosmic-ray antideuterons. *Physics Reports*, 618:1 – 37, 2016. ISSN 0370-1573. doi: https://doi.org/10.1016/j.physrep.2016.01.002. URL http://www.sciencedirect.com/science/article/pii/S0370157316000120.

[35] Michael Korsmeier, Fiorenza Donato, and Nicolao Fornengo. Prospects to verify a possible dark matter hint in cosmic antiprotons with antideuterons and antihelium. *Physical Review D*, 97(10):103011, 2018. doi: 10.1103/PhysRevD.97.103011.

[36] Nicola Tomassetti and Alberto Oliva. Production of cosmic-ray antinuclei in the Galaxy and background for dark matter searches. *Proceedings of Science*, EPS-HEP2017:620, 2017. doi: 10.22323/1.314.0620.

[37] Adam Coogan and Stefano Profumo. Origin of the tentative AMS antihelium events. *Physical Review D*, 96(8):083020, 2017. doi: 10.1103/PhysRevD.96.083020.

[38] Su-Jie Lin, Xiao-Jun Bi, and Peng-Fei Yin. Expectations of the Cosmic Antideuteron Flux. , 2018.

[39] Yu-Chen Ding, Nan Li, Chun-Cheng Wei, Yue-Liang Wu, and Yu-Feng Zhou. Prospects of detecting dark matter through cosmic-ray antihelium with the antiproton constraints. *Journal of Cosmology and Astroparticle Physics*, 1906(06):004, 2019. doi: 10.1088/1475-7516/2019/06/004.

[40] Lisa Randall and Weishuang Linda Xu. Searching for dark photon dark matter with cosmic ray antideuterons. *Journal of High Energy Physics*, 2020(5), may 2020. doi: 10.1007/jhep05(2020)081. URL https://doi.org/10.1007%2Fjhep05%282020%29081.

[41] von Doetinchem et al. Cosmic-ray antinuclei as messengers of new physics: status and outlook for the new decade. *Journal of Cosmology and Astroparticle Physics*, 2020(08):035–035, aug 2020. doi: 10.1088/1475-7516/2020/08/035. URL https://doi.org/10.1088/1475-7516/2020/08/035.

[42] M. M. Kachelrieß, S. Ostapchenko, and J. Tjemsland. Revisiting cosmic ray antinuclei fluxes with a new coalescence model. *Journal of Cosmology and Astroparticle Physics*, 2020(08):048–048, aug 2020. doi: 10.1088/1475-7516/2020/08/048. URL https://doi.org/10.1088%2F1475-7516%2F2020%2F08%2F048.

[43] L. Serksnyte et al. Reevaluation of the cosmic antideuteron flux from cosmic-ray interactions and from exotic sources. *Physical Review D*, 105(8), apr 2022. doi: 10.1103/physrevd.105.083021. URL https://doi.org/10.1103%2Fphysrevd.105.083021.

[44] Mario Bertolotti. Celestial messengers. cosmic rays. the story of a scientific adventure, Jul 2013.

[45] Diego Mauricio Gomez Coral. Deuteron and antideuteron production in galactic cosmic-rays. Producción de deuterio y antideuterio en rayos cósmicos galácticos. *CERN CDS*, Mar 2019. URL https://cds.cern.ch/record/2673048. Presented 26 Apr 2019.

[46] Sebastian Hornung. Understanding the background in dark matter searches by studying anti-nucleosynthesis in the laboratory with alice. https://indico.cern.ch/event/868940/contributions/3814851/, 2020. Accessed: 2023-03-21.

[47] H. Fuke et al. Search for Cosmic-Ray Antideuterons. *Physical Review Letters*, 95(8):081101, August 2005. doi: 10.1103/PhysRevLett.95.081101.

[48] K. Abe et al. Search for Antihelium with the BESS-Polar Spectrometer. *Physical Review Letters*, 108(13):131301, March 2012. doi: 10.1103/PhysRevLett.108.131301.

[49] K. Abe et al. Measurement of the Cosmic-Ray Antiproton Spectrum at Solar Minimum with a Long-Duration Balloon Flight over Antarctica. *Physical Review Letters*, 108(5):051102, February 2012. doi: 10.1103/PhysRevLett.108.051102.

[50] O. Adriani et al. Measurement of the flux of primary cosmic ray antiprotons with energies of 60 MeV to 350 GeV in the PAMELA experiment. *Soviet Journal of Experimental and Theoretical Physics Letters*, 96:621–627, January 2013. doi: 10.1134/S002136401222002X.

[51] O. Adriani et al. Ten years of PAMELA in space. *Riv. Nuovo Cim.*, 40(10):473–522, 2017. doi: 10.1393/ncr/i2017-10140-x.

[52] A. W. Strong and I. V. Moskalenko. Propagation of Cosmic-Ray Nucleons in the Galaxy. *Astrophysical Journal*, 509:212–228, December 1998. doi: 10.1086/306470.

[53] M. Aguilar et al. Antiproton Flux, Antiproton-to-Proton Flux Ratio, and Properties of Elementary Particle Fluxes in Primary Cosmic Rays Measured with the Alpha Magnetic Spectrometer on the International Space Station. *Phys. Rev. Lett.*, 117(9): 091103, 2016. doi: 10.1103/PhysRevLett.117.091103.

[54] O. Adriani et al. An anomalous positron abundance in cosmic rays with energies 1.5-100GeV. *Nature*, 458:607–609, April 2009. doi: 10.1038/nature07942.

[55] M. Aguilar et al. First Result from the Alpha Magnetic Spectrometer on the International Space Station: Precision Measurement of the Positron Fraction in Primary Cosmic Rays of 0.5-350 GeV. *Physical Review Letters*, 110:141102, Apr 2013. doi: 10.1103/PhysRevLett.110.141102.

[56] L. Accardo et al. High Statistics Measurement of the Positron Fraction in Primary Cosmic Rays of 0.5-500 GeV with the Alpha Magnetic Spectrometer on the International Space Station. *Physical Review Letters*, 113:121101, Sep 2014. doi: 10.1103/PhysRevLett.113.121101.

[57] M. Ackermann et al. Measurement of Separate Cosmic-Ray Electron and Positron Spectra with the Fermi Large Area Telescope. *Physical Review Letters*, 108(1):011103, January 2012. doi: 10.1103/PhysRevLett.108.011103.

[58] Aguilar et al. Electron and Positron Fluxes in Primary Cosmic Rays Measured with the Alpha Magnetic Spectrometer on the International Space Station. *Physical Review Letters*, 113:121102, Sep 2014. doi: 10.1103/PhysRevLett.113.121102.

[59] I. V. Moskalenko and A. W. Strong. Production and Propagation of Cosmic-Ray Positrons and Electrons. *Astrophysical Journal*, 493:694, January 1998. doi: 10.1086/305152.

[60] M. Boudaud, S. Aupetit, S. Caroff, A. Putze, G. Belanger, Y. Genolini, C. Goy, V. Poireau, V. Poulin, S. Rosier, et al. A new look at the cosmic ray positron fraction. *Astronomy & Astrophysics*, 575:A67, March 2015. doi: 10.1051/0004-6361/201425197.

[61] R. L. Workman et al. Review of Particle Physics. *PTEP*, 2022:083C01, 2022. doi: 10.1093/ptep/ptac097. URL https://pdg.lbl.gov/2022/reviews/rpp2022-rev-cosmic-rays.pdf.

[62] Aguilar et al. Antiproton flux, antiproton-to-proton flux ratio, and properties of elementary particle fluxes in primary cosmic rays measured with the alpha magnetic spectrometer on the international space station. *Phys. Rev. Lett.*, 117:091103, Aug 2016. doi: 10.1103/PhysRevLett.117.091103. URL https://link.aps.org/doi/10.1103/PhysRevLett.117.091103.

[63] PAMELA Collaboration. PAMELA Results on the Cosmic-Ray Antiproton Flux from 60 MeV to 180 GeV in Kinetic Energy. *Physical Review Letters*, 105(12):121101, September 2010. doi: 10.1103/PhysRevLett.105.121101.

[64] Marco Cirelli and Gaelle Giesen. Antiprotons from Dark Matter: Current constraints and future sensitivities. *Journal of Cosmology and Astroparticle Physics*, 1304:015, 2013. doi: 10.1088/1475-7516/2013/04/015.

[65] Timur Delahaye and Michael Grefe. Antiproton limits on decaying gravitino dark matter. *Journal of Cosmology and Astroparticle Physics*, 1312:045, 2013. doi: 10.1088/1475-7516/2013/12/045.

[66] Ming-Yang Cui, Qiang Yuan, Yue-Lin Sming Tsai, and Yi-Zhong Fan. Possible dark matter annihilation signal in the AMS-02 antiproton data. *Physical Review Letters*, 118(19):191101, 2017. doi: 10.1103/PhysRevLett.118.191101.

[67] Alessandro Cuoco, Michael Krämer, and Michael Korsmeier. Novel Dark Matter Constraints from Antiprotons in Light of AMS-02. *Physical Review Letters*, 118(19): 191102, 2017. doi: 10.1103/PhysRevLett.118.191102.

[68] Annika Reinert and Martin Wolfgang Winkler. A Precision Search for WIMPs with Charged Cosmic Rays. *JCAP*, 01:055, 2018. doi: 10.1088/1475-7516/2018/01/055.

[69] Alessandro Cuoco, Jan Heisig, Lukas Klamt, Michael Korsmeier, and Michael Krämer. Scrutinizing the evidence for dark matter in cosmic-ray antiprotons. *Physical Review D*, 99(10):103014, 2019. doi: 10.1103/PhysRevD.99.103014.

[70] Ilias Cholis, Tim Linden, and Dan Hooper. A Robust Excess in the Cosmic-Ray Antiproton Spectrum: Implications for Annihilating Dark Matter. *Phys. Rev. D*, 99 (10):103026, 2019. doi: 10.1103/PhysRevD.99.103026.

[71] Mathieu Boudaud, Yoann Génolini, Laurent Derome, Julien Lavalle, David Maurin, Pierre Salati, and Pasquale D. Serpico. AMS-02 antiprotons' consistency with a secondary astrophysical origin. *Phys. Rev. Res.*, 2(2):023022, 2020. doi: 10.1103/PhysRevResearch.2.023022.

[72] Jan Heisig, Michael Korsmeier, and Martin Wolfgang Winkler. Dark matter or correlated errors: Systematics of the AMS-02 antiproton excess. *Phys. Rev. Res.*, 2(4):043017, 2020. doi: 10.1103/PhysRevResearch.2.043017.

[73] T. Aramaki et al. Review of the theoretical and experimental status of dark matter identification with cosmic-ray antideuterons. *Physics Reports*, 618:1–37, 2016. ISSN 0370-1573. doi: https://doi.org/10.1016/j.physrep.2016.01.002. URL https://www.sciencedirect.com/science/article/pii/S0370157316000120.

[74] A. Boveia et al. Snowmass 2021 cross frontier report: Dark matter complementarity (extended version), 2022. URL https://arxiv.org/abs/2210.01770.

[75] Alessandro Cuoco, Jan Heisig, Michael Korsmeier, and Michael Krämer. Probing dark matter annihilation in the Galaxy with antiprotons and gamma rays. *Journal of Cosmology and Astroparticle Physics*, 1710(10):053, 2017. doi: 10.1088/1475-7516/2017/10/053.

[76] Martin Wolfgang Winkler, Pedro De La Torre Luque, and Tim Linden. Cosmic ray antihelium from a strongly coupled dark sector, 2022. URL https://arxiv.org/abs/2211.00025.

[77] Kenichi Sakai et al. New result of Antideuteron search in BESS-Polar II. *PoS*, ICRC2021:123, 2021. doi: 10.22323/1.395.0123.

[78] Shreyasi Acharya et al. Production of deuterons, tritons, ^{3}He nuclei and their antinuclei in pp collisions at $\sqrt{s} = 0.9$, 2.76 and 7 TeV. *Phys. Rev. C*, 97(2):024615, 2018. doi: 10.1103/PhysRevC.97.024615.

[79] T. Aramaki et al. Potential for Precision Measurement of Low-Energy Antiprotons with GAPS for Dark Matter and Primordial Black Hole Physics. *Astropart. Phys.*, 59:12–17, 2014. doi: 10.1016/j.astropartphys.2014.03.011.

[80] T. Aramaki et al. Antideuteron Sensitivity for the GAPS Experiment. *Astropart. Phys.*, 74:6–13, 2016. doi: 10.1016/j.astropartphys.2015.09.001.

[81] N. Saffold et al. Cosmic antihelium-3 nuclei sensitivity of the GAPS experiment. *Astropart. Phys.*, 130:102580, 2021. doi: 10.1016/j.astropartphys.2021.102580.

[82] S. Ting. The First Five Years of the Alpha Magnetic Spectrometer on the International Space Station. *Press Conference at CERN, December 8*, 2016.

[83] S. Ting. Latest Results from the AMS Experiment on the International Space Station. *Colloquium at CERN, May 24*, 2018.

[84] A. Kounine. AMS Experiment on the International Space Station. *Next Generation of AstroParticle Experiments in Space (NextGAPES-2019) http://www.sinp.msu.ru/contrib/NextGAPES/files/AMS_AK.pdf, June 21*, 2019.

[85] A. Oliva. Observations of cosmic-rays and search for anti-nuclei with AMS-02. *https://indico.cern.ch/event/849055/contributions/3598085/attachments/1925619/3187261/01_LAN2019_-_Observations_of_cosmic-rays_and_search_for_anti-nuclei_with_AMS-02_-_A._Oliva.pdf, October 14*, 2019.

[86] Vitali Choutko. Cosmic Heavy Anti-Matter. In *44th COSPAR Scientific Assembly. Held 16-24 July*, volume 44, page 2083, July 2022.

[87] Andrei Kounine. The Latest Results from the Alpha Magnetic Spectrometer. *PoS*, EPS-HEP2019:028, 2020. doi: 10.22323/1.364.0028.

[88] F. C. Adams et al. Constraints on the intergalactic transport of cosmic rays. *Astrophysical Journal*, 491:6–12, 1997. doi: 10.1086/304962.

[89] Andrew G. Cohen, A. De Rujula, and S.L. Glashow. A Matter - antimatter universe? *Astrophysical Journal*, 495:539–549, 1998. doi: 10.1086/305328.

[90] K. Blum et al. Cosmic rays, antihelium, and an old navy spotlight. *Physical Review D*, 96(10):103021, 2017. doi: 10.1103/PhysRevD.96.103021.

[91] Vivian Poulin, Pierre Salati, Ilias Cholis, Marc Kamionkowski, and Joseph Silk. Where do the ams-02 antihelium events come from? *Phys. Rev. D*, 99:023016, Jan 2019. doi: 10.1103/PhysRevD.99.023016. URL https://link.aps.org/doi/10.1103/PhysRevD.99.023016.

[92] D. Gomez-Coral et al. Deuteron and Antideuteron Production Simulation in Cosmic-Ray Interactions. *Physical Review D*, 98(2):023012, 2018. doi: 10.1103/PhysRevD.98.023012.

[93] A. Shukla et al. Large-scale simulations of antihelium production in cosmic-ray interactions. *Physical Review D*, 102(6), Sep 2020. ISSN 2470-0029. doi: 10.1103/physrevd.102.063004. URL http://dx.doi.org/10.1103/PhysRevD.102.063004.

[94] T. Massam, Th. Muller, B. Righini, M. Schneegans, and A. Zichichi. Experimental observation of antideuteron production. *Il Nuovo Cimento*, 39(1):10–14, 1965. ISSN 0029-6341. doi: 10.1007/BF02814251.

[95] D. E. Dorfan, J. Eades, L. M. Lederman, W. Lee, and C. C. Ting. Observation of Antideuterons. *Physical Review Letters*, 14:1003–1006, Jun 1965. doi: 10.1103/PhysRevLett.14.1003.

[96] H. C. Urey, F. G. Brickwedde, and G. M. Murphy. A Hydrogen Isotope of Mass 2. *Physical Review*, 39:164–165, January 1932. doi: 10.1103/PhysRev.39.164.

[97] S. T. Butler and C. A. Pearson. Deuterons from High-Energy Proton Bombardment of Matter. *Physical Review Letters*, 7:69–71, Jul 1961. doi: 10.1103/PhysRevLett.7.69.

[98] S.T. Butler and C.A. Pearson. Deuterons from high-energy proton bombardment of matter. *Physics Letters*, 1(3):77 – 81, 1962. ISSN 0031-9163. doi: http://dx.doi.org/10.1016/0031-9163(62)90274-3.

[99] S. T. Butler and C. A. Pearson. Deuterons from high-energy proton bombardment of matter. *Phys. Rev.*, 129:836–842, Jan 1963. doi: 10.1103/PhysRev.129.836. URL https://link.aps.org/doi/10.1103/PhysRev.129.836.

[100] A. Schwarzschild and Č. Zupančič. Production of Tritons, Deuterons, Nucleons, and Mesons by 30-GeV Protons on A1, Be, and Fe Targets. *Physical Review*, 129:854–862, Jan 1963. doi: 10.1103/PhysRev.129.854.

[101] Jehanne Simon-Gillo et al. Deuteron and anti-deuteron production in CERN experiment NA44. *Nucl. Phys. A*, 590:483C–486C, 1995. doi: 10.1016/0375-9474(95)00259-4.

[102] T.A. Armstrong et al. Anti-deuteron yield at the AGS and coalescence implications. *Phys. Rev. Lett.*, 85:2685–2688, 2000. doi: 10.1103/PhysRevLett.85.2685.

[103] S.V. Afanasiev et al. Deuteron production in central Pb + Pb collisions at 158-A-GeV. *Phys. Lett. B*, 486:22–28, 2000. doi: 10.1016/S0370-2693(00)00746-2.

[104] T. Anticic et al. Energy and centrality dependence of deuteron and proton production in Pb + Pb collisions at relativistic energies. *Phys. Rev. C*, 69:024902, 2004. doi: 10.1103/PhysRevC.69.024902.

[105] S.S. Adler et al. Deuteron and antideuteron production in Au + Au collisions at s(NN)**(1/2) = 200-GeV. *Phys. Rev. Lett.*, 94:122302, 2005. doi: 10.1103/PhysRevLett.94.122302.

[106] B. Alper et al. Large angle production of stable particles heavier than the proton and a search for quarks at the CERN intersecting storage rings. *Physics Letters B*, 46:265–268, September 1973. doi: 10.1016/0370-2693(73)90700-4.

[107] W. M. Gibson et al. Production of deuterons and antideuterons in proton-proton collisions at the CERN ISR. *Lettere al Nuovo Cimento*, 21(6):189–194, 1978. ISSN 0375-930X. doi: 10.1007/BF02822248.

[108] T. Alexopoulos et al. Cross sections for deuterium, tritium, and helium production in $\overline{p}p$ collisions at $\sqrt{s} = 1.8$ tev. *Phys. Rev. D*, 62:072004, Sep 2000. doi: 10.1103/PhysRevD.62.072004. URL https://link.aps.org/doi/10.1103/PhysRevD.62.072004.

[109] A. Aktas et al. Measurement of anti-deuteron photoproduction and a search for heavy stable charged particles at HERA. *Eur. Phys. J. C*, 36:413–423, 2004. doi: 10.1140/epjc/s2004-01978-x.

[110] D.M. Asner et al. Anti-deuteron production in Upsilon(nS) decays and the nearby continuum. *Phys. Rev. D*, 75:012009, 2007. doi: 10.1103/PhysRevD.75.012009.

[111] S. Schael et al. Deuteron and anti-deuteron production in e+ e- collisions at the Z resonance. *Phys. Lett. B*, 639:192–201, 2006. doi: 10.1016/j.physletb.2006.06.043.

[112] Jaroslav Adam et al. Production of light nuclei and anti-nuclei in pp and Pb-Pb collisions at energies available at the CERN Large Hadron Collider. *Phys. Rev. C*, 93(2):024917, 2016. doi: 10.1103/PhysRevC.93.024917.

[113] Jaroslav Adam et al. ${}^{3}_{\Lambda}\mathrm{H}$ and ${}^{3}_{\Lambda}\overline{\mathrm{H}}$ production in Pb–Pb collisions at $\sqrt{s_{\mathrm{NN}}} = 2.76$ TeV. *Phys. Lett.*, B754:360–372, 2016. doi: 10.1016/j.physletb.2016.01.040.

[114] Shreyasi Acharya et al. Measurement of deuteron spectra and elliptic flow in Pb–Pb collisions at $\sqrt{s_{\mathrm{NN}}} = 2.76$ TeV at the LHC. *Eur. Phys. J.*, C77(10):658, 2017. doi: 10.1140/epjc/s10052-017-5222-x.

[115] Shreyasi Acharya et al. Multiplicity dependence of (anti-)deuteron production in pp collisions at $\sqrt{s} = 7$ TeV. *Phys. Lett. B*, 794:50–63, 2019. doi: 10.1016/j.physletb.2019.05.028.

[116] H. Agakishiev et al. Observation of the antimatter helium-4 nucleus. *Nature*, 473:353, 2011. doi: 10.1038/nature10079.

[117] B. I. Abelev et al. Observation of an Antimatter Hypernucleus. *Science*, 328:58–62, 2010. doi: 10.1126/science.1183980.

[118] Jaroslav Adam et al. Precision measurement of the mass difference between light nuclei and anti-nuclei. *Nature Phys.*, 11(10):811–814, 2015. doi: 10.1038/nphys3432.

[119] Jaroslav Adam et al. Measurement of the mass difference and the binding energy of the hypertriton and antihypertriton. *Nature Phys.*, 16(4):409–412, 2020. doi: 10.1038/s41567-020-0799-7.

[120] Shreyasi Acharya et al. Measurement of the low-energy antideuteron inelastic cross section. *Phys. Rev. Lett.*, 125(16):162001, 2020. doi: 10.1103/PhysRevLett.125.162001.

[121] N. Abgrall et al. NA61/SHINE facility at the CERN SPS: beams and detector system. *Journal of Instrumentation*, 9:6005P, June 2014. doi: 10.1088/1748-0221/9/06/P06005.

[122] S. Acharya et al. Measurement of anti-3he nuclei absorption in matter and impact on their propagation in the galaxy. *Nature Physics*, 19(1):61–71, dec 2022. doi: 10.1038/s41567-022-01804-8. URL https://doi.org/10.1038%2Fs41567-022-01804-8.

[123] Martin Wolfgang Winkler and Tim Linden. Response to comment on "Dark matter annihilation can produce a detectable antihelium flux through $\bar{\Lambda}_b$ decays", 2021.

[124] J. Cooley et al. Report of the topical group on particle dark matter for snowmass 2021, 2022. URL https://arxiv.org/abs/2209.07426.

[125] Rudiger Scheibl and Ulrich W. Heinz. Coalescence and flow in ultrarelativistic heavy ion collisions. *Physical Review C*, 59:1585–1602, 1999. doi: 10.1103/PhysRevC.59.1585.

[126] M. Kachelrieß, S. Ostapchenko, and J. Tjemsland. Alternative coalescence model for deuteron, tritium, helium-3 and their antinuclei. *European Physical Journal A*, 56(1):4, 2020. doi: 10.1140/epja/s10050-019-00007-9.

[127] M. Kachelrieß, S. Ostapchenko, and J. Tjemsland. On nuclear coalescence in small interacting systems. *The European Physical Journal A*, 57(5), may 2021. doi: 10.1140/epja/s10050-021-00469-w. URL https://doi.org/10.1140%2Fepja%2Fs10050-021-00469-w.

[128] F. Becattini and Ulrich W. Heinz. Thermal hadron production in p p and p anti-p collisions. *Zeitschrift für Physik C Particles and Fields C*, 76:269–286, 1997. doi: 10.1007/s002880050551. [Erratum: Z. Phys.C76,578(1997)].

[129] A. Andronic, P. Braun-Munzinger, J. Stachel, and H. Stöcker. Production of light nuclei, hypernuclei and their antiparticles in relativistic nuclear collisions . *Physics Letters B*, 697(3):203 – 207, 2011. ISSN 0370-2693. doi: http://dx.doi.org/10.1016/j.physletb.2011.01.053.

[130] J. Cleymans, S. Kabana, I. Kraus, H. Oeschler, K. Redlich, and N. Sharma. Antimatter production in proton-proton and heavy-ion collisions at ultrarelativistic energies. *Physical Review C*, 84(5):054916, November 2011. doi: 10.1103/PhysRevC.84.054916.

[131] Francesca Bellini and Alexander Philipp Kalweit. Testing production scenarios for (anti-)(hyper-)nuclei and exotica at energies available at the CERN Large Hadron Collider. *Phys. Rev. C*, 99(5):054905, 2019. doi: 10.1103/PhysRevC.99.054905.

[132] Raghunath Sahoo. Relativistic kinematics, 2016.

[133] Peter Braun-Munzinger and Benjamin Dönigus. Loosely-bound objects produced in nuclear collisions at the LHC. *Nucl. Phys. A*, 987:144–201, 2019. doi: 10.1016/j.nuclphysa.2019.02.006.

[134] M. Floris. Hadron yields and the phase diagram of strongly interacting matter . *Nuclear Physics A*, 931(0):103 – 112, 2014. ISSN 0375-9474. doi: http://dx.doi.org/10.1016/j.nuclphysa.2014.09.002.

[135] S. Acharya et al. (ALICE Collaboration). Production of deuterons, tritons, ^{3}He nuclei and their antinuclei in pp collisions at $\sqrt{s} = 0.9$, 2.76 and 7 TeV. *Physical Review C*, 97(2):024615, 2018. doi: 10.1103/PhysRevC.97.024615.

[136] Pascal Chardonnet, Jean Orloff, and Pierre Salati. The production of anti-matter in our galaxy. *Physics Letters B*, 409(1-4):313–320, Sep 1997. ISSN 0370-2693. doi: 10.1016/s0370-2693(97)00870-8. URL http://dx.doi.org/10.1016/s0370-2693(97)00870-8.

[137] Alejandro Ibarra and Sebastian Wild. Determination of the cosmic antideuteron flux in a monte carlo approach, 2013.

[138] Alejandro Ibarra and Sebastian Wild. Prospects of antideuteron detection from dark matter annihilations or decays at ams-02 and gaps, 2012.

[139] Mario Kadastik, Martti Raidal, and Alessandro Strumia. Enhanced anti-deuteron dark matter signal and the implications of pamela, 2009.

[140] T. Pierog, Iu. Karpenko, J. M. Katzy, E. Yatsenko, and K. Werner. EPOS LHC: Test of collective hadronization with data measured at the CERN Large Hadron Collider. *Physical Review C*, 92(3):034906, 2015. doi: 10.1103/PhysRevC.92.034906.

[141] Sergey Ostapchenko. QGSJET-II: Results for extensive air showers. *Nuclear Physics B - Proceedings Supplements*, 151:147–150, 2006. doi: 10.1016/j.nuclphysbps.2005.07.027.

[142] Torbjorn Sjostrand, Stephen Mrenna, and Peter Z. Skands. A Brief Introduction to PYTHIA 8.1. *Computer Physics Communications*, 178:852–867, 2008. doi: 10.1016/j.cpc.2008.01.036.

[143] Agostinelli et al. Geant4—a simulation toolkit . *Nuclear Instruments and Methods in Physics Research A*, 506(3):250 – 303, 2003. ISSN 0168-9002. doi: http://dx.doi.org/10.1016/S0168-9002(03)01368-8.

[144] Allison et al. Geant4 developments and applications. *IEEE Transactions on Nuclear Science*, 53:270–278, February 2006. doi: 10.1109/TNS.2006.869826.

[145] A. Galoyan and V. Uzhinsky. Simulation of Light Antinucleus-Nucleus Interactions. *Hyperfine Interaction*, 215(1-3):69–76, 2013. doi: 10.1007/s10751-013-0780-2.

[146] Eun-Joo Ahn, Ralph Engel, Thomas K. Gaisser, Paolo Lipari, and Todor Stanev. Cosmic ray interaction event generator SIBYLL 2.1. *Physical Review D*, 80:094003, 2009. doi: 10.1103/PhysRevD.80.094003.

[147] Mario Kadastik, Martti Raidal, and Alessandro Strumia. Enhanced anti-deuteron Dark Matter signal and the implications of PAMELA. *Physics Letters B*, 683:248–254, 2010. doi: 10.1016/j.physletb.2009.12.005.

[148] M. Tanabashi et al. Review of particle physics. *Phys. Rev. D*, 98:424, Aug 2018. doi: 10.1103/PhysRevD.98.030001. URL https://link.aps.org/doi/10.1103/PhysRevD.98.030001.

[149] Michael Korsmeier, Fiorenza Donato, and Mattia Di Mauro. Production cross sections of cosmic antiprotons in the light of new data from the NA61 and LHCb experiments. *Physical Review D*, 97(10):103019, 2018. doi: 10.1103/PhysRevD.97.103019.

[150] R. P. Duperray, C.-Y. Huang, K. V. Protasov, and M. Buénerd. Parametrization of the antiproton inclusive production cross section on nuclei. *Phys. Rev. D*, 68:094017, Nov 2003. doi: 10.1103/PhysRevD.68.094017. URL https://link.aps.org/doi/10.1103/PhysRevD.68.094017.

[151] T. Pierog, C. Baus, and R. Ulrich. CRMC (Cosmic Ray Monte Carlo package). web.ikp.kit.edu/rulrich/crmc.html, 2020.

[152] Carina Kanitz. Coalescence of light antinuclei - presentation at uh manoa, 2018. Accessed: 2023-03-21.

[153] John W. Norbury and Lawrence W. Townsend. Parameterized total cross sections for pion production in nuclear collisions. *Nuclear Instruments and Methods in Physics Research Section B: Beam Interactions with Materials and Atoms*, 254(2):187–192, jan 2007. doi: 10.1016/j.nimb.2006.11.054. URL https://doi.org/10.1016%2Fj.nimb.2006.11.054.

[154] T. Anticic, B. Baatar, J. Bartke, L. Betev, H. Białkowska, C. Blume, B. Boimska, J. Bracinik, and V. et al. Cerny. Inclusive production of protons, anti-protons and neutrons in p+p collisions at 158 gev/c beam momentum. *The European Physical Journal C*, 65(1-2), Nov 2009. ISSN 1434-6052. doi: 10.1140/epjc/s10052-009-1172-2. URL http://dx.doi.org/10.1140/epjc/s10052-009-1172-2.

[155] M. Antinucci, A. Bertin, and P. Capiluppi. Multiplicities of charged particles up to isr energies. *Lett. Nuovo Cim. 6: No. 4, 121-128(27 Jan 1973).*, 1 1973. doi: 10.1007/BF02827250.

[156] Martin Wolfgang Winkler. Cosmic ray antiprotons at high energies, 2017.

[157] M. di Mauro et al. New evaluation of the antiproton production cross section for cosmic ray studies. *Phys. Rev. D*, 90:085017, Oct 2014. doi: 10.1103/PhysRevD.90.085017.

[158] W. Bozzoli, A. Bussière, G. Giacomelli, E. Lesquoy, R. Meunier, L. Moscoso, A. Muller, F. Rimondi, and S. Zylberajch. Production of d, t, 3he, d, t and 3he by 200 gev protons. *Nuclear Physics B*, 144(2):317 – 328, 1978. ISSN "0550-3213. doi: https://doi.org/10.1016/0550-3213(78)90373-5. URL http://www.sciencedirect.com/science/article/pii/0550321378903735.

[159] W.F. Baker et al. Measurement of pi, k, p and pbar production by 200 and 300 gev/c protons. *Physics Letters B*, 51(3):303 – 305, 1974. ISSN 0370-2693. doi: https://doi.org/10.1016/0370-2693(74)90297-4. URL http://www.sciencedirect.com/science/article/pii/0370269374902974.

[160] Jie Feng Alberto Oliva, Nicola Tomassetti. Production of antimatter nuclei in galactic cosmic rays. *35th International Cosmic Ray Conference - ICRC2017*, July 2018. doi: arXiv:1707.06918v2. URL https://arxiv.org/abs/1707.06918v2.

[161] S Acharya et al. Production of deuterons, tritons, ^{3}He nuclei, and their antinuclei in pp collisions at $\sqrt{s} = 0.9$, 2.76, and 7 tev. *Phys. Rev. C*, 97:024615, Feb 2018. doi: 10.1103/PhysRevC.97.024615.

[162] Yu-Chen Ding et al. Prospects of detecting dark matter through cosmic-ray antihelium with the antiproton constraints. *Journal of Cosmology and Astroparticle Physics*, page 004–004, Jun 2019. ISSN 1475-7516. doi: 10.1088/1475-7516/2019/06/004.

[163] ALICE Collaboration. (anti-)deuteron production in pp collisions at $\sqrt{s}$ = 13 tev, 2020.

[164] S. Acharya et al. (ALICE Collaboration). Production of 4he and 4he-bar in pb–pb collisions at snn=2.76tev at the lhc. *Nuclear Physics A*, 971:1–20, Mar 2018. ISSN 0375-9474. doi: 10.1016/j.nuclphysa.2017.12.004.

[165] S. Acharya et al. (ALICE Collaboration). Production of (anti-)he3 and (anti-)h3 in p-pb collisions at snn=5.02 tev. *Physical Review C*, 101(4), Apr 2020. ISSN 2469-9993. doi: 10.1103/physrevc.101.044906.

[166] Oleksandra Panova and Maciej Lewicki. System size and energy dependence of proton rapidity spectra from NA61/SHINE at the CERN SPS. *EPJ Web of Conferences*, 274: 05004, 2022. doi: 10.1051/epjconf/202227405004.

[167] P Braun-Munzinger et al. Particle production in heavy ion collisions. *Quark–Gluon Plasma 3, World Scientific Publishing*, pages 491–599, jan 2004. doi: 10.1142/9789812795533_0008.

[168] Ulrich W. Heinz. Concepts of heavy-ion physics, 2004.

[169] E. N. Parker. The passage of energetic charged particles through interplanetary space. *Planetary and Space Science*, 13(1):9–49, January 1965. doi: 10.1016/0032-0633(65)90131-5.

[170] L. J. Gleeson and W. I. Axford. Solar Modulation of Galactic Cosmic Rays. *Astrophys. J.*, 154:1011, 1968. doi: 10.1086/149822.

[171] M.J. Boschini, S. Della Torre, M. Gervasi, G. La Vacca, and P.G. Rancoita. Propagation of cosmic rays in heliosphere: The helmod model. *Advances in Space Research*, 62(10):2859–2879, 2018. ISSN 0273-1177. doi: https://doi.org/10.1016/j.asr.2017.04.017. URL https://www.sciencedirect.com/science/article/pii/S0273117717302971.

[172] M. J. Boschini et al. The helmod model in the works for inner and outer heliosphere: From ams to voyager probes observations. *Advances in Space Research*, 64(12):2459–2476, 2019. ISSN 0273-1177. doi: https://doi.org/10.1016/j.asr.2019.04.007.

[173] K. Blum et al. Cosmic rays, antihelium, and an old navy spotlight. *Phys. Rev. D*, 96:103021, Nov 2017. doi: 10.1103/PhysRevD.96.103021. URL https://link.aps.org/doi/10.1103/PhysRevD.96.103021.

[174] R. P. Duperray et al. Antideuteron production in proton-proton and proton-nucleus collisions. *The European Physical Journal A - Hadrons and Nuclei Volume 16 pages 27–34*, 2003. doi: 10.1140/epja/i2002-10074-0.

[175] F. Donato et al. Antiprotons in cosmic rays from neutralino annihilation. *Physical Review D*, 69(6), Mar 2004. ISSN 1550-2368. doi: 10.1103/physrevd.69.063501. URL http://dx.doi.org/10.1103/PhysRevD.69.063501.

[176] M. Boudaud et al. A fussy revisitation of antiprotons as a tool for dark matter searches. *Journal of Cosmology and Astroparticle Physics*, 2015(05):013–013, May 2015. ISSN 1475-7516. doi: 10.1088/1475-7516/2015/05/013.

[177] G. Gaëlle et al. Ams-02 antiprotons, at last! secondary astrophysical component and immediate implications for dark matter. *Journal of Cosmology and Astroparticle Physics*, 2015(09):023–023, Sep 2015. ISSN 1475-7516. doi: 10.1088/1475-7516/2015/09/023.

[178] M. Kachelrieß, S. Ostapchenko, and J. Tjemsland. Alternative coalescence model for deuteron, tritium, helium-3 and their antinuclei. *Eur. Phys. J. A*, 56(1):4, 2020. doi: 10.1140/epja/s10050-019-00007-9.

[179] M. Kachelrieß, S. Ostapchenko, and J. Tjemsland. Revisiting cosmic ray antinuclei fluxes with a new coalescence model. *JCAP*, 08:048, 2020. doi: 10.1088/1475-7516/2020/08/048.

[180] V.V. Abramov et al. Production of deuterons and antideuterons with large p_T in pp and pA collisions at 70 GeV. *Soviet Journal of Nuclear Physics*, 45:5:845–851, 1987.

[181] A. Aduszkiewicz et al. Measurements of $\pi^{\pm}$, $K^{\pm}$, p and $\bar{p}$ spectra in proton-proton interactions at 20, 31, 40, 80 and 158 GeV/c with the NA61/SHINE spectrometer at the CERN SPS. *European Physical Journal C*, 77(10):671, 2017. doi: 10.1140/epjc/s10052-017-5260-4.

[182] Szymon Pulawski. Identification and analysis of charged hadrons in p+p interactions from NA61/SHINE experiment at CERN SPS energies. *CERN CDS*, 2015. URL https://cds.cern.ch/record/2240156.

[183] M. Kachelrieß et al. Aafrag: Interpolation routines for monte carlo results on secondary production in proton–proton, proton–nucleus and nucleus–nucleus interactions. *Computer Physics Communications*, 245:106846, 2019. ISSN 0010-4655. doi: https://doi.org/10.1016/j.cpc.2019.08.001.

[184] N. Abgrall et al. NA61/SHINE facility at the CERN SPS: beams and detector system. *JINST*, 9:P06005, 2014. doi: 10.1088/1748-0221/9/06/P06005.

[185] ALICE. Poster ALICE Time Projection Chamber, 2002.

[186] A. Aduszkiewicz. School on Cosmic Matter in Heavy-Ion Collision Laboratories in Ladek Zdroj, 2012.

[187] C. Strabel. Eth-19538, cern-thesis-2011-295, 2011.

[188] C. Bovet et al. *The CEDAR counters for particle identification in the SPS secondary beams: a description and an operation manual*. CERN Yellow Reports: Monographs. CERN, Geneva, 1982. doi: 10.5170/CERN-1982-013.

[189] N. Abgrall et al. Measurement of negatively charged pion spectra in inelastic p+p interactions at p_{lab} = 20, 31, 40, 80 and 158 GeV/c. *Eur.Phys.J.*, C74:2794, 2014. doi: 10.1140/epjc/s10052-014-2794-6.

[190] Maciej Piotr Lewicki. Charged hadron production in central Ar+Sc collisions at the CERN SPS. *CERN CDS*, 2020. URL https://cds.cern.ch/record/2772291. Presented 22 Jan 2021.

[191] Klaus Werner. The hadronic interaction model EPOS. *Nucl. Phys. B Proc. Suppl.*, 175-176:81–87, 2008. doi: 10.1016/j.nuclphysbps.2007.10.012.

[192] René et al. Brun. *GEANT: Detector Description and Simulation Tool; Oct 1994*. CERN Program Library. CERN, Geneva, 1993. doi: 10.17181/CERN.MUHF.DMJ1. URL https://cds.cern.ch/record/1082634. Long Writeup W5013.

[193] Piotr Podlaski. Study of charged hadron production with tof-dE/dx identification method in central Ar+Sc collisions in NA61/SHINE experiment at CERN. *CERN CDS*, 2021. URL https://cds.cern.ch/record/2799198. Figure 5.7.

[194] M. van Leeuwen. Energy dependence of particle production in nucleus nucleus collisions at the CERN SPS. *XXXVIIIth Rencontres de Moriond, QCD and High Energy Hadronic Interactions*, 2003.

[195] M. van Leeuwen. A practical guide to de/dx analysis in na49, 2008.

[196] S. Afanasev et al. The NA49 large acceptance hadron detector. *Nucl.Instrum.Meth.*, A430:210–244, 1999. doi: 10.1016/S0168-9002(99)00239-9.

[197] A. Rustamov and M.I. Gorenstein. Identity Method for Moments of Multiplicity Distribution. *Phys.Rev.*, C86:044906, 2012. doi: 10.1103/PhysRevC.86.044906.

[198] Jeremy Orloff and Jonathan Bloom. Bootstrap confidence intervals, class 24, 18.05, 2018. URL https://math.mit.edu/~dav/05.dir/class24-prep-a.pdf.

[199] A. Aduszkiewicz et al. Production of Λ -hyperons in inelastic p+p interactions at 158 GeV/*c*. *Eur. Phys. J.*, C76(4):198, 2016. doi: 10.1140/epjc/s10052-016-4003-2.

[200] A Aduszkiewicz. Report from the NA61/SHINE experiment at the CERN SPS. *CERN CDS*, 2017. doi: 10.17181/CERN.0KV8.20KE. URL https://cds.cern.ch/record/2287091.

[201] C. Alt et al. Inclusive production of charged pions in pp collisions at 158 GeV/c beam momentum. *The European Physical Journal C*, 45(2):343–381, dec 2005. doi: 10.1140/epjc/s2005-02391-9. URL https://doi.org/10.1140%2Fepjc%2Fs2005-02391-9.

[202] Michael Haug. Measurement of the cross section of Pion-Carbon interactions using the NA61 detector. *CERN CDS*, 2012. URL https://cds.cern.ch/record/2240129.

[203] R. Sina, V. Ptuskin, and E. S. Seo. The Flux of Cosmic-Ray Deuterons in Simplified Propagation Models. *International Cosmic Ray Conference*, 4:1973, July 2003.

[204] Nicola Tomassetti and Jie Feng. The curious case of high-energy deuterons in galactic cosmic rays. *The Astrophysical Journal*, 835(2):L26, jan 2017. doi: 10.3847/2041-8213/835/2/l26.

[205] Diego Mauricio Gomez-Coral, Cory Gerrity, Riccardo Munini, and Philip von Doetinchem. Current status and new perspectives on cosmic ray deuterons, 2023.

[206] J. P. Meyer. Deuterons and He$\hat{}${3} formation and destruction in proton induced spallation of light nuclei (Z ¡= 8). *A&AS*, 7:417, December 1972.

[207] S. Afanasiev et al. The NA49 large acceptance hadron detector. *Nucl. Instrum. Meth. A*, 430:210–244, 1999. doi: 10.1016/S0168-9002(99)00239-9.

[208] T. Anticic et al. Antideuteron and deuteron production in midcentral Pb+Pb collisions at 158A GeV. *Physical Review C*, 85(4):044913, April 2012. doi: 10.1103/PhysRevC.85.044913.

[209] R. P. Duperray et al. Parametrization of the antiproton inclusive production cross section on nuclei. *Phys. Rev. D*, 68:094017, Nov 2003. doi: 10.1103/PhysRevD.68.094017. URL http://link.aps.org/doi/10.1103/PhysRevD.68.094017.

[210] R. L. Workman et al. Review of Particle Physics. *PTEP*, 2022:083C01, 2022. doi: 10.1093/ptep/ptac097.

[211] Piotr Podlaski. Study of charged hadron production with tof-dE/dx identification method in central Ar+Sc collisions in NA61/SHINE experiment at CERN. *CERN CDS*, 2021. URL https://cds.cern.ch/record/2799198. Section 5.3.2 pp 51-53.

[212] M et al. Gazdzicki. Report from the NA61/SHINE experiment at the CERN SPS. *CERN CDS*, 2019. doi: 10.17181/CERN.E3JY.7Z6E.

[213] A. Seryakov. Energy scan of correlations in p+p and be+be from NA61/SHINE. *Journal of Physics*, 668:012077, jan 2016. doi: 10.1088/1742-6596/668/1/012077.

[214] M. Gazdzicki et al. Particle-set identification method to study multiplicity fluctuations. *Nuclear Physics A*, 1001:121915, sep 2020. doi: 10.1016/j.nuclphysa.2020.121915.

[215] S. Acharya et al. Search for a common baryon source in high-multiplicity pp collisions at the LHC. *Physics Letters B*, 811:135849, dec 2020. doi: 10.1016/j.physletb.2020.135849. URL https://doi.org/10.1016%2Fj.physletb.2020.135849.

[216] D. L. Mihaylov et al. A femtoscopic correlation analysis tool using the schrödinger equation (CATS). *The European Physical Journal C*, 78(5), May 2018. doi: 10.1140/epjc/s10052-018-5859-0.

[217] Kfir Blum and Masahiro Takimoto. Nuclear coalescence from correlation functions. *Phys. Rev. C*, 99(4):044913, 2019. doi: 10.1103/PhysRevC.99.044913.

[218] Francesca Bellini, Kfir Blum, Alexander Phillip Kalweit, and Maximiliano Puccio. Examination of coalescence as the origin of nuclei in hadronic collisions. *Phys. Rev. C*, 103(1):014907, 2021. doi: 10.1103/PhysRevC.103.014907.

[219] L Fields and P Podlaski. Report from the NA61/SHINE experiment at the CERN SPS. *CERN-CDS*, 2020. URL http://cds.cern.ch/record/2739340.